Technical University of Denmark

DTU

Real-time detection of sub-monolayer desorption phenomena during electrochemical reactions: Instrument development and applications

Trimarco, Daniel Bøndergaard; Chorkendorff, Ib; Vesborg, Peter Christian Kjærgaard

Link back to DTU Orbit

DTU Library
Technical Information Center of Denmark

Real-time detection of sub-monolayer desorption phenomena during electrochemical reactions:
Instrument development and applications

Daniel Bøndergaard Trimarco

Department of Physics
Technical University of Denmark

August 2017

Real-time detection of sub-monolayer desorption phenomena during electrochemical reactions: Instrument development and applications

PhD dissertation by

Daniel Bøndergaard Trimarco

Supervisor: Professor Ib Chorkendorff

Co-supervisor: Associate Professor Peter C. K. Vesborg

August 2017

Surface Physics and Catalysis
Villum Center for the Science of Sustainable Fuels and Chemicals
Department of Physics
Technical University of Denmark

Front image:
Photograph of the latest iteration of the membrane chip developed as part of this PhD project. The photograph is taken by Jesper Scheel.

Preface

This thesis is written as the culmination of my PhD project, which has been funded by The Danish National Research Foundation and carried out in the Surface Physics and Catalysis (SurfCat) group at the Department of Physics under the supervision of Professor Ib Chorkendorff and Associate Professor Peter C. K. Vesborg. It is submitted as part of the requirements for obtaining a PhD degree from the Technical University of Denmark.

A patent filed on the membrane chip technology during the project is included in this thesis. This lead to a 12 month leave of absence in the period Apr 15th 2016 – Apr 14st 2017, during which I founded the company Spectro Inlets ApS in order to commercialize the technology. The work presented in this PhD thesis was conducted over three years in the periods Sep 1st 2013 – Apr 15th 2016 and Apr 14th 2017 – Aug 31st 2017.

Writing a PhD in the SurfCat group at DTU has truly been an enjoyable experience for me. It is a workplace full of technological creativity and academic drive, making highly interdisciplinary project like this one possible. I would like to thank all my good colleagues and friends at SurfCat, especially my co-supervisor Peter C. K. Vesborg for his innovative approach to science, which is truly admirable.

I am grateful to my main supervisor Ib Chorkendorff for giving me the opportunity to carry out this PhD project and for letting it unfold as organically as it did. In a sense, I think this project in particular represents Ib's way of facilitating interesting research and development in general. If there is the slightest change that a project can succeed, it is initiated, and often leads to a good outcome.

I have myself co-supervised five Master's projects and six smaller student projects over the course of my PhD. I would therefore like to thank all my students, with whom I have had many exciting and challenging discussions and conducted interesting research projects. I would especially like to thank Søren B. Scott, who did his Master's project, and later part of his own PhD work,

ii

on the experimental setup presented in this thesis. He has been involved in much of the development and has truly been the ideal sparring partner both for technical development and research ideas.

I would furthermore like to thank my company partner, Anil Haraksingh Thilsted, for helping me keep academic work and the company separate, especially towards the end of the PhD project, and I would like to thank Rasmus Ellebæk Christiansen, Asger Schou Jacobsen, Béla Sebök and Anders Holst Bodin for proof-reading and commenting on my thesis work.

It has truly been a pleasure to share both ups and downs of my PhD experience with my good friend Anders Holst Bodin, who I have known since my first day at DTU, now ten years ago. He has been a valuable support throughout the entire project, for which I am truly grateful.

Finally, I would like to thank my mom and dad, for their support throughout this endeavor, and for the deep curiosity and positive attitude that they have instilled in me. Most importantly, I would like to thank my girlfriend, Stine Nørgreen Madsen, for her unwavering support in helping me establish a solid base to explore from, and for her admirable patience with me throughout the past four years.

<div align="right">

Sincerely,

Daniel Bøndergaard Trimarco

(August 2017)

</div>

Abstract

This thesis presents the development of a novel analysis instrument for performing highly sensitive electrochemistry mass spectrometry (EC-MS) measurements in real-time. The instrument is based on a micofabricated membrane chip which is used to establish a direct loss–free coupling between wet electrochemistry and the vacuum of a mass spectrometer, thereby enabling a high detection probability of volatile analyte species by the mass spectrometer. The instrument exhibits a higher sensitivity than conventional differential electrochemical mass spectrometry (DEMS), while maintaining a fast response time, making it highly suitable for electrochemistry studies.

Incorporating the membrane chip into a stagnant thin–layer electrochemistry cell, 100 % collection efficiency is ensured, which makes it possible to utilize the full dynamic range of a standard MS, and thereby analyze desorption phenomena during electrochemical measurements with sub-monolayer sensitivity. The membrane chip furthermore makes it possible to directly control the dissolved gas atmosphere experienced by the working electrode by dosing gases through the membrane. Thereby reactant gases can be introduced, either for stead-state electrocatalytic measurements, or by transiently perturbing the system with single pulses of reactant gas injections.

The capabilities of the instrumentation are demonstrated by studying electrochemical hydrogen evolution (HER), oxygen evolution (OER), CO oxidation and CO stripping on polycrystalline platinum. The latter two are made possible by the transient and steady-state introduction CO reactant gas, respectively, through the membrane. A mass transport model is used to describe the analyte transport from the surface of an electrode, through the stagnant thin–layer cell, through the membrane chip and into the mass spectrometer. By applying this model to HER, OER, CO oxidation and CO stripping experiments, it is demonstrated possible to match anticipated mass spectrometer signals based on current measurements on the electrode, to the actual measured mass spectrometer signal. This mapping function thereby directly couples mass spectrometer

data with faradaic currents on the electrode surface.

The EC-MS instrumentation presented herein is utilized to discover a new electrocatalytic phenomenon during electrochemical CO reduction: By exposing a copper catalyst to dioxygen prior to constant–potential electrolysis, a new reaction pathway towards methane production is temporarily established. The phenomenon is shown only to affect the formation of methane, leaving ethylene and hydrogen formation unaffected. Using density functional theory (DFT) it is demonstrated that adsorbed oxygen on surface sites adjacent to under-coordinated kink sites destabilizes the binding energy of CO, while stabilizing the binding energy of CHO due to a geometric tilting effect. This causes the initial protonation towards methane, which is otherwise known to be rate–limiting on kink sites, to become energetically favorable. The phenomenon is short–lived, as the adsorbed oxygen reduces away within $\sim 1\,\mathrm{s}$ during which only a few turn–overs of methane occurs.

Furthermore, a preliminary EC-MS study is presented, which reveals a new desorption phenomenon on polycrystalline copper: By initially priming a copper electrode at cathodic potentials close to hydrogen evolution potentials, the desorption of $\sim 50\,\mathrm{pmol}$ of gaseous hydrogen, corresponding to $\sim 10\,\%$ of a monolayer, is measured when scanning to potential anodic of the reversible hydrogen potential (RHE). The phenomenon is proven to be electrochemically triggered, unrelated to copper oxidation and invariant to pH on the RHE scale. The amount of desorbed hydrogen is likewise proven to be unaffected by priming conditions and potential scan rates. By variation of the upper and lower potential limits the ad- and desorbtion potentials for hydrogen on copper are measured to be -0.125 and $+0.05\,\mathrm{V}$ vs RHE, respectively. The proposed mechanism is that hydrogen adsorbs to the surface at cathodic potentials prior to HER, and remain surface bound until it becomes energetically favorable to adsorb OH at more cathodic potentials, at which hydrogen is expelled through a surface replacement reaction. As only $\sim 10\,\%$ of a monolayer, is observed, the hydrogen is believed only to remain adsorbed on stronger binding step sites. The proposed mechanism is not yet verified with any theoretical predictions.

The presented electrochemical studies exemplifies some of the unique capabilities enabled by the presented EC-MS instrumentation. The potential for future application of the technique could be wide–spread and enable unique insight into electrochemical reaction mechanism through careful study of sub–monolayer desorbtion phenomena similar to the ones presented herein.

Resumé

Denne afhandling præsenterer udviklingen af et nyt analyseinstrument til at udføre yderst følsomme elektrokemi massespektrometri (EC-MS) målinger i realtid. Instrumentet er baseret på en mikrofabrikeret membranchip, som anvendes til at etablere en direkte, tabsfri kobling mellem væskebaseret elektrokemi og vakuummet i et massespektrometer (MS), for derved at muliggøre stor målingssandsynlighed overfor volatile analyt specier med MS'et. Instrumentet udviser en højere følsomhed en konventionel differentiel elektrokemisk massespektrometri (DEMS), samtidig med at det bevarer et hurtigt tidsrespons, hvilket gør det yderst anvendeligt til elektrokemi-studier.

Ved at inkorporere membranchippen i en elektrokemi-celle designet med et tyndt stillestående væskelag mellem membranen og elektroden, bliver 100 % opsamlingssandsynlig sikret, hvilket gør det muligt at udnytte den fylde dynamiske spændevidde for et standard MS og derved analysere desorberingsfænomener under elektrokemiske målinger, med en sub-monolagsfølsomhed. Membranchippen gør det ydermere muligt direkte at kontrollere den opløste gasatmosfære omkring arbejdselektroden, ved at dosere gasser gennem membranen. Derved kan der introduceres reaktantgasser enten til at udføre steady-state elektrokatalytiske målinger, eller til at perturbere systemet med enkelte pulser af reaktantgasinjektioner.

Instrumentets kunnen bliver demonstreret ved at studere elektrokemisk hydrogenudvikling (HER), oxygenudvikling (OER), CO oxidation og CO stripping på polykrystallinsk platin. De sidste to er muliggjort af den transiente og konstante introduktion af reaktantgas gennem membranen. En massetransportmodel bliver brugt til at beskrive analyt-transporten fra overfladen af elektroden, gennem den stillestående væske, gennem membranchippen og ind i MS'et. Ved at anvende denne model på HER, OER, CO oxidation og CO strippinger eksperimenterne, bliver det demonstreret hvordan det er muligt at matche det forventede MS signal baseret på en strømmåling på elektroden, til et faktisk MS signal. Denne koblingsfunktion kobler dermed MS data direkte til faradaiske

strømme på overfladen af elektroden.

EC-MS instrumentet præsenteret heri, bliver brugt til at opdage et nyt elektrokatalytisk fænomen under elektrokemisk reduktion af CO: Ved at eksponere en kobber-katalysator til diatomisk oxygen umiddelbart før et konstant-potential elektrolyse eksperiment, bliver en ny reaktionsvej til metanproduktion midlertidigt etableret. Fænomenet bliver vist kun at påvirke metanproduktionen, mens etylen- og hydrogenproduktion forbliver upåvirket. Ved at anvende density functional theory (DFT) bliver det vist at adsorberet oxygen på overflade-sites umiddelbart ved siden af under-koordineret kink-sites, destabiliserer bindingsenergien af CO, mens bindingsenergien for CHO bliver stabiliseret pga. en geometrisk tildningseffekt. Dette gør at det første protonerings-step til formning af metan, som ellers er kendt for at være rate-begrænsende på kink-sites, bliver energisk favorabelt. Fænomenet er kortlivet da det adsorberede oxygen reduceres væk indenfor $\sim 1\,\mathrm{s}$ alt imens nogle enkelte turn-overs af metan finder sted.

Ydermere bliver et præliminært EC-MS studie præsenteret, som afslører et nyt desorptionsfænomen på polykrystallinsk kopper: Ved først at prime en kopper elektrode ved katodiske potentialer tæt på hydrogen evolutionspotentialet, måles en desorption af $\sim 50\,\mathrm{pmol}$ gasfase-hydrogen, svarende til $\sim 10\,\%$ af et monolag, efter potentialet skannes anodisk ift. det reversible hydrogen potentiale (RHE). Fænomenet bliver vist at være elektrokemisk aktiveret, urelateret til kobber oxidation og uafhængig af pH på en RHE skala. Mængden af desorberet hydrogen er ligeledes vist upåvirket af hvordan elektroden primes og af skanneraten for potentialet. Ved at variere de øverste og nederest potentialbegrænsninger, bliver ad- og desorptionspotentialerne for hydrogen på kopper målt til at være henholdsvis -0.125 og $+0.05\,\mathrm{V}$ vs RHE. Den foreslåede mekanisme er, at hydrogen adsorberer til overfladen ved katodiske potentialer umiddelbart før HER og forbliver bundet til overfladen indtil det bliver energisk favorabelt at adsorbere OH ved mere katodiske potentialer, hvorved hydrogen bliver frastødt gennem en overflade-erstatningsreaktion. Da kun $\sim 10\,\%$ af et monolag bliver observeret, er det sandsynligt at hydrogen kun forbliver bundet til stærkere bindende step-sites. Denne foreslåede mekanisme er endnu ikke blevet verificeret med teoretiske forudsigelser.

De præsenterede elektrokemi-studier eksemplificerer nogle af de unikke anvendelsesmuligheder der bliver muliggjort med det præsenterede EC-MS instrument. Potentielle fremtidige anvendelser af denne teknik kan muligvis være omfattende og muliggøre unik indsigt i elektrokemiske reaktionsmekanismer gennem omhyggelige studier af sub-monolag desorptionsfænomener som dem der her bliver præsenteret.

List of publications

Appended publications

Paper I

Fast and sensitive method for detecting volatile species in liquids [P1]
<u>Daniel. B. Trimarco</u>, Thomas Pedersen, Ole Hansen, Ib Chorkendorff, and Peter
C. K. Vesborg
Rev. Sci. Instrum. **86**, 5006 (2015)

Paper II

**Real-time tracking of electrochemical desorption phenomena with
sub-monolayer sensitivity [P2]**
<u>Daniel. B. Trimarco</u>*, Soren B. Scott*, Anil H. Thilsted, Jesper Y. Pan, Thomas
Pedersen, Ole Hansen, Ib Chorkendorff, and Peter C. K. Vesborg
In preparation
∗These authors contributed equally to this work.

Paper III

Dynamic effects of surface oxygen in CO electroreduction [P3]
<u>Daniel. B. Trimarco</u>*, Soren B. Scott*, Anders Bodin*, Alexander Bagger, Nicola
Mazzanti, Jakob E. Sørensen, Thomas Pedersen, Ole Hansen, Ifan E. L. Stephens,
Peter C. K. Vesborg, Jan Rossmeisl, and Ib Chorkendorff
In preparation
∗These authors contributed equally to this work.

Paper IV

Anodic H$_2$ desorption from polycrystaline copper [P4]
Soren B. Scott, <u>Daniel. B. Trimarco</u>, Nikolaj R. Knøsgaard, Albert K. Engst-
feld, Jan Rossmeisl, Peter C. K. Vesborg and Ib Chorkendorff
In preparation

Publications not included in the thesis

Paper V

**Acetaldehyde as an intermediate in the electroreduction of carbon
monoxide to ethanol on oxide-derived copper**
Erlend Bertheussen, Arnau Verdaguer-Casadevall, Davide Ravasio, Joseph H.
Montoya, <u>Daniel B. Trimarco</u>, Claudie Roy, Sebastian Meier, Jürgen Wendland,
Jens K. Nørskov, Ifan E. L. Stephens, and Ib Chorkendorff
Angew. Chem. **128**, 1472 (2015)

Paper VI

**Fundamental understanding of NiFe catalyst for the electro-oxidation
of water under alkaline conditions using mass-selected nanoparticles**
Claudie Roy, Béla Sebök, Elisabetta M. Fiordaliso, Soren B. Scott, Jakob E.
Sørensen, <u>Daniel B. Trimarco</u>, Anders Bodin, Jakob Kibsgaard, Christian D.
Damsgaard, Ifan E. L. Stephens, Ib Chorkendorff
In preparation

Appended patents

Patent I

A device for extracting volatile species from a liquid
<u>Daniel. B. Trimarco</u>, Peter C. K. Vesborg, Thomas Pedersen, Ole Hansen, and
Ib Chorkendorff
Patent pending, publication no. WO 2016075208 A1
(priority date: Nov 14 2014, publication date: May 19 2016)

Contents

Chapter 1

Introduction

The transition to an electrified society is inevitable. With fossil fuel resources becoming more scarce and climate change increasingly apparent, the transition to sustainable energy sources like wind and solar is likely to happen. This will completely alter the energy landscape of the future global society, leading to electro- and biochemical technological solutions to energy storage and industrial chemical processes playing an increasingly important role [1].

This thesis presents the development and utilization of a novel analysis tool for investigating electrochemical reactions in real-time, which will hopefully help provide a greater understanding of fundamental electrochemical processes. Ultimately, tools like the one presented herein, and the research that such tools enable, can help establish a toolbox of electrochemistry based technological solutions to plug into, or establish, future electrified industries and thus help establish a sustainable global society. With this being the top motivation for the present PhD work, this chapter will begin with a sketch of today's energy and climate problem, discussing the importance of electrochemistry in relation to the changing global energy landscape and go through existing tools and methodologies for conducting real-time electrochemistry analysis.

1.1 Welcome to the Anthropocene

Since the industrial revolution the world has seen an exponential rise in human population and general human standard of living. At the beginning of the eighteenth century, there were just under one billion people on this planet and
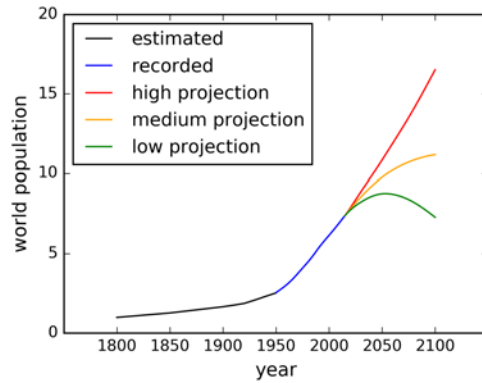
Figure 1.1: World population since the industrial revolution with data from the United Nations. Data for historical estimates from [2] and recorded data and projections from [3].

today there are 7.5 billion, a number which is still growing [3].

Most people now have access to electricity and clean water, and in the most developed countries it is even the norm to have free access to advanced health care and university level education. As living standards increase in developing countries, fertility rates tend to decrease to, or even below, the replacement level of 2.1 births per woman in a developed country [4]. Even the fertility rate in India has dropped to 2.3 as of 2017 [3]. Thus current predictions from the United Nations show that the human population will approach 11.2 billion people by the year 2100 (see Figure 1.1) [3].

A major part of this development is due to the discovery of fossil resources: non-renewable carbon compounds in the form of coal, oil and natural gas, which has accumulated in Earth's crust over millions of years. Today the global energy consumption sums to 526.4 quads (quadrillion British thermal units) or 154.4 PWh (petawatt hours) on a yearly basis (2016) equal to almost 18 TW of power every second of every day throughout the year [5]. 85 % of that power comes from burning fossil resources (33 % oil, 28 % coal, and 24 % gas) with the remaining 15 % coming from nuclear, biomass and renewable energy sources such as wind and solar [5]. Developed countries account for most of this consumption in order to maintain the high standard of living experienced in the modern western society today.
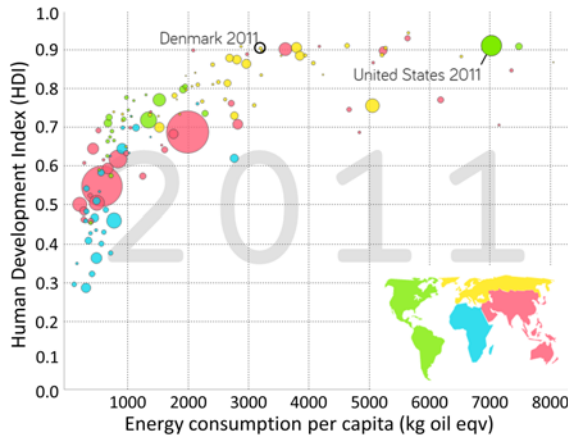
Figure 1.2: Human development index (HDI) as a function of energy consumption per capita for each of the worlds countries. Each circle represents a county with the size of the circle representing it's population. Data and figure from the online world data repository, Gapminder [6].

Approaching steady-state

As a measure of global standard of living the United Nations has introduced the *human development index* (HDI), which is a combined statistical measure of life expectancy, education, and per capita income [7]. Plotting the HDI as a function of energy consumption per capita for each of the worlds countries (see Figure 1.2) it becomes apparent that: 1) a high HDI costs a lot of resources and 2) HDI seems to stagnate in terms of energy consumption when approaching an HDI of 0.9. The Nordic countries; Denmark, Sweden and Norway, are among the top 10 most developed countries in the world, all with an HDI above 0.9, while having a maintained focus on energy efficiency. These countries are all located at the onset of the plateau in Figure 1.2. Using these countries as an averaged representation of a high, but obtainable, standard of living, it becomes apparent, that it "costs" about 5300 W per capita (4000 kg oil equivalent per capita per year) to reach and sustain an HDI of about 0.9.

As developing countries steadily seek, and ultimately reach, a similar standard of living as the more developed western countries, a further increase in global energy consumption will happen until steady-state is reached. As a rough upper estimate, "steady-state Earth" conditions thus seem to converge towards 60 TW power consumption in 2100 with 5300 kW per capita for each of the 11 billions people on the planet. Current projections estimate a global energy demand of 24 TW by 2040 [8].

Dependence on fossil resources

Taking the United States of America as an (over)estimation of a developed and industrialized country, a consideration can be made of how the consumption of fossil, and renewable, resources is distributed as of today (see Figure 1.3) in order to establish a proper basis for the above steady-state Earth projections. USA consumes 28.5 PWh of energy on a yearly basis (2016) corresponding to 18.5 % of the global consumption [5]. This energy is used to produce electricity, heating and cooling homes and work places, run large industries as well as transportation of goods and people both domestically and globally. 80 % is covered by fossil resources, which, for the most part are burned to acquire raw energy, with the remaining part used as feedstock of hydrocarbons and hydrogen to chemical industries where it is transformed into higher value products like fertilizers and plastics. From this depiction it becomes apparent how heavily modern society relies on fossil fuels.

Business-as-usual is unsustainable

With a human population in the billions and standards of living raised to modern levels, we have entered a new epoch where human activity has become significant enough to perturb the geological system of the entire planet. As proposed by Nobel laureate Paul Crutzen in 2002, we have now entered the Anthropocene [10].

Already today, clear signs of global warming due to green house gas emissions (CO_2, CH_4 and N_2O) are showing, as well as mass extinction of animal species due to pollution and deforestation. Oceans are rising and acidifying, and the climate system is pumped with 330 TW of additional power every single day due to global warming [11], corresponding to 18 times as much energy as today's global energy consumption by humans. This in turn causes more extreme hurricanes, droughts and rainfalls, all with significant impact on both human and animal living conditions. These signs of climate change have all been thoroughly documented in a synthesis report by the United Nations's Intergovernmental Panel on Climate Change (IPCC) in 2014 [12].

Policy makers are therefore working towards making society independent of fossil resources, with the Paris Agreement of 2015 marking a true turning point. Every country in the world, excluding Nicaragua and Syria, agreed to significantly reduce anthropogenic greenhouse gas emissions in order to keep the global average temperature increase well below 2°C, relative to preindustrial levels [13]. For temperature changes above a 2°C increase the IPCC report projects significant changes to the global ecosystem, which will have severe consequences for human and animal living conditions. The worst case scenario presented by the IPCC synthesis report, with a business-as-usual approach to fossil resource consumption and green house gas emissions, projects a global temperature increase of 4.5°C. A few degrees of temperature change does not sound like much,
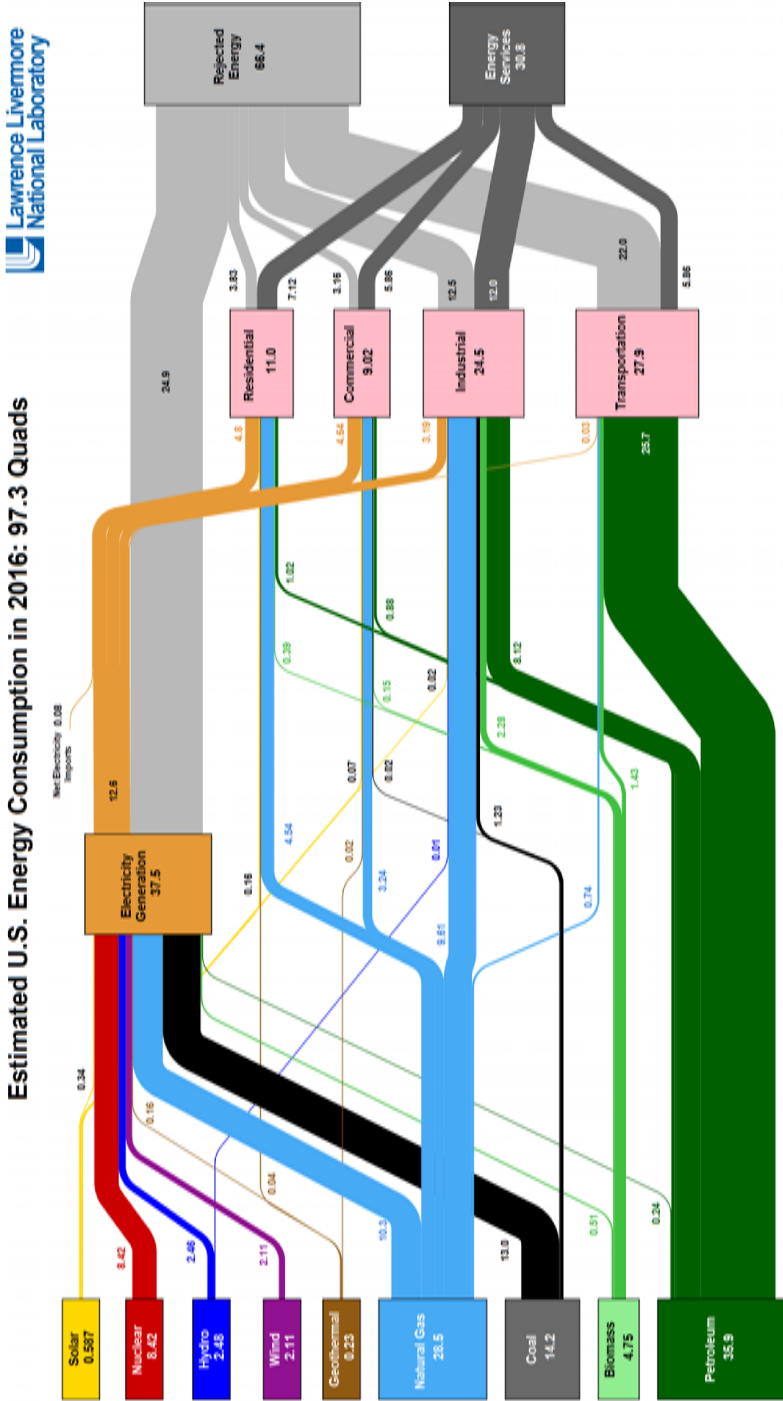
Figure 1.3: Flow chart, or "Sankey diagram", illustrating the conversion of fossil and renewable resources into value for the residential, commercial, industrial and transportation sectors, respectively, for the United States in 2016. Rejected energy represents heat loss from each conversion process. Figure from Lawrence Livermore National Laboratory [9].

but to put it in perspective, the average global temperature during the last ice age was only 4.5°C below the 20th century norm, as illustrated quite explicitly by the online comic strip, xkcd, in 2014 (see Figure 1.4). In other words, a business-as-usual approach to fossil resource consumption would be highly irresponsible.

In addition, at the current rate of consumption non-renewable resources will eventually run out, or at least reach a situation where extraction is no longer feasible. This becomes apparent when considering the *energy return on energy invested* (EROI), an estimated ratio of what fraction of input energy will return as an output, for the oil and gas industry from 1930 to present day (see Figure 1.5) [15]. In short, the planetary boundary has been reached [16].

Transition to an electrified society

Since the Paris Agreement was signed individual countries have made increasingly optimistic goals for decommissioning coal power plants, electrifying personal transport, and ramping up installation of sustainable energy sources like wind and solar. There is no shortage of technologically viable solution for transitioning completely to sustainable energy solutions [17], and as of 2017 non-subsidized solar power has become cheaper than coal-based thermal power plants, making sustainable green energy the go-to choice for a range of energy solutions [18].

Returning to the energy landscape presented in Figure 1.3 the world is thus transitioning away from a society relying on fossil resources, and towards a society where the main input parameter to society and its industries is intermittent electricity or direct solar energy, as well as renewable abundant chemical building blocks like N_2, O_2, H_2O and biomass. As a thought experiment, imagine therefore Figure 1.3 with only an orange (electricity) and a light green (biomass)
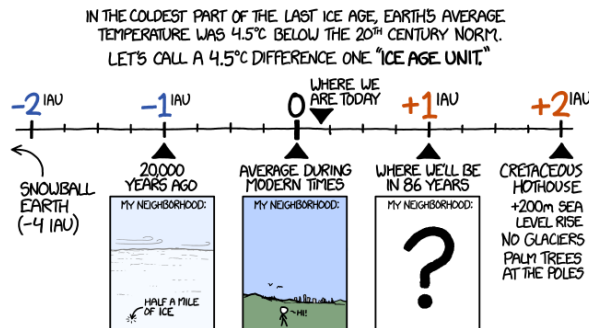
Figure 1.4: Comic strip illustrating the magnitude of "a few degrees" change in global temperature by comparing to the global temperature during the last ice age. From the online comic strip, xkcd [14].
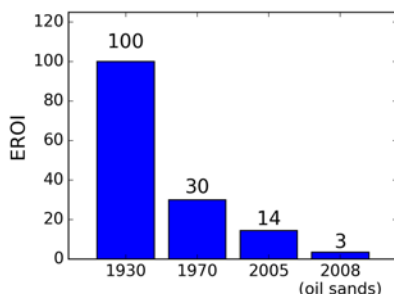
Figure 1.5: Energy return on energy invested (EROI) for oil and gas from 1930 to present day. Data from [15].

box on the left hand side. With such energy infrastructure, how will ammonia be generated to produce enough fertilizer to feed 11 billion people? How will plastics and base chemicals be made, to support future chemical industries? How will energy carriers be formed, which are dense enough to ensure global shipping of goods and people? In other words: one of the ultimate long term technological challenges that society is facing, is to establish a steady-state 60 TW global society based on electricity and renewable resources as input parameters.

Electro- and biochemical technology solutions could play a large role in solving these problems, the former in particular, with electricity becoming an abundant and practically free resource, especially during peak production. Electrochemical technology solutions could furthermore be used in cheap decentralized units, often operating at room temperature, which are able to turn on and off quickly and thus adapt to a fluctuating energy input and with redundant systems capable of handling peak energy production. Already today, a large focus is thus put on technological development supporting this transition, with e.g. the German technology company, Siemens, investing \$1.1B over a five year period in technologies related to decentralized electrification as of 2016 [19].

As stated in the beginning of this chapter, electrification of society represents a top motivation for studying electrochemistry and in particular for developing instrumentation which enables further research in the field. In chapter 5 of this thesis research results will be presented on the electrochemical production of hydrocarbons from carbonated water and electricity (electrochemical CO hydrogenation). For now this field is fundamental research and does not yet show industrial applicability, but having a toolbox of such electrochemical technology solution to be used in the future fossil free society will definitely make it easier to restructure the energy landscape in Figure 1.3 and thereby ensure a sustainable future society.

1.2 Introduction to electrochemistry

Before progressing any further, a brief introduction to the field of electrochemistry is in order.

Electrochemisty is the field of science describing chemical change to a substance caused by an electrical input, or vice versa. The energy input in an electrochemical system is given as a potential difference, ΔU, between two electrodes, which establishes a strong electric field at the electrode-electrolyte interface referred to as the Helmholz layer, which drives an electrochemical reaction on either electrode.

The chemistry occurring on the surface of the electrode is strongly dependent on the choice and morphology of the electrode material and the potential difference, ΔU, applied, as any of these parameters change the catalytic behavior of the electrode. A large part of understanding the fundamental science of electrochemistry thus lies in the interdisciplinary field of electrocatalysis, which involves a deep understanding of both surface science and physical chemistry.

Introduction to electrocatalysis

The overarching goal of electrocatalysis is to optimize the rate of a given electrochemical reaction on the surface of an electrode through the choice of electrode material and ΔU. A suitable catalyst increases the rate of a chemical reaction by lowering the energy barrier or activation energy, by providing a surface where reactants can bind to and then react with each in order to form products [20], as exemplified in Figure 1.6a for the oxidation of CO to CO_2 on a Pt surface. Without the presence of a catalyst the reaction proceeds slowly despite the final product having a lower free energy. This is due to a short lived transition state, with a high potential energy. On a suitable catalyst reactants can bind and/or
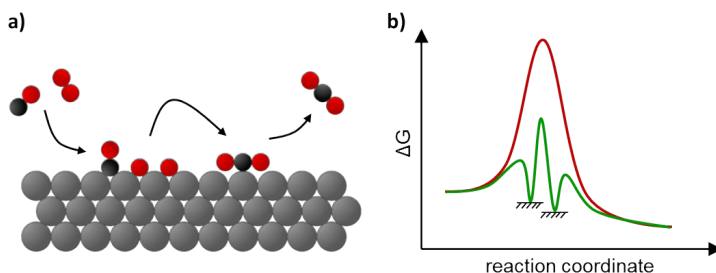
Figure 1.6: a) Schematic illustrating the catalytic oxidation of CO to CO_2 on a Pt surface with carbon depicted in black and oxygen in red. **b)** Schematic illustration of a free energy diagram showing the energy barrier with (green) and without (red) the presence of a catalyst.

dissociate on the surface and form intermediates, which can then react with much lower energy barriers as illustrated in Figure 1.6b.

Catalytic activity is thus associated with the binding energy of reactants, intermediates and products on the surface. If reactants and dissociated reaction intermediates bind too weakly, adsorption and/or dissociation will never take place. If any adsorbate, however, binds too strongly, it will stay on the surface, "poisoning" any catalytically active sites, and preventing the capture of new reactants. This principle of the existence of an optimal binding energy is called the Sabatier principle, as introduced by Nobel laureate Paul Sabatier in 1912 [21].

Electrochemical reactions involving the transfer of electrons between the electrode and the reactants, i.e. faradaic processes, are called a *reduction-oxidation* (redox) reactions. The rate of redox reactions can be measured as the flow of electrons through the electrode-electrolyte interface, measured as a faradaic current, which scales with ΔU. The redox reactions occurring on either electrode in an electrochemical system can be considered as two half reactions where the electrode at which the oxidation reaction occurs is conventionally called the *anode*, while the reduction reaction takes place on the *cathode*.

Electrocatalysis in the laboratory

In order to study the catalysis of a single half reaction in the laboratory, one electrode, referred to as the *working electrode* (WE), is isolated by setting an arbitrary potential against a dummy *counter electrode* (CE) while measuring the potential difference against a *reference electrode* (RE), an electrode with a known absolute potential. That way, the faradaic current, measured between the WE and CE, can be directly related to the absolute potential of the WE (see Figure 1.7).

The conventional zero-point used in electrochemistry for the RE is the equilibrium potential of the H_2/H^+ redox couple, referred to as the *standard hydrogen electrode* (SHE) potential. This potential is pH dependent, so a more common standard is the *reversible hydrogen electrode* (RHE), which is adjusted for pH using the Nernst equation [22]. A suitable SHE reference electrode can be established by submerging a Pt electrode into a pH 0 acid saturated with

Figure 1.7: Schematic depiction of a three electrode setup.

1 bar of $H_2(g)$. Pt is practically a reversible catalyst for the *hydrogen evolution reaction* (HER), meaning that almost no overpotential is needed to drive either the reduction of H^+ or the oxidation of H_2.
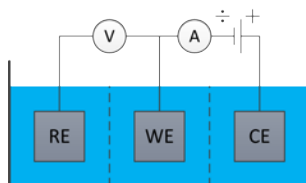
Standard laboratory electrochemistry conditions

In order to gain fundamental understanding of electocatalytic reactions, a deep understanding of the interface between the electrode and electrolyte is necessary to get insight into reaction mechanisms. Ultimately it all comes back to the fundamental definition of electrochemistry: what chemical change is induced by the application of an electrical energy input. Often chemical change involves gaseous reactants and/or products, or strongly adsorbed intermediates.

In order to establish an understanding of the experimental conditions during laboratory scale electrochemistry, consider, as an example, electrochemical hydrogen evolution, i.e. one of the half reactions of water splitting, on a perfectly flat Pt electrode. Polycrystalline Pt contains $\sim 1.7 \times 10^{15}$ surface atoms per cm^2 [23]. At 1 mA of faradaic current $\sim 3.1 \times 10^{15}$ H_2 molecules are generated per cm^2 per second ($\frac{1}{2q_e} \cdot 1$ mA where q_e is the electron charge), corresponding to a *turn-over-frequency* (ToF) of ~ 1. 1 mA is considered a standard current density during laboratory scale electrocatalytic experiments. Let us call this this the anticipated analyte product rate, $\dot{N}_0^{el}$, at the surface of a working electrode, where

$$\dot{N}_0^{el} \approx 10^{15} \, \text{molecules s}^{-1} \, . \tag{1.1}$$

Thus, under typical laboratory conditions for electrocatalysis studies, the desorption of a single monolayer (or below) of reaction products per cm^2 per second, can be expected. Above $1\,mA/cm^2$ bubbles start forming on the electrode, due to diffusion limitation and saturation of the electrolyte, if convective transport is not applied, which makes well-defined studies difficult to conduct.

In order to correlate desorbtion of reaction products, or strongly bound reaction intermediates, with the applied electrical potential and faradaic current measured during electrocatalytic experiments, and thus get insight into reaction mechanisms of a given electrocatalytic process, it is therefore necessary to have an analysis tool capable of capturing and analyzing less than a monolayer of electrochemical reaction products in real-time. In other words, being able to measure $< 10^{15}$ analyte molecules per second.

1.3 Electrochemistry mass spectrometry

A *mass spectrometer* (MS) is a viable candidate for such a tool, with inherent sampling speed in the sub-second range and sensitivities down to *parts-per-trillion* (ppt). A mass spectrometer can be thought of as a "molecular scale", which is capable of counting individual molecules, sorted according to their
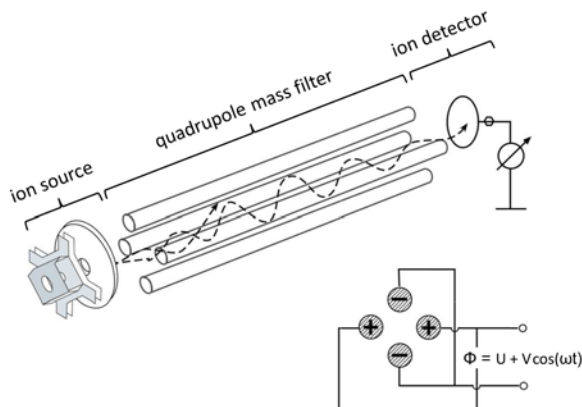
Figure 1.8: Schematic depiction of a quadrupole mass spectrometer (QMS). Figure from [24].

molecular mass, m. A mass spectrometer consists of three main components: an ion source, a mass filter and a detector, as sketched in Figure 1.8. The most commonly used mass spectrometer is a *quadrupole mass spectrometer* (QMS), using "hard" *electron impact ionization* (EI) and a quadrupole mass filter.

Such a mass spectrometer operates by ionizing an incoming stream of gas by electron bombardment, after which positively ionized molecules gets accelerated into the quadropole filter, where an oscillating electro-magnetic field ensures only a single stable spiral trajectory for a given m/z ratio, where m is the molecular mass measured in *atomic mass units* (amu) and z is the charge.

After filtering, molecules with a specific m/z ratio proceed to the detector, which is usually either a Faraday cup (a simple wire or plate grounded through a sensitive electrometer), where the count of individual molecules is directly measured as a current in amperes, or a *secondary electron multiplier* (SEM), where the impact of the incoming ion produces a cascade of electrons, which helps boosting the signal to noise ratio.

However, a mass spectrometer has a maximum operating pressure of 10^{-6} mbar, also referred to as *ultra-high vacuum* (UHV), bordering to *high vacuum* (HV), which makes it difficult to couple a MS directly to an electrochemistry test environment at 1 bar, given a 12 orders of magnitude difference in molecular density between the two. Above 10^{-6} mbar non-linearity can occur do to space charge formation in the ionization zone or non-ballistic motion in the filtering zone, as well as gradual degradation of ionization filaments and detectors [25].

UHV is usually obtained with a *turbo molecular pump* (TMP). Assuming a standard off-the-shelf TMP (e.g. Pfeiffer HiPace 80) delivering a pumping speed of at least 50 l/s on all gaseous species, the total in-flux to a MS cannot be more

than

$$\dot{N}_0^{\mathrm{v}} = \frac{1}{k_{\mathrm{B}}T} \, 50 \times 10^{-6} \, \mathrm{mbar\,l\,s^{-1}} \approx 10^{15} \, \mathrm{molecules\,s^{-1}} \ , \qquad (1.2)$$

assuming *room temperature and pressure* (RTP). This molecular flux thus sets the ultimate boundary condition for how much analyte can be passed into a mass spectrometer during measurements.

Luckily, however, this molecular flux tolerance coincidentally matches the anticipated analyte production rate during laboratory condition electrochemistry measurements, as described previously (Equation 1.1). So given a finely tuned permeable interface, which carefully delivers reaction products from the surface of an electrode to a mass spectrometer for detection, the full utilization of mass spectrometry for electrochemistry measurements should be possible.

It should of course be noted, that this particular $\dot{N}_0^{\mathrm{v}}$ can be circumvented by either using a bigger pumping system, or simply by accepting non-liniarities and faster system degradation in the MS. These trade-offs will not be the subject of this PhD work. $\dot{N}_0^{\mathrm{v}}$ will be used as a reference point, representing ideal mass spectrometry conditions using standard MS and vacuum components, providing a basis for comparison between different system configurations.

Membrane inlet systems

In order to analyze dissolved analyte species in real-time in a liquid using a mass spectrometer a proper membrane inlet system is needed. The membrane serves the purpose of extracting dissolved analyte to the gaseous phase, given that the analyte is volatile, i.e. has a measurable vapor pressure, and delivering the gaseous analyte to the MS, without violating $\dot{N}_0^{\mathrm{v}}$.

The idea of applying mass spectrometry to analyzing dissolved analyte species in liquids originates from 1963 where Hoch and Kok introduced a technique called *membrane inlet mass spectrometry* (MIMS) [26]. In MIMS volatile species permeate through semi-permeable polymer membranes, typically *polydimethylsiloxane* (PDMS), directly into a mass spectrometer. This technique was developed to study biological systems and has been widely used for that purpose ever since.

The total flux of a given analyte species, n, across a polymer membrane scales with the diffusivity, D and solubility, S, of solvent and analytes inside the membrane material, and the thickness, l, and cross sectional area, A, of the membrane as:

$$\dot{N}_n^{\mathrm{MIMS}} = \frac{A}{l} D_n S_n p_n \ . \qquad (1.3)$$

The membrane material and size (A/l) is chosen in order for $\sum_n \dot{N}_n^{\mathrm{MIMS}}$ to satisfy $\dot{N}_0^{\mathrm{v}}$ (Equation 1.2) and thus allow a direct coupling to MS. Most polymers

have a relatively high permeability for water vapor, which makes up most of the molecular flux and which sets the upper boundary for (A/l).

MIMS systems are capable of highly sensitive measurements, especially if the membrane material is chosen for preferential permeation of the analyte species of interest, which causes an up-concentration of analyte inside the membrane. MIMS systems, however, suffer from a slow time-response due to the diffusive transport mechanism through the membrane material, which makes them unsuitable for time–resolved electrochemistry measurements.

In 1971 Bruckenstein and Gadde improved membrane transport drastically by changing to a perforated and hydrophobic membrane made of porous polytetrafluoroethylene (PTFE), through which both water and analyte could evaporate much quicker [27]. The molecular flux across such a porous PTFE membrane is dominated by the mean free path of molecules in the pores of the membrane and can thus be described by Knudsen diffusion [28], as:

$$\dot{N}_n^{\mathrm{DEMS}} = \frac{1}{k_\mathrm{B}T} p_n \frac{\phi_p A}{l_p} \frac{d_p}{3} \sqrt{\frac{8}{\pi} \frac{k_\mathrm{B}T}{m_n}} \; , \tag{1.4}$$

where l_p is the length of the pores ($\sim$ membrane thickness), d_p is the diameter, ϕ_p is the pore density (as a fraction between 0 and 1) and m_n is the molecular mass of the species. This flux is strictly dominated by water evaporation. For a $0.5\,\mathrm{cm}^2$ large membrane with a pore size of $l_p = 100\,\mu\mathrm{m}$ and $d_p = 20\,\mathrm{nm}$, and a pore density of 0.5 (typical for e.g. Gore-Tex), Equation 1.4 yields $\sim 10^{18}$ molecules/s for water alone [29]. This makes it difficult to sustain the 10^{-6} mbar operation pressure needed for a mass spectrometer. In the first electrochemistry studies, an integrative approach was therefore applied, where the linear response of the MS was simply measured as a function of the steadily increasing pressure in the mass spectrometer. In 1984 Wolter and Heitbaum improved the vacuum system drastically by introducing differential pumping [30], which made it possible to continuously maintain a suitable pressure in the MS and thus allowed for *differential*, i.e. time-resolved, *electrochemical mass spectrometry* (DEMS) measurements.

The porous membrane inlet combined with differential pumping has the obvious advantage of a fast time-response, but suffer from a high background signal from water in the mass spectrometer, macroscopic local loss of electrolyte through evaporation, and loss of analyte to differential pumping. In other words: in conventional DEMS the total molecular flux to the MS is mismatched compared to the anticipated analyte production rate during laboratory electrocatalysis by almost three orders of magnitude. This makes it difficult to optimize the mass spectrometer for the sensitive sub-monolayer measurements in electrocatalysis. This mismatch is corrected for by differential pumping, which causes only a fraction of the total amount of analyte to reach the actual mass spectrometer. This can be described as a vacuum collection efficiency, η_v, representing the fraction of analyte reaching the mass spectrometer, $\dot{N}_\mathrm{v}$, after crossing the

membrane, $\dot{N}_{\mathrm{m}}$, as:

$$\eta_{\mathrm{v}} = \frac{\dot{N}_{\mathrm{v}}}{\dot{N}_{\mathrm{m}}} \ . \tag{1.5}$$

It should be noted that η_{v} should be thought of as an abstract descriptor for the relative sensitivity. In most conventional DEMS setups η_{v} represents an actual loss of analyte to the differential pumping, with $\eta_{\mathrm{v}} \approx 0.001$ given a water evaporation rate of $\sim 10^{18}$ molecules/s. As an alternative configuration the ionization zone can however be placed in the high pressure part of the vacuum system, with correspondingly lower ionization rate applied in order to prevent non-linearity from space charging. This in turn results in a lower MS sensitivity towards the incoming analyte species, which here is assumed to be comparable to the effect of differential pumping.

Electrochemistry cells

Since 1984, DEMS has undergone a huge development with the main focus being on electrochemistry cell design. The first "classical" DEMS cell designs from 1971 and 1984 utilized deposition of electrode material directly onto the membrane inlet, allowing for a fast transport of analyte within the electrolyte. In 1993 Baltruschat introduced a stagnant thin–layer cell [31], allowing for the use of massive working electrodes placed directly opposite of the membrane inlet with a $100\,\mu\mathrm{m}$ thick Teflon (PTFE) spacer used to define the working distance between the electrode and the membrane, forming a thin–layer electrochemistry working volume between the two.

These first cell configurations were all able to capture $100\,\%$ of the analyte produced at the working electrode given that the electrode was smaller than the membrane area and placed in close proximity to the membrane, as long as the faradaic current was kept small ($\sim 1\,\mathrm{mA/cm^2}$). This introduces the concept of a membrane collection efficiency, η_{m}, relating the amount of analyte reaching the vacuum system, $\dot{N}_{\mathrm{m}}$, to the amount of analyte produced at the working electrode, $\dot{N}_{\mathrm{el}}$, as:

$$\eta_{\mathrm{m}} = \frac{\dot{N}_{\mathrm{m}}}{\dot{N}_{\mathrm{el}}} \ . \tag{1.6}$$

With this notion of a membrane collection efficiency, an overall collection efficiency can now be introduced by combing the membrane and vacuum collection efficiency for a given electrochemisty mass spectrometry system as:

$$\eta = \eta_{\mathrm{m}}\eta_{\mathrm{v}} = \frac{\dot{N}_{\mathrm{m}}}{\dot{N}_{\mathrm{el}}} \frac{\dot{N}_{\mathrm{v}}}{\dot{N}_{\mathrm{m}}} = \frac{\dot{N}_{\mathrm{v}}}{\dot{N}_{\mathrm{el}}} \ . \tag{1.7}$$

This metric will be used again in later chapters in order to benchmark the device developed in this PhD work against conventional DEMS systems.

The response time in the stagnant thin-layer cell is fast, but limited by the diffusion across the electrolyte layer. For less volatile species, it can furthermore be limited by evaporation across the membrane interface, causing both time-delay and up-concentration of analyte species in the thin layer working volume. Both diffusion and evaporation varies between different analyte species. Furthermore the stagnant thin-layer cell does not allow for the use of pre-purged electrolytes as the working volume gets, per design, immediately depleted from purging gas.

In order to lock down the time-response and allow the use of pre-purged electrolytes, a dual thin–layer flow cell was introduced by Jusys, et al. in 1999 [32], which utilized a thin–layer working volume and a corresponding thin–layer collection volume placed above a porous PTFE membrane down stream from a working electrode. These cells typically have an internal volume of $\sim 5\,\mu$l and a continuous electrolyte flow of $\sim 5\,\mu$l/s, giving a time response of $\sim 1\,$s [29]. At these flow-rates $100\,\%$ membrane collection efficiency is however no longer possible, especially for less volatile species, which affects the overall sensitivity.

Throughout the years many other cell designs have been introduced, including hanging meniscus configurations, which are particularly useful for single crystal studies [33–35], and other more exotic cell designs like rotating disk electrode [36] and scanning flow cell configurations [37, 38]. DEMS has also been coupled to complementary detection techniques like e.g. infrared spectroscopy (IR) [39] and electrochemical detection methods [40, 41].

Most of the above-mentioned DEMS configurations utilize similar membrane inlet systems constituting of nanoporous PTFE membranes and differential pumping. Other inlet systems have been introduced, which circumvent the need for differential pumping by decreasing the inlet area (see Equation 1.4) and thus probing a single location on an electrode, typically in a hanging meniscus configuration [34]. These systems are often referred to as *on-line electrochemistry mass spectrometry* (OLEMS) systems. OLEMS cell configurations tend to be more versatile to use, but are incapable of quantitative analysis. OLEMS should not be confused with system configurations sampling the head space (gas volume) above the electrolyte surface in a larger electrochemistry cell [42], often referred to as OEMS. These systems do also perform "on-line" analysis, but calling it real-time would be a misinterpretation.

Since the introduction of DEMS, this method has been widely used to gain insight into electrochemical reaction mechanics, with ethanol [43] and methanol [44] oxidation, complex electrocatalytic systems like electrochemical CO_2 hydrogenation [45] (see also chapter 5) and fundamental battery research [42, 46] representing a few examples.

The above is only a selection of key developments in the history of membrane inlet mass spectrometry. A detailed review of the historical development of MIMS can be found in [47], reviews on specific polymer membrane MIMS systems (oriented towards biochemistry) can be found in [48–57], and reviews on conventional DEMS systems (for electrochemistry) can be found in [29, 58, 59].

1.4 Thesis outline

The present PhD work has focused on the development of a novel membrane inlet system, based on microfabrication technology, for performing electrochemistry mass spectrometry measurements. The anticipated analyte production rate, $\dot{N}_0^{rel}$ (Equation 1.1), and the maximum tolerated molecular flux to a mass spectrometer, $\dot{N}_0^{v}$ (Equation 1.2), have been used as design parameters to construct a micro-fabricated *membrane chip* used to establish a permeable interface between electrochemistry and mass spectrometry. This membrane chip enables highly sensitive *electrochemistry mass spectrometry* (EC-MS) measurements with added functionalities like dosing of reactant gases and ease of quantification. Besides the fundamental development of the membrane chip analysis tool, several electrocatalysis studies have been conducted as part of this PhD work, of which two will be highlighted in this thesis.

In order to best present the development and use of the membrane chip EC-MS instrumentation, this thesis is structured with a total of seven chapters, including this introduction, which constitutes the following:

Chapter 1 (this chapter): A motivation for this PhD work, an introduction to electrochemistry and an overview of the historical development of electrochemistry mass spectrometry.

Chapter 2: A presentation of EC-MS using a microfabricated membrane inlet system with main focus on fundamental concepts, functionality of the instrumentation and description of analysis methodology.

Chapter 3: Modeling of analyte transport in the membrane chip EC-MS setup with comparison to conventional DEMS.

Chapter 4: A description of design considerations leading to the development of the membrane chip, vacuum system and electrochemstry cell presented in Chapter 2, including highlights of the historical development.

Chapter 5: An EC-MS study of a novel phenomenon demonstrating a transient increase in CH_4 production on mass-selected Cu nanoparticles caused by a CO electroreduction pathway being temporarily activated by surface adsorbed oxygen.

Chapter 6: An EC-MS study of a novel phenomenon demonstrating electrochemical desorption of H_2 on a Cu electrode, at potentials anodic of the reversible hydrogen potential.

Chapter 7: Concluding remarks including a perspective on future development possibilities of the presented EC-MS instrumentation.

Chapters 2 and 3 will cover the basics about the membrane chip EC-MS tool developed throughout this PhD and will thus provide the sufficient background knowledge for understanding the research presented in chapters 5 and 6. Chapter 4 is meant for the curious reader, interested in the details on the design considerations in the building of the membrane chip EC-MS setup. This chapter is furthermore meant to establish a toolbox of sufficient know-how, for expanding on the present PhD work during future development of the instrumentation.

A readers guide

Throughout the thesis abbreviations for commonly used concepts, instruments and methods, will be introduced at first use, by highlighting the abbreviated words in *italic*, followed by the abbreviation in a parenthesis, as done earlier in this chapter for e.g. *quadrupole mass spectrometry* (QMS). Citations are made using consecutive numbering in square brackets and the papers included in in this thesis are specifically referred to as [PX], with X being a number from 1 to 4. This notation will also be used in the header of each chapter containing material from the included papers.

Membrane chip EC-MS

This chapter presents the final version of the *electrochemistry mass spectrometry* (EC-MS) tool developed as part of this PhD work. The main focus will be on the general concept and functionality of the system, which will help define the basic terms describing the technology. Bear in mind, that the analysis tool presented in the following is the culmination of three years of work, and thus many details and design considerations will for now be left out. In chapter 4, however, a more detailed description of the development process will be presented, which will both elaborate on detailed working principles of the equipment and help establish a design toolbox for further development.

In the present PhD work a direct coupling between electrochemistry and mass spectrometry is established using a micro-fabricated *membrane chip*, which allows for a compact vacuum system and enables $100\,\%$ vacuum collection efficiency, while maintaining a fast membrane transport. The membrane chip thus combines the best from both semi-permeable polymer membrane, and nanoporous and differential pumped membrane inlet systems, as discussed in chapter 1.

2.1 Membrane chip

The membrane chip, as seen in the photograph in Figure 2.1a, is a 15 x 15 x 0.9 mm microchip with a $7\,mm$ diameter micro porous and hydrophobic *membrane* on the top side, placed above a small *sampling volume* (inside the chip), which in turn couples directly to a mass spectrometer through a finely tuned micro
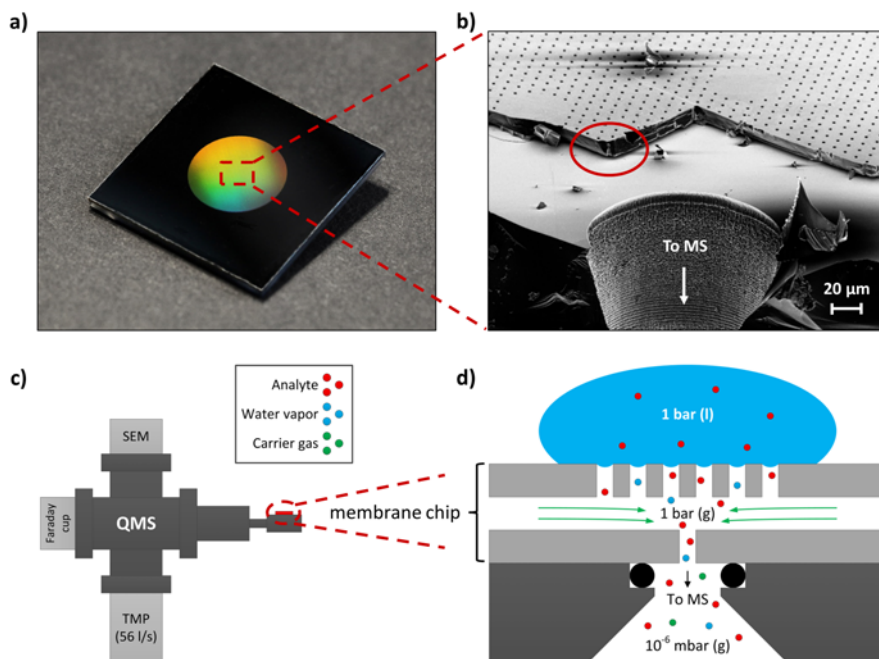
Figure 2.1: a) Photograph of the membrane chip consisting of a micro porous and hydrophobic membrane suspended across a small internal sampling volume inside the chip. **b)** Scanning electron microscopy (SEM) image revealing the internal structure of a membrane chip, which has been cut open across the middle of the chip. **c)** Schematic of the compact mass spectrometer vacuum chamber, to which the membrane chip, here depicted in red, is coupled. A photograph of the vacuum chamber can be found in Figure A.1. **d)** Schematic illustrating the working principle of the membrane chip, drawn as a schematic side view depiction of the internal structure shown in the SEM image in **c**. In reality the capillary coupling to UHV is made through a series of capillary channels placed downstream (on the backside of the chip) of the large hole shown in **c**). A detailed description of the membrane chip gas handling can be found in chapter 4.

capillary located on the backside (not visible). The micro porous membrane results in colorful diffraction patterns making the membrane stand out during photography.

The *scanning electron microscopy* (SEM) image in Figure 2.1b shows a membrane chip, which is cut across the middle to illustrate the internal structure. The porous membrane is $10\,\mu$m thick consist of $2.5\,\mu$m large pores distributed in a honeycomb pattern. Underneath the entire membrane is a $3\,\mu$m tall and

$7000\,\mu$m wide sampling volume, which is apparent by the shadow underneath the membrane, highlighted by the red circle in Figure 2.1b. The membrane connects to the mass spectrometer through an outlet in the center, which leads to a micro capillary placed on the backside of the chip (not visible). The membrane chip is fabricated in a clean-room using standard micro fabrication techniques, such as UV lithography, deep reactive ion etching (DRIE), hydrophloric etching (HF), anodic bonding and molecular vapor deposition (MVD), which will be described in more detail in chapter 4.

Working principle

During operation, the membrane chip acts as an "equilibration buffer" between an aqueous electrolyte and the vacuum of a mass spectrometer, as illustrated in Figure 2.1d. When exposed to water, a large liquid–gas interface is formed across the hydrophobic pore structure of the membrane. The sampling volume underneath, with a total volume of $\sim 100\,$nl, then equilibrates within a few milliseconds to $\sim 30\,$mbar of water vapor (at room temperature) as well as the vapor pressure, p_n, of any volatile compounds dissolved in the water through Henry's law of volatility [60]:

$$K_n^{pc} = \frac{p_n}{c_n} \; , \qquad\qquad (2.1)$$

where c_n is the concentration of a given analyte compound, n, in the water immediately above the membrane.

During water exposure inert gas (He) is continuously introduced at the rim of the sampling volume to make up for the pressure difference to ambient ($\sim 1\,$bar). This gas is referred to as a carrier gas, even though diffusion is the dominant transport mechanism in the sampling volume, and the inert gas serves primarily to hold a constant pressure in the sampling volume. The sampling volume is coupled directly to a mass spectrometer through a finely tuned micro capillary on the backside of the membrane chip, designed to let $(1.6 \pm 0.3) \times 10^{15}$ molecules/s into the MS and thus satisfying $\dot{N}_0^Y$, as described in chapter 1. With a sampling volume of only 100 nl this means that the entire volume, at 1 bar, is delivered to the MS within $\sim 1\,$s, ensuring a fast analyte transport across the entire liquid–vacuum interface.

The working principle of the membrane chip is demonstrated in Figure 2.2 where a membrane chip is first exposed to ambient air before being covered by a droplet of water. During air exposure a full MS spectrum is generated (see Figure 2.2a), with the components of air showing up as expected in the MS signal for $^m/_z = 18$, 28, 32, 40 and 44 corresponding to H_2O, N_2, O_2, Ar and CO_2, respectively. The peak intensity for each compound is then recorded as a function of time, as shown in Figure 2.2b, while a droplet of water is placed onto the membrane.
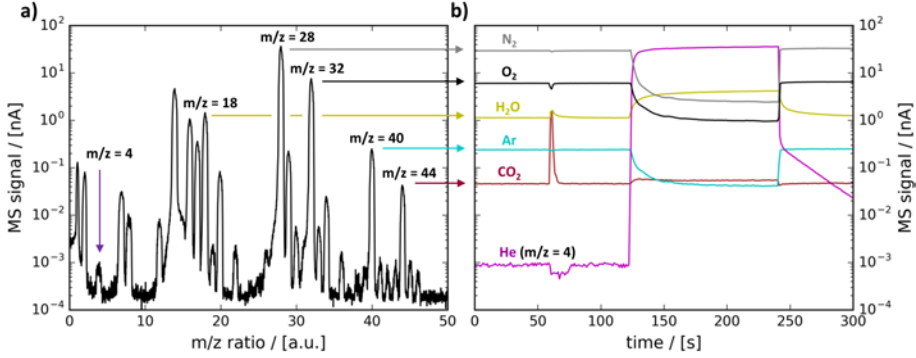
Figure 2.2: a) Mass spectrum of air being sampled through the membrane chip before a droplet of water is placed onto the membrane. **b)** Mass-time analysis of air with N_2, O_2, H_2O, Ar and CO_2 measured on $m/z = 28, 32, 18, 40$ and 44, respectively. At $t \approx 60\,s$ a breath exhale from the user, indicated by a spike in CO_2 and H_2O, is recorded, before the placement of the water droplet at $t \approx 120\,s$, after which the sampling volume equilibrates with water, with He carrier gas making up the pressure to $1\,bar$, measured on $m/z = 4$.

During air exposure the sampling volume continuously equilibrates with the gaseous atmosphere immediately outside the membrane. This is e.g. seen at $t \approx 60\,s$ where the user of the setup exhales a breath of air while leaning over membrane, which is immediately shown as a spike in the H_2O and CO_2 signals at $m/z = 18$ and 44. At $t \approx 120\,s$ a droplet of water is placed on top of the membrane, which causes the sampling volume to saturate with water vapor and fill to $1\,bar$ with helium, instead of ambient air. This is seen by the rise of the He signal at $m/z = 4$. The subsequent drop in N_2 and O_2 signals at $m/z = 28$ and 32 shows the depletion of N_2 and O_2 dissolved in the droplet through the membrane inlet until a steady-state diffusion from ambient to the MS through the thickness of the water droplet is reached.

During continuous analysis of individual MS signals there are two background signals, which influences the ultimate sensitivity of the system: One is the internal detection limit, determined by the background noise at $\sim 10^{-4}\,nA$ in Figure 2.2a, caused by the electronics of the MS, and the other is the presence of any *physical background* signal on the m/z peak being analyzed. The change in the CO_2 being analyzed in Figure 2.2a, is e.g. a perturbation to the already present CO_2 background signal. The membrane chip thus provides an increase in sensitivity over conventional DEMS systems, both due to a higher vacuum collection efficiency and due to smaller physical background signals in the MS.

As the molecular flux across the entire membrane chip, $\dot{N}_0^{\text{chip}}$ is defined by the micro capillary and tuned to $\dot{N}_0^{\text{chip}} = (1.6 \pm 0.3) \times 10^{15}\,\text{molecules/s}$,

the flux for a given analyte species, n, across the membrane chip to the mass spectrometer can be described as:

$$\dot{N}_n^{\text{chip}} = \frac{p_n}{p_{\text{chip}}} \dot{N}_0^{\text{chip}} \, , \qquad (2.2)$$

with $p_{\text{chip}} = 1\,\text{bar}$. This means that water flux to the mass spectrometer is limited to $\sim 5 \times 10^{13}$ molecules/s, which is four orders of magnitude less than in conventional DEMS. A slight variation can arise from changes in gas composition and temperature, which will be described in further detail in chapter 4. The total molecular flux across the membrane chip is given by

$$\dot{N}^{\text{chip}} = \sum_n \dot{N}_n^{\text{chip}} + \dot{N}_{\text{He}}^{\text{chip}} \equiv \dot{N}_0^{\text{chip}} \, , \qquad (2.3)$$

with He constituting most of the flow when few analyte species are present, while being correspondingly suppressed as more analyte species enter the membrane chip.

Also note, that Equation 2.2 is independent of the membrane area, A, as opposed to Equation 1.3 and Equation 1.4, for semi-permeable and porous membrane inlets, respectively, given the fact that the transport across the liquid-gas and gas-vacuum interfaces are decoupled in the membrane chip. This means that the membrane area can be scaled as needed, within certain design limitation as will be discussed in chapter 4. Here, the membrane is designed to be 7 mm in diameter in order to ensure the capture of analyte species from the entire surface of an 5 mm diameter electrode, which will become apparent in the following section.

The membrane chip is incorporated in a larger experimental setup, as shown in Figure 2.3, which allows abrupt switching between carrier gases, control of the chip pressure and ensures a direct coupling to the mass spectrometer. The MS system used throughout this PhD work is a Pfeiffer QMA 125 with a 90 deg SEM and an open axial beam filament ionizing at 100 eV, which is continuously pumped by a 56 l/s (N_2) Pfeiffer TMP (see Figure A.1 for a close-up photo of the MS). This mass spectrometer is not state-of-the-art, but is capable of delivering a dynamic range of 6 orders of magnitude (see Figure 2.2), which is good enough to ensure a theoretical lower detection limit of 1 ppm of a monolayer, given no physical background on the analyte being measured. This will be discussed in further detail later in this chapter.

2.2   Stagnant thin-layer cell

In order to ensure 100 % membrane collection efficiency, the membrane chip is incorporated into a stagnant thin-layer electrochemistry (EC) cell, as seen in Figure 2.4, inspired by the stagnant thin-layer cell from 1993 by Baltruschat and co-workers [31]. To ensure a versatile electrode mounting system the cell is designed to be compatible with the rotating disk electrode (RDE) mounting
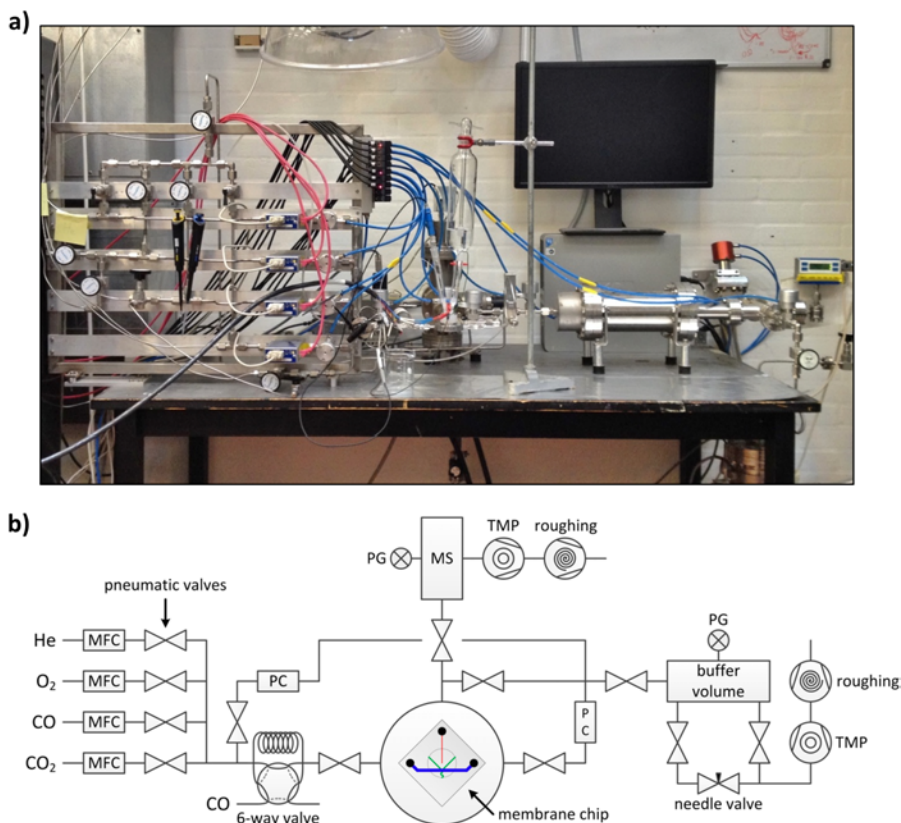
Figure 2.3: a) Photograph of the final state of the EC-MS setup.
b) Diagram of the complete membrane chip EC-MS setup as shown in
a, illustrating the gas handling system both inside and surrounding the
membrane chip. This is used to control carrier gas flow rates and compo-
sition by means of mass flow controllers (MFC), chip pressure by means
of a set of pressure controllers (PC), and ensure a direct coupling to a
mass spectrometer (MS). A 6-way valve is installed on the carrier gas line
to allow $10 - 60\,\mathrm{s}$ pulse injections of reactant gases into the carrier gas
stream. All valves are pneumatic and remotely controlled and pressures
recorded with pressure gauges (PG). The entire setup is controlled us-
ing a LabView control program (see Figure A.2) and all data acquisition
is controlled by an open-source data logging system developed by the
SurfCat group at DTU [61]. The depiction of the membrane chip illus-
trates the diagram of the internal gas system governing the functionality
of the chip. For details on the on-chip gas system, see chapter 4.

system, ChangeDisk RDE, from Pine Resereach Instrumentation [62], which utilizes a PTFE U-cup designed to incorporate 5.0 mm outer diameter disk electrodes. This allows for a high versatility in terms of sample choice as both poly- and single crystalline massive electrodes, as well as thin–film and nanoparticle samples deposited onto e.g. glassy carbon disk substrate electrodes, can easily be measured.

The EC cell is made from Kel-F (PCTFE) and contains a center hole designed to fit an assembled ChangeDisk RDE electrode stick, and four access channels, connecting the top of the cell with the flat cell bottom. In Figure 2.4 the full assembly of the EC cell and the membrane chip is shown together with a schematic illustration of the working principle.

The assembly consists of three steps as depicted in Figure 2.4a-c: First the electrode is inserted into the EC cell by means of the ChangeDisk RDE electrode assembly, as shown in Figure 2.4a. The electrode is mounted so that the electrode surface, the end of the U-cup and the flat bottom of the EC cell are flush within $\pm 10 \mu$m. This alignment is ensured using a mounting block system formed as a negative of electrode, U-cup and EC cell, and is verified using an optical microscope after assembly.

After assembly the EC cell is mounted onto the membrane chip using a $100 \, \mu$m thick PTFE washer as a spacer, which defines the thin-layer working volume of the EC cell, as seen in Figure 2.4b. The height of the working volume, referred to as the working distance, L, and thereby the distance between the working electrode and the membrane, is thus defined by the thickness of the washer. The membrane chip is interfaced with the mass spectrometer and the carrier gas system using an interface-flange designed to have a small internal volume for the gas connections and a large pump way connection to the MS. A set of Viton O-rings is used to make a UHV compatible seal. A 3D rendering of the full assembly can be seen in Figure A.3.

After mounting, the EC cell is filled with electrolyte by introduction through the inlet channel and exits through the remaining three access channels. An external counter electrode (CE) and reference electrode (RE) are then connected opposite of each other perpendicular to the inlet and the last access channel is then connected to an outlet leading to waste. This way a full three electrode setup is established with the the CE and RE on opposite sides of the WE, which results in zero ohmic drop during experiments (valid for small currents, $I \lesssim 1$mA).

During operation, the electrolyte is kept stagnant in the working volume itself allowing for a continuous equilibration between the membrane chip and the thin-layer working volume and thus 100 % collection of reaction product by the membrane, as sketched in Figure 2.4d. If needed, the working volume volume can be flushed with fresh electrolyte through the inlet in between experiments to prevent gradual pH drift, accumulation of non-volatile reaction products or simply in order to change to different electrolytes.

A photograph of the full cell assembly is shown in Figure 2.5 illustrating
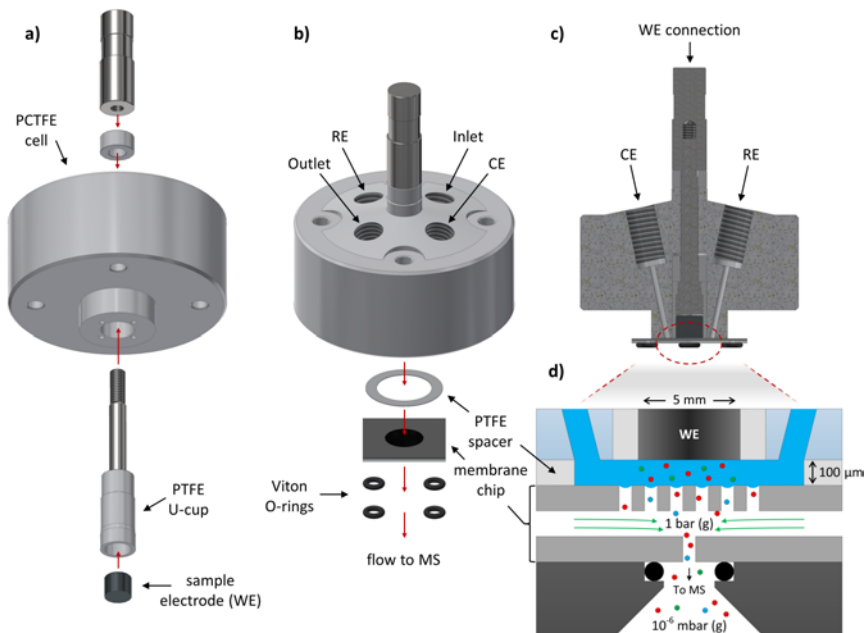
Figure 2.4: Schematic illustration showing the assembly of the stagnant thin-layer electrochemistry (EC) cell. **a)** (bottom view) Mounting of a 5.0 mm outer diameter disk electrode in the EC cell using a ChangeDisk RDE electrode mounting system from Pine Resereach Instrumentation. **b)** (top view) Mounting of the assembled EC cell onto the membrane chip using a 100 μm thick Teflon (PTFE) spacer to define a thin-layer working volume between the electrode and the membrane. Viton O-rings are used to seal the membrane chip to the ultra-high vacuum of the mass spectrometer. Four access channels connect the working volume to an external electrolyte reservoir, a reference electrode (RE) and a counter electrode (CE) using Tefzel (ETFE) Luer adapters (not shown). **c)** (side cut view) Filling of the EC cell with electrolyte, creating a three electrode configuration established with the working electrode (WE) placed in the center above the membrane. **d)** (zoomed side view) Working principle showing how volatile reaction products are captured by the membrane and sent to the mass spectrometer while the carrier gas in turn equilibrates with the working volume. The assembled flow cell and the membrane chip interfaces to the mass spectrometer through an interface flange. The full system assembly can be seen in Figure A.3.
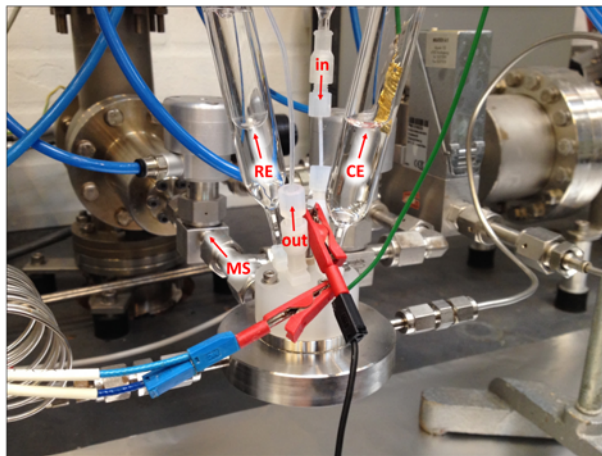
Figure 2.5: Photograph of the full assembly of the stagnant thin-layer electrochemistry cell mounted into the membrane chip. The mass spectrometer is visible in the background in the top left corner of the photograph. This complete is shown in a 3D rendered exploded view in Figure A.3.

how electrolyte is introduced to the EC cell via 1/16 inch PTFE tubing from a water tower (not shown), where the electrolyte can be pre-saturated by e.g. Ar using a bubbler. The reference and counter electrodes are connected via two glass cylinders made with a glass frit and a Luer connector at the bottom. Throughout this PhD work, an Au foil was used as CE and a Hg/Hg_2SO_4 electrode with a potential of $\sim 0.68\,\mathrm{V\,vs\,SHE}$ was used as RE. The RE was frequently calibrated against the RHE potential using a Pt wire and an H_2 saturated electrolyte, as described in chapter 1. All glass and PTFE parts in touch with the electrolyte during experiments are cleaned in strong acids prior to any experiments, in order to keep the system contamination free.

2.3   Experimental procedures

In electrocatalysis the goal is to find out how the catalytic activity of a given catalyst material (electrode) responds to a given electrical input (electric potential, U), as discussed in chapter 1. On the membrane chip EC-MS setup, this is typically done by setting the electrical potential in one of two ways: either by setting a constant potential while recording the electric current and MS signal as a function of time, i.e. *chronoamperiometry* (CA), or by sweeping the potential on a linear ramp, typically in consecutive cycles within a certain potential range, i.e. *cyclic voltammetry* (CV). The former technique has the clear advantage of showing how the catalytic system changes over time, given a constant

input parameter, U, and a time sensitive analysis instrument. The latter is advantageous for investigating phenomena, which are highly dependent on the potential input, e.g. the desorption of strongly adsorbed reaction intermediates.

Figure 2.6 and Figure 2.7 presents a series of experiments, which demonstrate how the above techniques are performed using the membrane chip EC-MS instrumentation. As demonstration reactions the *hydrogen evolution reaction* (HER), *oxygen evolution reaction* (OER) and CO oxidation reaction, all on a polycrystalline Pt electrode in 1.0 M HClO$_4$, will be used. Data from these experiments will furthermore be used to demonstrate quantification procedures later in this chapter, and as input for a mass transport model presented in chapter 3. As the focus of this chapter is on the technique, rather than the catalysis of Pt in itself, the catalytic interpretation of the data will be kept to a minimum. Examples of in-depth electrocatalytic studies will be presented later in this thesis in chapter 5 and chapter 6. Details on the mechanisms of HER, OER and CO oxidation on Pt can be found in [63].

Constant-potential experiments

To exemplify the advantage of constant-potential EC-MS experiments HER and OER was performed on a Pt electrode, as shown in Figure 2.6a and b. Each figure consists of two panels, with the top panel showing mass spectrometry data and the bottom panel showing electrical potential (black) and current (red), all plotted on a shared time axis. This type of plot will from now on be referred to as an EC-MS plot. Each experiments is performed as a two minute constant-potential step at 0.055 V vs RHE and 1.75 V vs RHE, respectively, while resting the potential at 0.45 V vs RHE in between experiments, where no electrochemical processes are expected to happen. H$_2$ is measured by recording the $m/z = 2$ signal in the MS and O$_2$ is measured by recording $m/z = 32$.

As expected, the HER immediately reaches a steady-state, whereas the OER experiment represents a good example of a system, which changes drastically as a function of time. The O$_2$ production decreases towards a lower steady-state due oxidation of the Pt catalyst [64]. This is an example of an electrocatalytic system, which changes dramatically as a function of time, and thus illustrates the importance of keeping the input parameter, i.e. the electrical potential, constant. Without doing so, the response of the catalytic system would convolute into the dynamic change due to the potential change. This phenomenon is in itself also an interesting scientific result, as EC-MS is able to show the actual OER activity on a reduced metal surface in the initial phases prior to oxidation, which can be difficult to obtain otherwise as the electric current is convoluted with the non-faradaic process of double-layer capacitance. A similar behavior has been observed on other metals, as part of this PhD work, but this will be a subject of future studies.

The HER and OER experiments shown in Figure 2.6a and b are both performed in a He saturated electrolyte, ensured by the membrane chip being in
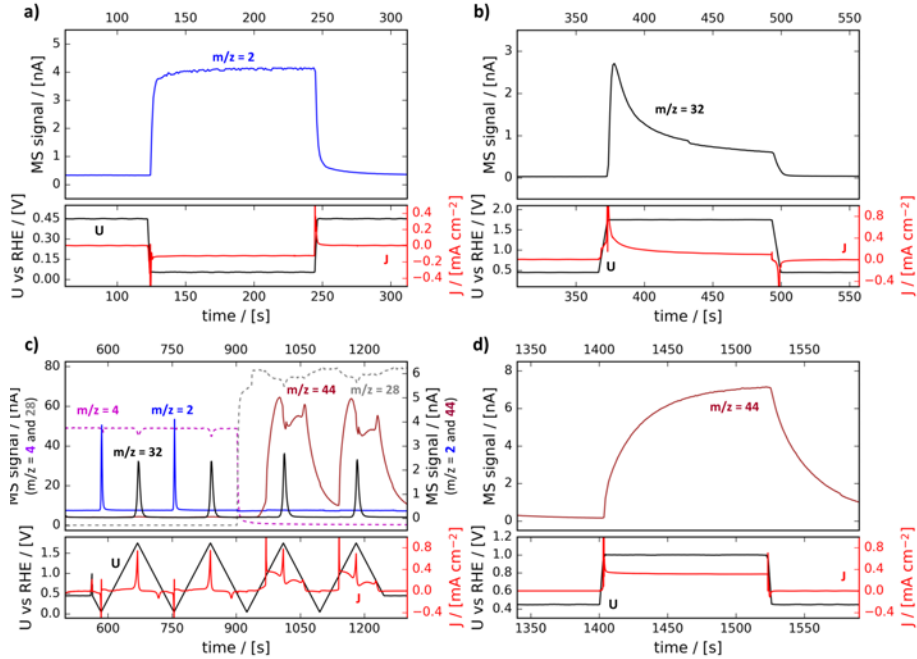
Figure 2.6: Experiment series showing constant potential HER, OER and CO oxidation on a polycrystaline Pt electrode in $1.0\,\mathrm{M}$ HClO$_4$. **a)** Constant-potential HER performed at $0.055\,\mathrm{V}$ vs RHE for two minutes. The potential is reached by a fast ramp at $200\,\mathrm{mV/s}$, to reduce capacitance charging. **b)** Constant-potential OER performed at $1.75\,\mathrm{V}$ vs RHE for two minutes. **c)** Abrupt change of carrier gas from He to CO at $t = 900\,\mathrm{s}$, while cycling the potential between 0.045 and $1.75\,\mathrm{V}$ vs RHE with $20\,\mathrm{mV/s}$. The change is timed to be exactly between the second and third CV cycle illustrating clear suppression of HER by CO poisoning and onset of CO oxidation. **d)** Constant-potential CO oxidation performed at $1.00\,\mathrm{V}$ vs RHE for two minutes. $m/z = 4, 28, 2, 32$ and 44 corresponds to He, CO, H$_2$, O$_2$ and CO$_2$, respectively. This data set has been normalized to the relative H$_2$O signal, due to unexpected space charging caused by a newly installed filament in the MS. These experiments will be repeated before publication in [P2], but the qualitative conclusions remain unchanged.

constant equilibrium with the thin-layer working volume in between the electrode and the membrane. In order to perform experiments with gaseous reactions, e.g. CO oxidation experiments, it is possible to feed reactant gas directly through the membrane chip, by changing the composition of the carrier gas. As a demonstration Figure 2.6c therefore shows the change from He to CO, while cycling the electrode potential between $0.045\,\mathrm{V}$ vs RHE and $1.75\,\mathrm{V}$ vs RHE with

$20\,\mathrm{mV/s}$. With both carrier gas and reactants here co-plotted in the top panel on a linear scale, the y-axis is split in two, with the larger signal (carrier gases) being read off on the left and smaller signals (reaction products) being read off on the right, as indicated in the figure.

The carrier gas is changed abruptly between two consecutive CV cycles, leading to an immediate suppression of HER as the surface sites get blocked by CO poisoning, after which CO oxidation sets in at potentials anodic (towards positive) of $\sim 0.7\,\mathrm{V}$ vs RHE, where CO_2 is measured on $m/z = 44$. The shape of the CO_2 production points to metallic Pt being more active for CO oxidation than PtO, given a higher CO_2 production rate at more cathodic (towards negative) potentials. The plateau reached at more anodic potentials, is due to the mass transport limitation of CO from the membrane to the electrode at these high conversion rates. Interestingly, OER remains largely unchanged during this transition, which is a bit surprising, as both OER and CO oxidation involve the adsorption of OH^- as an intermediate reaction step [63], and thus one would expect them to compete with each other. This has however not been studied in further detail as part of this PhD work. This experiment demonstrates how the membrane chip introduces the ability to control and monitor the dissolved gas atmosphere seen by the electrode to a high degree using the carrier gas system.

After introduction of CO as reactant gas, two minutes of steady-state CO oxidation at $1.00\,\mathrm{V}$ vs RHE is performed. Likewise, steady-state is reached due to the mass transport limitation of CO. One thing to notice both in Figure 2.6c and d, the relatively slow time response in the measurement of CO_2 on the $m/z = 44$ signal, compared to $m/z = 2$ and $m/z = 32$ for H_2 and O_2. This is due to CO_2 being evaporation limited across the membrane chip interface, which will be described in further detail in chapter 3.

Potential sweep experiments

CO stripping on Pt is an example of a transient phenomenon which is highly dependent on the potential input and thus best studied by sweeping the potential using cyclic voltametry. This reaction is well-studied elsewhere, including previous EC-MS studies [63, 65, 66].

The ability to introduce reactant gases into the carrier gas stream of the membrane chip, as shown in Figure 2.6c, allows for transient pulse injections by use of the 6-way valve system shown in Figure 2.3. Thus $10\,\mathrm{s} - 60\,\mathrm{s}$ long pulses of reactant gas can be introduced to the thin-layer working volume in a well controlled manner. On the EC-MS setup, a CO stripping experiment can thereby be performed as shown in Figure 2.7.

First a CV scan is performed between 0.075 at $1.15\,\mathrm{V}$ vs RHE with $20\,\mathrm{mV/s}$ to verify that the Pt electrode behaves as expected, after which a $60\,\mathrm{s}$ long pulse of CO was introduced through the carrier gas stream, while holding the potential of the Pt electrode at $0.45\,\mathrm{V}$ vs RHE, which causes the electrode to be fully poisoned with CO. No residual CO is left in the working volume of the
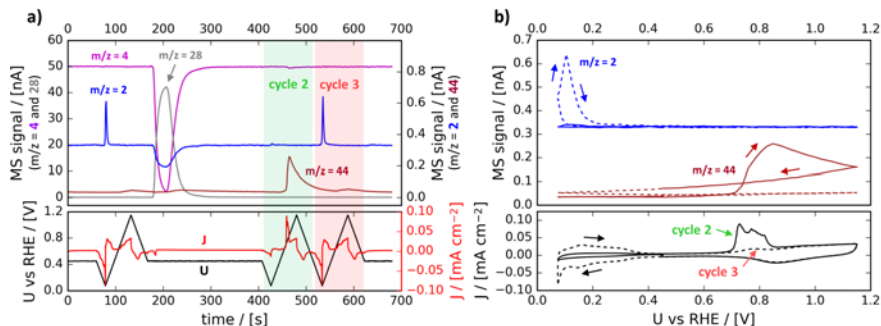
Figure 2.7: a) EC-MS plot of a CO stripping experiments performed on a polycrystaline Pt electrode in $1.0\,M$ $HClO_4$. The top panel of **a)** shows the MS signal for $m/z = 4$, 28, 2 and 44, corresponding He, CO, H_2 and CO_2, respectively, and the bottom panel shows electrical potential and current, all recorded as a function of time. CO is introduced by $60\,s$ pulse injection of CO into the carrier gas stream of the membrane chip at $t \approx 200\,s$, while resting the potential at $0.45\,V$ vs RHE for three minutes. The potential is then scanned first cathodicly to demonstrate CO poisoning and then anodicly $1.15\,V$ vs RHE with $20\,mV/s$ to oxidized the surface adsorbed CO to CO_2. Two complete CV cycles are performed between $0.075\,V$ vs RHE at $1.15\,V$ vs RHE after dosing of CO. The last two CV cycles are plotted in **b)** as an EC-MS plot against potential for comparison, with the second cycle (green) showing the CO stripping and the third cycle (red) showing a clean Pt surface.

EC cell after the pulse has passed through the membrane chip, as seen in the MS signal.

After the pulse injection the potential is scanned cathodic (towards negative) with $20\,mV/s$ to confirm the poisoning (no HER observed) and then anodic (towards positive) to $1.15\,V$ vs RHE to oxidize the surface adsorbed CO off to CO_2. A consecutive CV scan is finally conducted to verify that the electrode is now back to normal. This is apparent in Figure 2.7a by the identical HER activity and electric current signal in the first and third CV cycles. The second (green box) and third (red box) CV cycle are co-plotted for comparison in Figure 2.7b as an EC-MS plot with MS signal and electric current plotted against potential.

Integrating the CO stripping peak yields $\sim 2.1 \times 10^{14}$ CO_2 molecules (integrated charge / $2q_e$), assuming that the pre-annealed Pt electrode used in these experiments has a roughness factor of ~ 1, this corresponds to a surface coverage of $\sim 66\,\%$ given the geometric surface area of $0.196\,cm^2$ of the electrode. This is to be expected, according to literature [23].

The ability to introduce gaseous reactants in a controlled manner as demonstrated here, is unique to the membrane chip and opens up for a large range

of experimental possibilities. Examples of further applications of this will be demonstrated later in chapter 5 and chapter 6.

General advantages and disadvantages of EC-MS

As demonstrated in the above EC-MS is very capable of analyzing desorbing volatile reaction products in real-time during both CA and CV experiments and is thus an extremely valuable tool for coupling charge transfers in faradaic processes to the generation of reaction products. However, more often than not electrochemical processes involve intermediate reaction steps which does not yield volatile reaction species.

As an example, consider e.g. the clean non-poisoned Pt CV Figure 2.7b, cycle 3 (red), bottom panel. Here distinct features at cathodic potentials indicate the under-potential adsorption and desorption of H^+ (H_{UPD}) to the surface prior to the onset of HER around 0.05 V vs RHE and the adsorption and desorption of OH^- as well as Pt oxide formation at more anodic potentials [67]. Besides HER, which evolves reaction products as seen in the experiments above, these are all non-faradaic process yielding a transient electron transfer at the electrode-electrolyte interface, recorded by the current signal in the CV. In between, in the center region of the CV, there is a small current representing the non-faradaic charging of a double-layer capacitance at the interface, yielding an electric current signal without any actual ad- or desorption phenomena occuring. With the introduction of CO, a small displacement current is seen in Figure 2.7a (bottom panel), again a non-faradaic process indicating a coverage of the electrode surface. Upon scanning the potential anodic to ~ 0.7 V vs RHE a clear CO oxidation feature shows up, due to the oxidation of the surface adsorbed CO to CO_2 [63], which again yields the desorption of a volatile reaction species.

In regards to non-volatile reaction products, adsorbates staying on the surface of the electrode, or any changes to the interface or the electrode itself, it is therefore necessary to either interpret the electric current signal indirectly, with the assistance of appropriate models, or use supplementary techniques like e.g. Raman or IR spectroscopy. None of these are part of this PhD work, where the focus is on information gained from electric and mass spectrometric measurements.

It is thus important to remember, that EC-MS is a specific complementary technique, which makes it possible to probe volatile reaction products as they leave the surface of an electrode and isolate these faradaic processes from the ones that form surface species or non-volatile reaction products. This is however in itself a highly valuable insight to gain during electrochemistry studies.

2.4   Quantification

Given a 100 % membrane and vacuum collection efficiency of all volatile electrochemical products, a direct proportionality between the integrated MS signal and the amount of an analyte produced at an electrode is ensured with the membrane chip. Thus for reaction products, which can be produced electrochemically with a known faradaic efficiency, an internal calibration constant, C_n, is straight forward to acquire through this constant of proportionality. For H_2, O_2 and CO_2 this is done by relating the integrated MS signal during a constant potential, or constant current, pulse as shown in Figure 2.6a, to the integrated faradaic current divided by zq_e. The calibration constant for a given reaction product, n, can thus be expressed as:

$$C_n = zq_e \frac{\Delta Q_n^{\mathrm{MS}}}{\Delta Q_n^{\mathrm{el}}} \ , \tag{2.4}$$

where z is the number of electrons involved in the production of that specific product. Repeating this procedure for different potentials, a multi-point integration curve can be generated, as seen in Figure 2.8a. From here the calibration constant, C_n, is given by the slope of the calibration curve. In this figure it is furthermore seen, that a linear relationship exist between the measured MS signal and the amount of an analyte produced, which confirms the assumption of 100 % membrane collection efficiency. The CO stripping experiment in Figure 2.7, where a fixed number of CO_2 molecules were generated is marked by a square in Figure 2.8a.

For reaction products like e.g. CH_4 or C_2H_4 where it is not possible to run an electrochemical process with a known faradaic efficiency to make an internal calibration, it is instead possible to perform an external calibration, using the membrane chip carrier gas system, as proposed in [69] and demonstrated in [P1]. With the membrane chip itself being a well defined vacuum leak, external calibration can be done by dosing a well-defined gas mixture through the membrane chip and into the mass spectrometer. As previously described the molecular flow through the membrane chip is tuned by the micro capillary to be $\sim 1.6 \times 10^{15}$ molecules/s. Thus, by dosing small amounts of analyte into the carrier gas stream, which can be done by use of the external gas manifold shown in Figure 2.3, a calibration curve for any volatile analyte can be acquired. In this case the calibration constant is given by the relationship between the MS signal measured for a given analyte species, and the fraction of analyte, f_n, dosed into the carrier gas times the molecular flow rate through the micro capillary. The calibration constant can thus be expressed as:

$$C_n = \frac{1}{\dot{N}_0^{\mathrm{chip}}} \frac{\Delta I_n^{\mathrm{MS}}}{\Delta f_n} \ , \tag{2.5}$$

As an alternative, it is also possible to obtain estimated calibration constants, C_n, by adjusting the internal calibration constant for e.g. CO_2 using *relative*
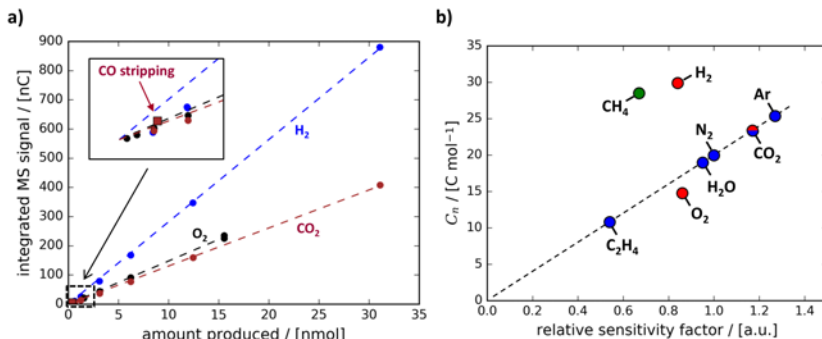
Figure 2.8: a) Internal calibration curves generated for H_2, O_2 and CO_2 from consecutive two minutes constant current pulses at 50, 20, 10, 5, 2, 1, 0.5 and 0.2 μA, respectively. The insert shows the calibration constant generated from the the CO stripping experiment in Figure 2.7, marked as a square. **b)** Calibration constants (red points) acquired from **a** and plotted against relative sensitivity factors (RSF) from [68], normalized to the internal calibration for CO_2 (blue points). The external calibration for CH_4 (green point) is co-plotted to demonstrate that external calibration factors can be approximately obtained within a factor of ~ 2. The external calibration for CH_4 is as well normalized to the internal calibration for CO_2, as external calibrations was performed at a different point in time.

sensitivity factors (RSF) for a generic MS system [68, 70]. RSF values describe the overall transmission function for the MS system, taking the inlet system, i.e. transition from atmospheric to UHV flow regimes (see chapter 4), ionization and cracking probabilities, MS transmission probability and detector efficiency, into account. RSF values therefore vary from system to system and between analyte species and should by used with care.

In Figure 2.8b is the internal calibration constants (red points) obtained from the calibration curves in Figure 2.8a, co-plotted with estimated calibration constants (blue points) obtained from normalized RSF values. The external calibration for CH_4 (green point), obtained as described above, is here inserted for comparison. This illustrates a reasonable correlation between the internal calibration and the generic RSF values for heavier molecules (O_2 and CO_2), whereas lighter molecules (H_2 and CH_4) deviate towards higher calibration values. This is not unusual, as MS transmission tend to increase at lighter masses, following a power law of m^{-1} to m^{-2} depending on the system [25, 71]. Throughout the present PhD work, this calibration methods is estimated be correct within a factor of ~ 2, given the deviation on H_2 and CH_4 in Figure 2.8b.

Prior to calibration of the mass spectrometer, the EC-MS plots throughout this thesis will be presented with raw MS data measured in nA for each m/z

recorded, as done in Figure 2.6 and Figure 2.7, and after calibration the MS signal will be presented in pmol/s for each chemical compound being measured. Indications will be made on which calibration procedure has been utilized for each measurement series.

2.5   Seeking lower detection limits

Measurements performed on the membrane chip EC-MS system tend to yield a higher signal-to-noise ratio than conventional DEMS, given the direct coupling to MS and a low water background. Given 100% vacuum collection efficiency, a higher fraction of analyte is being ionized and detected in the MS and due to a significantly lower water background, physical background peaks are usually less common. It is however difficult to make a true comparison of the lower detection limit between the membrane chip EC-MS and other membrane inlet systems.

In the MIMS literature lower detection limits are typically reported as lower concentration limits, with state-of the-art measurements demonstrating impressive sensitivities in the part-per-quadrillion (ppq) regime [72]. This is however not a fair comparison base, as the total number of molecules involved in saturating the polymer membrane and reaching a steady-state flux to the MS, is enormous, which is often not the case in electrochemical events. This can be thought of, as an "infinite reservoir" lower detection limit.

In the DEMS literature, the detection of a single monolayer of analyte molecule desorbing from the surface of an electrode was proven possible early on through electrochemical CO stripping (as in Figure 2.7) [29]. This is a better metric for lower detection limits, as the total number of analyte molecules there becomes a limiting factor. With monolayer detectibility possible almost from the onset of the DEMS research field, it has however not been a main focus to push the limits even further, which again makes it difficult to compare lower detection limits to present data. As discussed in chapter 1, the anticipated analyte production rate during lab scale electrochemistry is, however, on the order of a single monolayer of desorbing molecules per second. In the present PhD work, this is thus considered the upper detection limit, with sub-monolayer detectibilities sought as the lower. As will be discussed in further detail later in chapter 3, the true advantage of the membrane chip system is seen, when the total amount, or rate of production, of analyte species, is the limiting factor, as it provides the possibility of ionizing a larger fraction of the gas entering the MS.

To establish some representation of the lower detection limit on the membrane-chip EC-MS system, an experiment was therefore conducted on an early iteration of the instrument presented herein, where HER and OER was conducted on two small Pt electrodes ($0.44\,mm^2$ each) in a two-electrode setup configuration (see Figure 4.5). The goal was here to find the lowest possible faradaic current,
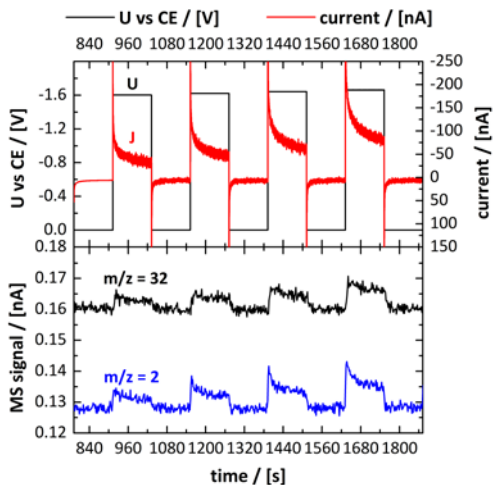
Figure 2.9: Two-electrode water-splitting experiment performed in 0.1 M HClO$_4$ on two 0.44 mm^2 Pt thin–film electrodes. H$_2$ and O$_2$ is here proven quantifiable at faradaic currents down to $\sim$30 nA, though with a signal-to-noise ratio of $\sim$1. This illustrates the lower detection limit of the membrane chip EC-MS systems for analyte species limited by physical backgrounds in the mass spectrometer. Figure from [P1] with an updated color scheme to match this thesis.

during which H$_2$ and O$_2$ evolution was still quantifiable in the MS [P1]. As seen in Figure 2.9, this was found to be $\sim$30 nA, though with a signal-to-noise ratio of $\sim$1 on the MS signal. This detection limit is also normally experienced, within a factor of 2, on H$_2$, O$_2$ and CO$_2$ using the thin-layer cell presented in this chapter, utilizing 45 times larger electrodes with an area of 0.196 cm^2. In the thin-layer cell, this detection limit thus corresponds to the desorption of $\sim$100 ppm of a monolayer per second. For comparison the original DEMS study by Wolter and Heibaum, demonstrated a lower detection limit of $\sim$10 μA using the same sensitivity metric.

H$_2$, O$_2$ and CO$_2$ are, however, all limited by physical backgrounds in the MS. Later in chapter 5, measurements are presented of CH$_4$, measured on the $^m/_z = 15$ signal in the MS, which is not limited by physical backgrounds, and thus illustrate even lower detection limits. In the case of zero physical backgrounds in the MS, the lower detection limit is intrinsically limited by the MS. The quadrupole mass spectrometer used in the present PhD work, delivers a dynamic range of detection of about 6 orders of magnitude below 10^{15} molecules/s (see Figure 2.2), yielding an anticipated lower detection limit of $\sim$1 ppm desorping from a surface per second on a 1 cm^2 electrode. For lower even detection limits, a larger electrode surface area, or a more sensitive MS, is needed. A more qualitative assessment of detection limits and comparison between the membrane chip EC-MS and conventional DEMS, will be discuss in chapter 3.

CHAPTER 3

Modeling

This chapter presents a theoretical model, which describes the transport of analyte molecules from the surface of an electrode to a mass spectrometer, in the membrane chip EC-MS setup presented in chapter 2. This work was done in collaboration with Søren B. Scott, who performed most of the modeling work. The model was established during his Master's project, supervised by Professor Ib Chorkendorff and the author of this thesis. Details on derivations can be found in [73].

This work, together with the instrumental presentation and data shown in chapter 2, constitutes [P2] and is important for understanding the functionality of the membrane chip. This model will both be used to describe the experimental data presented in chapter 2 and will be used as a basis to compare the membrane chip EC-MS system with conventional DEMS.

3.1 EC-MS mass transport model

The transport mechanism of any analyte, n, from the electrolyte above the membrane and into the mass spectrometer can, regardless of the membrane system of choice, be divided into three parts:

1. *Electrolyte transport*, which is governed by diffusion and is in steady-state best described by Fick's first law of diffusion. It describes the molecular flux density, j_n, given the gradient of the concentration, c_n, of a given

analyte species, as:

$$j_n = -D_n \nabla c_n \ , \tag{3.1}$$

where D_n is the diffusion constant. To describe dynamic changes and changes caused by convection in the system, the convection–diffusion equation, can be applied:

$$\left(\bar{v} \cdot \nabla c_n + \frac{\partial c_n}{\partial t} \right) = D_n \nabla^2 c_n \ . \tag{3.2}$$

Here $\bar{v}$ is the flow of the electrolyte, which is zero in the stagnant thin-layer cell [28].

2. *Membrane transport* across the entire liquid–vacuum interface, which is best described by a mass transfer coefficient, h_n, describing the molecular flux density, j_n, across the interface and given a concentration, $c_n(0)$, of that analyte in the liquid immediately outside the membrane, as:

$$h_n = \frac{j_n}{c_n(0)} \ . \tag{3.3}$$

The total molecular flux of a given analyte species across the entire membrane surface, is then given as:

$$\dot{N}_n = A \, c_n(0) \, h_n \ , \tag{3.4}$$

with A being the total membrane area.

3. *Vacuum transport*, which is governed by the free molecular flow of particles inside the vacuum system. For all membrane systems described in this thesis, a high vacuum of at least 10^{-3} mbar is assumed on the low pressure side of the membrane. This results in a mean free path of ~ 10 cm and keeps the backside out of equilibrium ensuring a direct translation of the vapor pressure of analyte inside the membrane into the vacuum on the low pressure side. The transport of gas in the vacuum system itself is best described using kinetic gas theory [74], but in this simple model, however, the vacuum collection efficiency, η_v, is simply used as a metric relating the incoming molecular flow to tolerated flow of $\dot{N}_0^v$ for ideal MS conditions, as described in chapter 1.

With the above strategy, a transport model can now be established for the membrane chip and for conventional DEMS, respectively, as schematically illustrated in Figure 3.1. The formalism used in this chapter also applies directly to polymer membrane based MIMS systems, but the focus will here be on conventional DEMS utilizing differential pumping, and on the membrane chip inlet system presented in chapter 2.
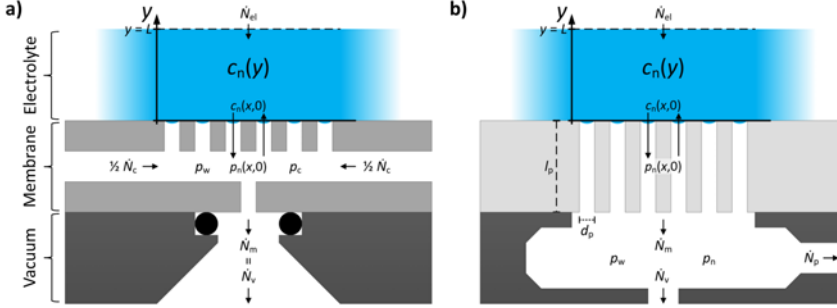
Figure 3.1: a) Stagnant thin–layer mass transport model for the membrane chip inlet system, and **b)** for conventional DEMS utilizing differential pumping.

In order to be able to describe the mass transport within the electrolyte, the membrane and vacuum transport needs to be understood. The following will thus describe the membrane and vacuum transport for the membrane chip and DEMS systems, respectively, in order to establish the mass transport model.

Membrane transport

The membrane transport, and thus the mass transfer coefficient, depends on the specific mechanism driving the transport across a given membrane, as presented in Equation 1.4 and Equation 2.2 for conventional DEMS and the membrane chip, respectively. In both cases the transport relies heavily on the partial pressure, i.e. the volatility, of the analyte species being measured, which relates to the concentration of analyte in the electrolyte immediately outside the membrane through Henry's law of volatility (Equation 2.1). The Henry's law constant vary more than 6 orders of magnitude between analyte species and is thus by far the most dominating parameter governing the membrane transport, as the entire mode of detection in EC-MS relies on analyte reaching the gas phase. As will become apparent in the following model, low volatility can be countered with fast pumping speeds, which is a good argument for using differential pumping, but which at the same time compromises sensitivity.

Using the transport equation for the membrane chip (Equation 2.2), and conventional DEMS (Equation 1.4), as well as Henry's law of volatility (Equation 2.1), a mass transport coefficient for the membrane chip and conventional DEMS, respectively, can be derived as:

$$h_n^{\text{chip}} = K_n^{pc} \frac{1}{p_{\text{chip}}} \frac{1}{A} \dot{N}_0^{\text{chip}} \, , \tag{3.5}$$

and

$$h_n^{\mathrm{DEMS}} = \frac{1}{k_{\mathrm{B}}T} K_n^{pc} \frac{\phi_p}{l_p} \frac{d_p}{3} \sqrt{\frac{8}{\pi} \frac{k_{\mathrm{B}}T}{m_n}} \tag{3.6}$$

Vacuum transport

The vacuum transport depends on the total molecular flux entering the mass spectrometer. This is, according to this model, per definition (or design) limited by $\dot{N}_0^{\mathrm{v}}$. In the membrane chip this total flux constitutes the sum of all analyte and solvent species being extracted, according to Equation 3.4, as well as the flow of carrier gas, as illustrated in Figure 3.1a. Here the flux across the membrane, $\dot{N}_{\mathrm{m}} = \eta_{\mathrm{m}} \dot{N}_{\mathrm{el}}$, according to Equation 1.6, where $\dot{N}_{\mathrm{el}}$ is the production production rate of analyte at an electrode and η_{m} describes the membrane collection efficiency. In a stagnant thin-layer cell as depicted in Figure 3.1, $\eta_{\mathrm{m}} = 1$, as the analyte has no where to go but through the membrane.

As seen experimentally in Figure 2.6, during high rates of HER, OER and CO oxidation the carrier gas flow gets suppressed as more analyte enters the membrane chip. The total molecular flux, $\dot{N}^{\mathrm{chip}}$, to the MS for the membrane chip inlet system can thus be expressed as:

$$\dot{N}^{\mathrm{chip}} = \sum_n \dot{N}_n + \dot{N}_{\mathrm{w}} + \dot{N}_{\mathrm{c}} = \mathrm{const.} \,, \tag{3.7}$$

where the water flux, $\dot{N}_{\mathrm{w}}$, is considered separately, and $\dot{N}_{\mathrm{c}}$ constitutes the flow of carrier gas.

In the DEMS system, the flow across the membrane is similarly given by the sum of analyte and solvent species, whereas the total flow to the MS is regulated by differential pumping through $\dot{N}_{\mathrm{p}}$, as illustrated in Figure 3.1b. In an ideal DEMS system, where differential pumping would be automatically regulated to ensure optimal MS conditions, the total flux, $\dot{N}^{\mathrm{DEMS}}$, to the MS for convententional DEMS can thus be expressed as:

$$\dot{N}^{\mathrm{DEMS}} = \sum_n \dot{N}_n + \dot{N}_{\mathrm{w}} - \dot{N}_{\mathrm{p}} = \mathrm{const.} \,. \tag{3.8}$$

As discussed in chapter 1 is the molecular flux across the membrane for DEMS strictly dominated by water evaporation with $\dot{N}_{\mathrm{w}} \approx 10^{18}$ molecules/s. This is regulated through $\dot{N}_{\mathrm{p}}$ which thereby determines the vacuum collection efficiency $\eta_{\mathrm{v}} \approx 0.001$. In this ideal depiction of a DEMS system, the vacuum collection efficiency depends on the amount of analyte being produced, where analyte is understood to include any dissolved volatile species. Thus, if the solution at the membrane is saturated with a gas, such as air or a purge gas, this will significantly lower the vacuum collection efficiency. In this model, the vacuum efficiency is however strictly calculated from the water evaporation rate.

3.2   Stagnant thin-layer transport model

The diffusive transport of analyte from an electrode to the membrane in the thin-layer cell can be described in 1D with $y = 0$ representing the membrane and $y = L$ representing the electrode, as illustrated in Figure 3.1. The concentration profile in the reaction volume during a pulse of analyte production, $\dot{N}_{el}(t)$ at the surface of the electrode ($y = L$) is described by Equation 3.2, which in 1D with a stagnant electrolyte reduces to:

$$\frac{\partial c_n}{\partial t} = D_n \frac{\partial^2 c_n}{\partial y^2} \ , \tag{3.9a}$$

The boundary conditions for solving this differential equation, can be established by applying Equation 3.1 to the electrode and the membrane, respectively, for a pulse of analyte production at the surface of the electrode lasting from $t = 0$ to $t = t_1$, as:

$$D_n \frac{\partial c_n}{\partial y} = \frac{I_n}{z q_e} = \dot{N}_{el} \qquad \text{for} \quad y = L \ , \quad 0 \le t \le t_1 \tag{3.9b}$$

$$D_n \frac{\partial c_n}{\partial y} = 0 \qquad \text{for} \quad y = L \ , \quad t < 0 \ , \quad t > t_1 \tag{3.9c}$$

$$D_n \frac{\partial c_n}{\partial y} = h_n c_n \qquad \text{for} \quad y = 0 \ , \tag{3.9d}$$

where I_n is the faradaic current and z is the number of electrons involved in the production of analyte species. Through non-dimensionalization (for details, see [73]) the system of equations (Equation 3.9a-d), can be described with a single system parameter, α, representing the ratio between the characteristic evaporation rate across the membrane, h_n, and the steady-state diffusion rate towards the membrane, $\frac{D_n}{L}$, as:

$$\alpha_n = \frac{L\,h_n}{D_n} \ , \tag{3.10}$$

Assuming a step function for the analyte production at the electrode, $\dot{N}_{el}(t)$, the system of equations, Equation 3.9, can be solved analytically using a Laplace transformation (again see [73] for details), which, to the first order, approximates the rise and settling response, respectively, to the step function with an exponential function, as:

$$y = a \exp\left(-\frac{t}{\tau}\right) \quad \text{and} \quad y = a\left[1 - \exp\left(-\frac{t}{\tau}\right)\right] \ , \tag{3.11}$$

with the characteristic time constant,

$$\tau_n = \underbrace{\frac{L^2}{2D_n}}_{\text{diff.}} + \underbrace{\frac{L}{h_n}}_{\text{evap.}} \ , \tag{3.12}$$

in which the system parameter, α, is recognized as (double) the ratio between the two terms. This illustrates that for large values of α_n the system is largely diffusion limited and for small values of α_n the system is largely evaporation-limited.

Preliminary system comparison

The largest difference between the membrane chip and conventional DEMS is the overall pumping speed, which leads to significantly higher mass transport coefficients for DEMS. In Table 3.1, the mass transport coefficient, h_n, as well as the characteristic time constant, τ_n, and system parameter, α_n, are listed for H_2, O_2 and CO_2, respectively, for both the membrane chip and conventional DEMS. The diffusion coefficient, D_n and Henry's law constant, K_n^{pc}, used for derivation, are listed as well. From this comparison, the low pumping speed of the membrane chip becomes apparent. In the stagnant thin-layer cell, assuming a working distance between the electrode and the membrane of $L = 100\,\mu m$, both H_2 and O_2 are however limited by diffusion, and not evaporation, given an $\alpha > 1$. CO_2, however, represents an analyte with sufficiently low volatility to become limited by the membrane chip pumping speed, which is apparent in the slow response time seen experimentally in chapter 2.

Given a much faster pumping speed in the DEMS system, and thereby a significantly larger mass transfer coefficient, H_2, O_2 and CO_2 become largely diffusion limited ($\alpha \gg 1$). Less volatile analyte species like, e.g. EtOH (ethanol), does however cross over and become evaporation limited, even for DEMS, with

Table 3.1: Diffusion coefficient, D_n, and Henry's law constant, K_n^{pc}, for H_2, O_2 and CO_2, respectively, listed together with the mass transfer coefficient, h_n, system parameter α_n, and response time, τ_n, expected in the membrane chip and DEMS systems, assuming an electrode–membrane distance of $L = 100\,\mu m$.

system	n	D_n $[\mathrm{m^2\,s^{-1}}]$	K_n^{pc} $[\mathrm{Pa\,m^3\,mol^{-1}}]$	h_n $[\mathrm{m\,s^{-1}}]$	α_n	τ_n $[\mathrm{s}]$
chip	H_2	4.5×10^{-9}	1.3×10^5	1.8×10^{-4}	3.9	1.7
	O_2	2.1×10^{-9}	8.3×10^4	1.1×10^{-4}	5.4	3.3
	CO_2	1.9×10^{-9}	3.0×10^3	4.1×10^{-6}	0.21	27
DEMS	H_2	4.5×10^{-9}	1.3×10^5	3.1	6.9×10^4	1.1
	O_2	2.1×10^{-9}	8.3×10^4	0.49	2.3×10^4	2.4
	CO_2	1.9×10^{-9}	3.0×10^3	0.015	8.0×10^2	2.6

an α value similar to that of CO_2 for the membrane chip.

At a given analyte production rate of 10^{15} molecules/s in a stagnant thin-layer configuration, the membrane chip will always have higher vacuum collection efficiency than conventional DEMS. This means, that given enough waiting time a higher sensitivity can be obtained, no matter the analyte of interest. The compromise with the time response is however important to consider. In the present membrane chip design, which is limited by a total pumping speed of $\sim 1.6 \times 10^{15}$ molecules/s, as described in chapter 2. CO_2 therefore represents a pragmatic descriptor for the transition between feasible and non-feasible analytes to be analyzed with the membrane chip system. This transition will become more apparent and will be discussed in further detail later in this chapter.

Applying the model to experiments

Applying the entire mass transport model to the experimental results for HER, OER, CO oxidation and CO stripping presented in Figure 2.6 and Figure 2.7 in chapter 2, it is possible to directly compare the anticipated MS signal given an electric current signal to the measured MS signal for each reaction product, as shown in Figure 3.2. The top row of Figure 3.2 shows the generated molecular flux (from $\frac{I_n}{zq_e}$) for H_2, O_2 and CO_2, respectively, assuming $100\,\%$ faradaic efficiency (all current going to a single reaction). The middle row shows the concentration profile in the thin layer of electrolyte between the electrode, with the top ($y = 100\,\text{nm}$) representing the electrode and the bottom ($y = 0$) representing the membrane, as illustrated in Figure 3.1. The concentration profile is a numerical solution to the partial differential equation and boundary conditions in Equation 3.9 [73]. The bottom row shows the measured MS signal (calibrated using internal calibration as described in chapter 2) for H_2, O_2 and CO_2, respectively, co-plotted with the anticipated MS signal (green dotted line) given the molecular flux from the top row as an input to the molecular transport model. All are plotted on shared time axis.

It should be noted, that this model contains zero fitted parameters. The only input parameters used for the transport model are the raw EC-MS data from Figure 2.6 and Figure 2.7, a reaction volume height of $100\,\mu m$, and a mass transfer coefficient for the membrane chip generated from the molecular flow-rate, $\dot{N}_0^{\text{chip}} = 1.6 \times 10^{15}$ molecules/s. As seen in Figure 3.2i-l, the measured MS signals, quantified according to Figure 2.8, correlate very well with the anticipated signal generated by the transport model.

This transport model can be thought of as an operator, which in this case maps a faradaic current measurement into an anticipated MS signal. Given enough confidence in the MS data, it is however possible to instead map the calibrated MS data back to an electric current signal in order to help deconvolute the current measurement and thereby account for individual faradaic processes. This would help in gaining a significantly deeper understanding of
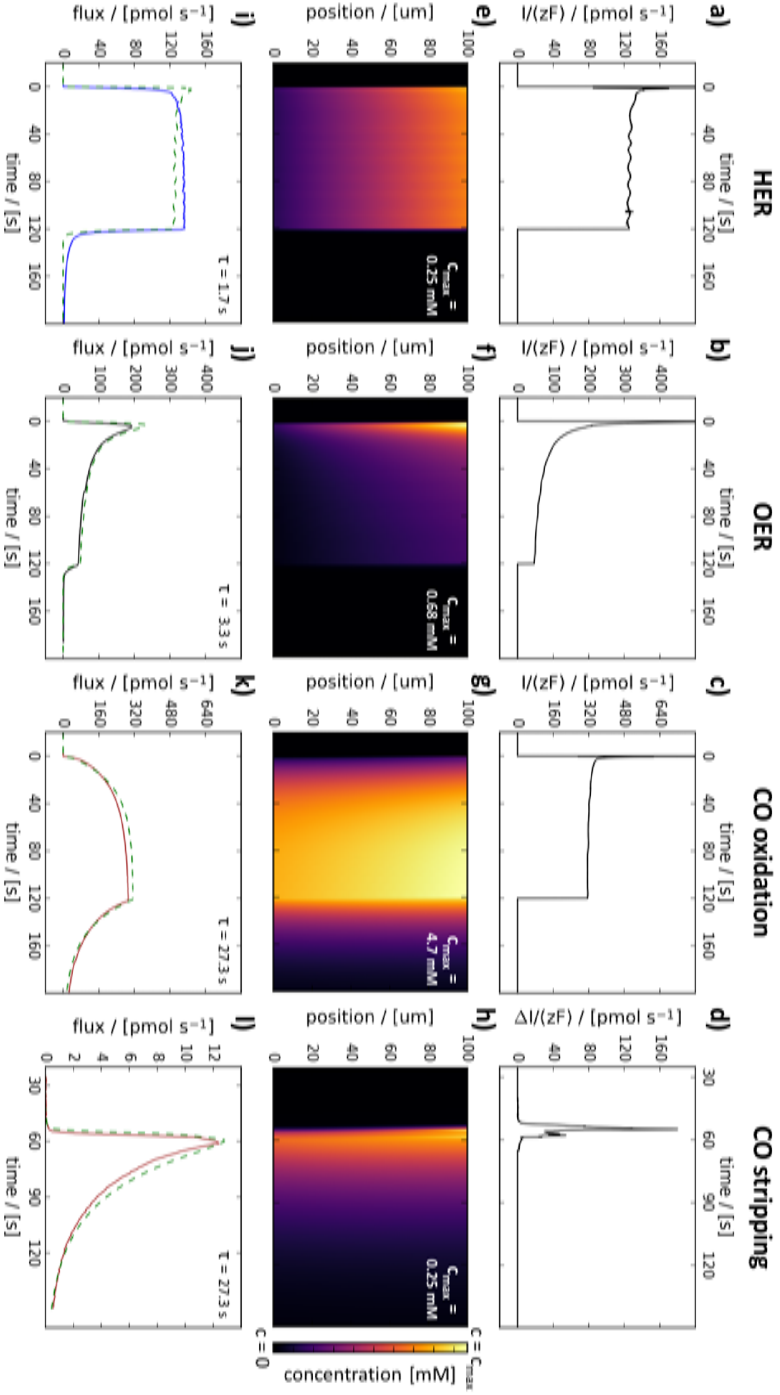
Figure 3.2: Transport model applied to HER, OER, CO oxidation and CO stripping data from Figure 2.6 and Figure 2.7, with each column representing one experiment. The first row, **a-d)**, shows generated molecular fluxes ($\frac{I_{el}}{z\,q_e}$) at the electrode as a function of time. The second row, **e-h)**, shows concentration profiles between the electrode and the membrane as a function of time. This is obtain by a numerical solution to the partial differential equation and boundary conditions in Equation 3.9 [73]. Each contour plot is normalized individually, with c_{max} representing the maximum concentration obtained in each case. The third row, **i-l)**, shows calibrated MS signals, measured (blue, black and brown lines) and anticipated (green dotted lines), with internal calibration constants obtained from Figure 2.8. The model assumes an electrode–membrane distance of $100\,\mu m$ and mass transfer coefficient, h_n^{chip}, based on a molecular flow rate $\dot{N}_0^{chip} = 1.6 \times 10^{15}$ molecules/s.

electrocatalytic reaction mechanisms.

As an example of this matching, a slight overshoot can be seen on the anticipated H_2 and O_2 signals in Figure 3.2i and Figure 3.2j. Presumably these overshoots represent non-faradaic charging of the double-layer at the electrode–electrolyte interface, which, as discussed in chapter 2, represents a non-faradaic process, yielding zero reaction products. Given enough trust in this model, and in the calibration of the membrane chip EC-MS system, it is thereby possible to directly seperate the faradaic HER and OER from the non-faradaic double layer capacitance charging in these experiments.

Coupled with the high sensitivity capabilities of the membrane chip EC-MS system, this represents a highly interesting methodology for future electrochemistry studies: By applying a constant potential step to an electrode, a "rainshower" of analyte species can be produced, of which every molecule is captured by the membrane chip and analyzed by the MS, making the rainshower detectable even with ppm's of a monolayer desorping from the surface. Using the present mass transport model, the measurement can thereafter be mapped directly back to the electrode, yielding insight into the dynamics of the analyzed phenomena. These are however still preliminary data, which will be part of [P2].

Collection efficiency comparison

As discussed above and as illustrated by the comparison in Table 3.1, the large difference in pumping speeds between the membrane chip and conventional DEMS results in a trade-off between response time and sensitivity, with the latter given by a lower vacuum collection efficiency caused by the differential pumping. It is therefore relevant to map out this trade-off in more detail. The best way to do this, is to establish a common comparison base between the membrane chip and DEMS systems. An example of such, is to consider a flow system, in which the time constant, τ is locked in place for all analyte species. This has been demonstrated experimentally through the design of a dual thin–layer flow cell as introduced by Jusys, et al. in 1999 [32], which then introduces a membrane collection efficiency, η_m, as described in chapter 1. The common descriptor in this case becomes the total collection efficiency, η, for the membrane chip and DEMS systems, respectively. This flow cell configuration is however not an experimental subject of this PhD work.

In this model the working volume is moved artificially up stream of an electrolyte flow, F, and the volume above the membrane is instead considered a collection volume where uniformly dispersed analyte, with a concentration, c_0, enters to the left at $x = 0$, as illustrated in Figure 3.3a. This uniform concentration is assumed to be created up-stream by a steady-state product generation, $\dot{N}_{el}$, resulting in $c_0 = \frac{\dot{N}_{el}}{F}$. The concentration profile of analyte $c_n(x, z)$ in the volume above the membrane is then modeled in steady-state in 2D, as the analyte travels through the collection volume with the residence time $\tau_{res} = \frac{V}{F}$ and gets collected by the membrane.

As an addition to the model introduced above, we now introduce convection to Equation 3.9a. In order to simplify the model a uniform velocity field, $v_0 = \frac{F}{Lw}$ is assumed, where w is the width of the collection chamber. This assumption, together with the assumption of a uniform concentration profile, c_0, is known not to be entirely correct, as discussed by Baltruschat and co-workers in [29]. Assuming a $0.5\,mm$ wide and $100\,\mu m$ high channel, and flow rates of $\sim 1\,\mu l/s$ the Reynolds number (Re)[1] is ~ 0.2, which makes the flow highly laminar, where a parabolic velocity profile is expected. These changes would however be expected to affect all membrane systems equally, making the previous assumptions acceptable for a qualitative comparison between the two systems.

In a steady-state 2D configuration, Equation 3.2 reduces to:

$$v_0 \frac{\partial c_n}{\partial x} = D_n \left(\frac{\partial^2 c_n}{\partial x^2} + \frac{\partial^2 c_n}{\partial y^2} \right) \; . \tag{3.13a}$$

The derivative with respect to x is however negligable due to the high aspect ratio of the collection volume. The mass transport at the membrane is treated in the same way as for a stagnant system, and thus the boundary conditions can similarly be establish as:

$$c_n = c_0 \qquad\qquad \text{for} \quad x = 0 \tag{3.13b}$$

$$D_n \frac{\partial c_n}{\partial y} = 0 \qquad\qquad \text{for} \quad y = L \tag{3.13c}$$

$$D_n \frac{\partial c_n}{\partial y} = 0 \qquad\qquad \text{for} \quad x < 0 \; , \quad x > w \; , \quad y = 0 \tag{3.13d}$$

$$D_n \frac{\partial c_n}{\partial y} = h_n c_n \qquad\qquad \text{for} \quad 0 < x < w \; , \quad y = 0 \; , \tag{3.13e}$$

Through non-dimensionalization, this equation system can similarly be described with two dominant system parameters [73]: α_n (as introduced in Equation 3.10), describing the relative influence of diffusion and evaporation, and, $\beta_n = \frac{v_0 L^2}{D_n w}$, which describes the relative influence of convection and diffusion within the collection volume.

Utilizing the flow model introduced above, the total collection efficiency, η, can be modeled for the membrane chip and conventional DEMS, as a function of different parameters. As previously discussed, the most dominant system parameter is the Henry's volatlity constant, especially given a fixed time constant in the collection volume, which gives the analyte a limited time to evaporate and reach the MS.

In Figure 3.3b the overall collection efficiency, η, for the membrane chip and conventional DEMS is plotted on a log-log plot against the Henry's law constant for various reaction products, with a few highlighted in the plot. This plot is

---

[1] A definition of Reynolds number can be found in Equation 4.3 in chapter 4.
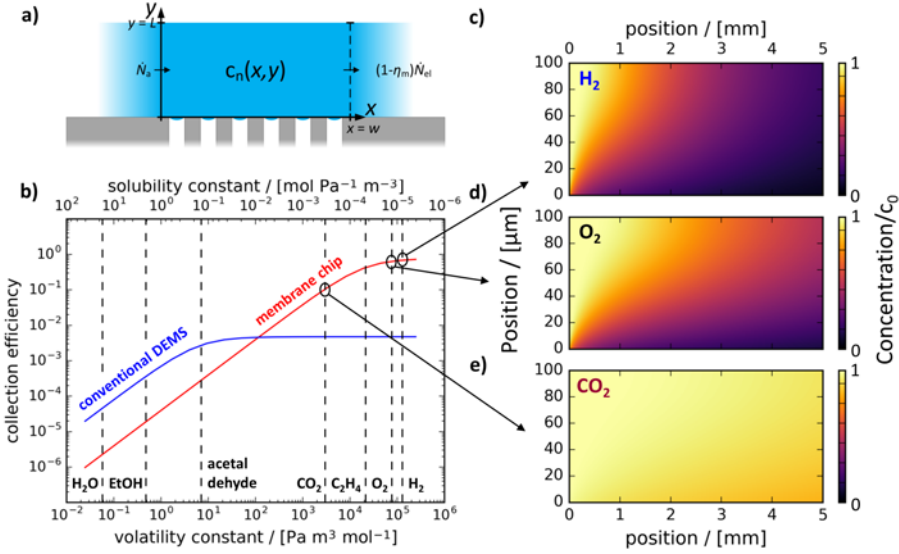
Figure 3.3: a) Schematic of the flow model depicting an incoming flow of electrolyte with an analyte concentration of $c_0 = 1$ at $x = 0$. **b)** Total collection efficiency for the membrane chip (red) and conventional DEMS (blue) as a function of Henry's volatility (bottom) and solubility (top) constants. Henry's constants are plotted for a selection of species for comparison. Values are from [60]. The collection efficiencies are modeled at a flow of $1\,\mu l/s$. **c)** The steady-state concentration profile in the electrolyte volume above the membrane chip for H_2, O_2 and CO_2, respectively. H_2 represents the upper extreme, being largely analyte production rate limited, leading to near $100\,\%$ membrane collection efficiency, and CO_2 represents the lower extreme, being largely evaporation limited, resulting in a continuous probing of the analyte vapor pressure at the membrane interface.

generated for a flow rate of $1\,\mu l\,s^{-1}$, resulting in a $\tau_{res} \approx 2\,s$. In Figure A.4a the same plot is made for various flow rates, which affects both the membrane chip and DEMS system in the same way, namely by allowing more products to be collected at lower flow-rates, and less at higher flow-rates.

From Figure 3.3b it becomes clear that the total collection efficiency decreases for less volatile analyte species, whereas a plateau is reached for more volatile analytes. In Figure 3.3c-e the steady-state concentration profiles in the collection volume above the membrane in the membrane chip system are shown for H_2, O_2 and CO_2, respectively. The upper plateau, which is almost obtained for H_2 as shown in Figure 3.3c, represents a $100\,\%$ membrane collection efficiency regime, which for the membrane chip means $100\,\%$ overall collection efficiency. Here all analyte is collected in both systems during the time period, τ. In Fig-

ure 3.3c this is a apparent by the all dark color at $x = w$, indicating that almost no analyte (yellow) is left after crossing the collection volume. However, since water vapor is continuously being "sampled" in conventional DEMS at a much higher rate than with the membrane chip, even after there is no more analyte to collect, the DEMS overall efficiency drops $\sim$ three orders of magnitude, due to differential pumping. This upper extreme can be thought of as an analyte production rate limited regime, and highlights the importance of matching the molecular flux to the MS, $\dot{N}_0^{\text{v}}$, with the anticipated analyte production rate, $\dot{N}_0^{\text{el}}$, as discussed in chapter 1.

For less volatile species (lower α values), evaporation limitation starts to become dominant, which means that not all analyte manages to get collected during the time period, τ, as seen in Figure 3.3d for O_2. This happens sooner for the membrane chip, as the DEMS system has a higher overall evaporation rate. The lowest evaporation limited extreme, which is almost obtained for CO_2 as seen in Figure 3.3e, in the membrane chip, can be described as an "infinite reservoir" regime, where a gradient across the thin-layer is never really obtained. In this case, the bulk concentration of a given analyte simply translates through the inlet system and into the mass spectrometer, according to Henry's law of volatility (Equation 2.1).

The reason for the crossover leading to a lower collection efficiency for the membrane chip in the low volatility region compared to DEMS, is that membrane chip operates a 1 bar of pressure in sampling volume, constituting mostly helium. In DEMS, the molecular flow to the MS constitutes only analyte and water vapor being sampled from the differentially pumped pre-chamber in the vacuum system. The membrane chip samples the equilibrium vapor pressure at 1 bar of chip pressure, resulting in a ~ 30 times lower collection efficiency, given by the ratio between the analyte vapor pressure and the chip pressure in the infinite reservoir limit. This is however simultaneously the same mechanism, which leads to water evaporation being suppressed by the membrane chip, which in turn leads to a much higher sensitivity.

From Figure 3.3 it follows, that there is an inherent trade-off to consider between total collection efficiency, which is a direct measure of the ultimate system sensitivity, and the time constant for the measurement.

3.3 Opportunity for improvement

With the membrane chip being fabricated using standard clean-room microfabrication techniques, there is a high degree of freedom in the design of the inlet system, as will be described in more detail in chapter 4. It is thus valid to discuss potential future adjustments and how they would compare with conventional DEMS.

Increasing pumping speed

The main limitation of the membrane chip inlet is the slow pumping speed, which inherently help to keeping the water flux down, but thereby also hinters the transport of less volatile reaction species, as discussed above. The most straight-forward way to circumvent this, is by simply increasing the pumping speed by adjusting $\dot{N}_0^{\text{chip}}$. This can be done as needed, given the design scheme presented in chapter 4, and thus any intermediate configuration in between conventional DEMS (blue) and the current membrane chip (red) in Figure 3.3b can be obtained. This would then be at the expense of either differential pumping, or the application of a larger vacuum pump system and a more delicate tuning of the ionization conditions. The latter does however suggest the intriguing possibility of tuning the "entire" transmission function of the MS, all the way from neutral (non-ionized) dissolved analyte species to the detector, to enable as high a pump rate ($\dot{N}_0^{\text{v}}$) as possible, with as high an analyte ionization and detection probability as possible. Many of these optimization parameters would benefit both conventional DEMS and the membrane chip, but the latter introduces a much higher degree of tuneability, as will become apparent later in chapter 4.

Decreasing membrane chip pressure

Another possibility is to change the pressure in the membrane chip and thereby transition from having He (or a reactant gas) as carrier gas, to using water vapor as a "carrier gas". In the extreme case, the chip pressure can be set to 30 mbar and carrier gas can be omitted all together. In Figure 3.4a a log-log plot of the total collection efficiency has been generated for different membrane chip pressures, with the solid line being the same as in Figure 3.3b. As $\dot{N}_0^{\text{v}}$ still allows $\sim 10^{15}$ molecules/s, this would allow for a relatively larger pumping speed on less volatile analyte species. A system similar to this has been developed by Koper and co-workers [34], who designed an OLEMS (pinhole) inlet system with a large porous PTFE membrane. This omission of carrier gas all together however poses the problem of pre-saturating the electrolyte for electrochemistry measurements. In the case of the stagnant thin-layer cell design, it would therefore not be possible to run experiments with reactant gases, and with dual thin-layer flow cell systems, a pre-saturated electrolyte would still feed 1 bar of "carrier gas" into the mass spectrometer, as the down stream membrane is inherently designed to collect gaseous species from the electrolyte. Having the feed of dissolved gases into the MS under control, by using the same carrier gas as used to pre-saturate the electrolyte, can thus be beneficial.

Increasing interface temperature

In any membrane inlet system, the most critical transfer step is the transfer from the dissolved phase to the vapor phase, which is necessary for ionization
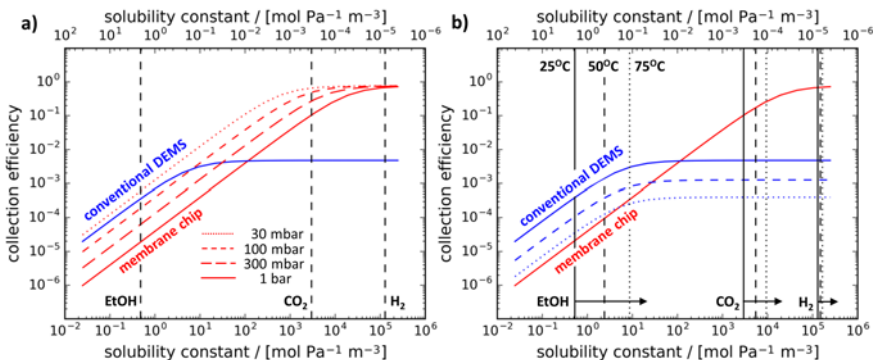
Figure 3.4: Total collection efficiency for the membrane chip (red) and conventional DEMS (blue), plotted as a function of **a)** membrane chip pressure and **b)** temperature of the liquid–gas interface. The solid line of both the membrane chip and conventional DEMS in both figures, is the same line as presented in Figure 3.3.

and detection in the mass spectrometer. A straight-forward way to increase the vapor pressure is to increase the temperature of the liquid–gas interface. With conventional DEMS this, however, results in an increase in the water vapor pressure, which lowers the vacuum collection efficiency for DEMS and thereby gives the membrane chip an advantage. The water vapor pressure does also change in the membrane chip, which can result in larger physical background signals in the MS, but the total molecular flux to the MS remains unchanged. The Henry's solubility constant for a given analyte, n, scales with temperature according to:

$$H_n^{cp} = H_0^{cp} \exp\left[-\Delta H_{\text{sol}}\left(\frac{1}{T} - \frac{1}{T_0}\right)\right] , \qquad (3.14)$$

where H_0^{cp} is the Henry's solubility constant at $T_0 = 298.15\,\text{K}$ and $-\Delta H_{\text{sol}}$ is the enthalpy of dissolution. A compilation of values for H_0^{cp} and $-\Delta H_{\text{sol}}$, can be found for 4632 different species in [60]. The solubility constant is inversely proportional to the volatility constant defined in Equation 2.1, as $H_n^{cp} = \frac{1}{K_n^{pc}}$.

In Figure 3.4b the collection efficiency for the membrane chip and conventional DEMS are plotted at different temperatures, with the Henry's volatility constants for EtOH, CO_2 and H_2 adjusted accordingly. This illustrates, that by increasing the interface temperature, larger pumping speeds can be obtained for the membrane chip for low volatility compounds, which would otherwise highly evaporation limited.

Design and development

This chapter presents the design considerations involved in the development of the membrane chip EC-MS system presented in chapter 2. The development process revolves around three main parts of the instrumentation: 1) the permeable interface between an electrochemical test environment and UHV, i.e. the membrane chip itself, 2) the interfacing of the membrane chip to UHV, as well as the associated gas and vacuum infrastructure, and 3) the introduction of the working electrode, i.e. the electrochemistry cell configuration.

The following chapter is meant to establish the framework surrounding the development process leading to the system design presented in chapter 2 and thereby establish a good foundation for further development of the system in the future. Aside from the above mentioned main topics, there will thus be an added focus on both theoretically proposed and experimentally tested future development ideas.

The clean-room fabrication work of the membrane chips presented herein has been performed by Thomas Pedersen, Jesper Yue Pan and Anil H. Thilsted. Chip design, system development and UHV work was done by the author of this thesis.

4.1 Membrane chip design

The idea of the membrane chip originates from work done on silicon based microreactor systems by Henriksen, Vesborg and Olsen in the period 2007-2010 [69, 75, 76]. During this period a large part of the microfabrication scheme for

construction of liquid–vacuum interfaces was developed.

The membrane chip is built around a "T-type" gas handling system inspired by a microreactor platform previously developed by the SurfCat group at DTU [77]. The fundamental idea is to couple a sampling volume, with a well-defined gas composition and pressure, directly to a mass spectrometer. In the case of the microreactor platform the sampling volume is acting as a reaction chamber, loaded with a catalyst, and in the case of the membrane chip, the sampling volume is used as an equilibration zone, equilibrating with an outside test environment through a membrane in the top, as discussed in chapter 2.

A schematic depiction of the key components in the T-type gas system in the membrane chip, is presented in Figure 4.1. The fundamental idea of this gas system is to establish a continuous flow of carrier gas from a well-defined source into the vacuum of the mass spectrometer, while maintaining control of pressure and gas composition in each part of the system. This is done in the following way: First, a well-defined carrier gas composition and pressure is established in a large *reservoir channel* (blue) by controlling the flow at the inlet and setting the pressure at the outlet using conventional gauging equipment. From here carrier gas is continuously pulled through an *inlet channel* (green), through the *sampling volume* (purple), in which it equilibrates with an outside test environment across a *permeable membrane* (dotted line), and lead into a mass spectrometer via a flow restricting *micro capillary* (red). The latter is designed to deliver a pressure drop all the way from the ~ 1 bar in the sampling volume and down to the $\sim 10^{-6}$ mbar in the MS, consequently governing the flow-rate in the upstream sections. The upstream sampling volume and the carrier gas inlet channel are thus designed to induce as little a pressure drop as possible, given the flow rate set by the down-stream capillary. This way, the pressure set in the upstream reservoir channel is representative for the pressure in the sampling volume.

Design parameters

In order to obtain the above mentioned functionality, a range of design parameters needs to be considered for each section of the gas system. These are presented in the following.

1. *Reservoir channel* (blue): Serves the purpose of establishing a well-defined reservoir point, from which carrier gas can be pulled to supply the downstream gas system. This is best obtained by establishing a flow channel, which is wide enough that the pressure drop from the connection point to the pressure control on the outlet becomes negligible at anticipated flow-rates, but with a small enough volume, that the gas composition and pressure can be updated fast. This is typically designed for $\sim 1 - 10$ ml/s at ~ 1 bar, which makes it easy to control the system with standard *mass flow controllers* (MFC) and *pressure controllers* (PC).
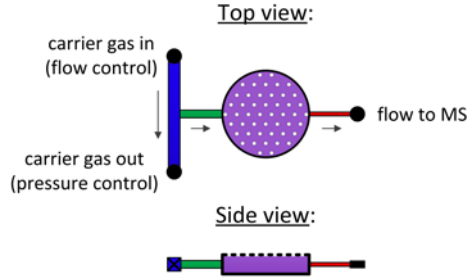
Figure 4.1: Symbolic representation of the membrane chip designed as a "T"-shaped gas system consisting of a main carrier gas reservoir channel (blue), a carrier gas inlet channel (green), a sampling volume (purple), a permeable membrane (dotted line in the side view), and a micro capillary connection to UHV (red).

2. *Inlet channel* (green): Serves the purpose of preventing back-diffusion of analyte from the sampling volume out into the carrier gas reservoir channel, thus ensuring a 100 % collection efficiency from the sampling volume and into the MS. The molecular flow rate $\dot{N}_0$ is determined by the downstream micro capillary. Thus for a given $\dot{V}_0 = \dot{N}_0 \frac{k_{\mathrm{B}}}{T}$, back-diffusion is prevented by ensuring an average flow velocity higher than the average back-diffusion velocity. This is obtained by reducing the cross sectional area of the gas inlet channel. The low cross sectional area should however not induce too high a pressure drop, in order for the set pressure to be representative of the actual pressure in the downstream sampling volume.

   Using the convection-diffusion equation from chapter 3 the fraction of analyte entering the mass spectrometer, and thus the membrane chip vacuum collection efficiency, η_{v}, can be derived as:

$$\eta_{\mathrm{v}} = 1 - \exp\left(-\frac{\dot{N}\,l}{c_n\,A\,D}\right) , \tag{4.1}$$

   where l and A are the length and cross sectional area of the inlet channel, respectively, and the analyte concentration, $c_n = x\frac{p}{k_B T}$, with x being an anticipated fraction of the sampling volume gas being analyte, which here can be approximated to $\sim$50 %. In the membrane chips presented herein, $\eta_{\mathrm{v}} \approx 1$ per design.

3. *Sampling volume* (purple): Serves as an equilibration, or "buffer", zone between the liquid–gas interface and the connection to the MS. This equilibration should be fast compared to any other time constant in the system, which is ensured by a high aspect ratio of the sampling volume. This in turn ensures the support of a large liquid–gas interface area, which ulti-

mately leads more analyte being sampled in flow cell configurations (see Figure A.4b) and allows for larger electrodes in the thin-layer EC cell system presented in chapter 2. In order to ensure a representative sampling of analyte into the MS, the residence time $\tau_{\mathrm{res}} = \frac{V}{V_0}$ should be small compared to the analyte transport time in the liquid above the membrane. A residence time of $\sim 1\,\mathrm{s}$ will for most systems suffice. The volume of the sampling volume should thus be as small as possible, with as high an aspect ratio as possible, but at the same time induce a minimal pressure drop from the carrier gas entry point and across the membrane to the micro capillary.

4. *Permeable membrane* (dotted line): Serves the purpose of establishing a stable (chemically and mechanically) and permeable liquid–gas interface. The time-constant for analyte transport across this interface should be small compared to transport times in the rest of the membrane chip and in the liquid above. For aqueous electrolytes this can be achieved by making a porous and hydrophobic membrane, which suspends a water meniscus across the pore structure by capillary forces (surface tension) [78]. Chemical resistance often relates to surface energy (low surface energy = strong capillary forces), with fluorine-terminated surfaces thus being good candidates.

A critical parameter for porous membranes is the burst pressure, at which the suspended meniscus can no longer be sustained. This depends on three important parameter: The surface tension, γ, of the electrolyte, the contact angle, θ, of the electrolyte to the membrane material and the geometry, or diameter, a, of the membrane pores. Only electrolytes with a contact angle of more than 90 degrees, which forms a curved liquid meniscus at the pores, are usable with such a membrane. Surface costs energy, and the extra surface created by this curvature relates to the contact angle and the radius of the pore, resulting in a net burst pressure of (from the Young-Laplace equation and a bit of trigonometry [79]):

$$\Delta p_{\mathrm{burst}} = \frac{\cos(180° - \theta)}{2a}\gamma \; . \tag{4.2}$$

In the membrane chip presented in chapter 2, where the chip pressure is matching the ambient and no net pressure gradient is exerted onto the liquid–gas interface, rather large pore size of $\sim 3\,\mu\mathrm{m}$ was used, which results in a large liquid–gas interface and eases fabrication. This results in a burst pressure of $\Delta p_{\mathrm{burst}} \approx 33\,\mathrm{mbar}$. In order to be capable of lowering the chip pressure to e.g. the vapor pressure of water, as discussed in chapter 2, a pore size of $\sim 20\,\mathrm{nm}$ is needed, which is standard for Gore-Tex materials and also obtainable with microfabrication. This has however not been explored as part of this PhD work.

5. *Micro capillary* (red): Serves the purpose of inducing the entirety of the pressure drop from the pressure set in the sampling volume (1 bar) to the 10^{-6} mbar operation pressure in the MS. As discussed in chapter 1, this depends on the vacuum pump system, but corresponds to $\sim 10^{15}$ molecules/s given a standard turbo molecular pump with a pumping speed of $\sim 50\,\text{l/s}$ on all relevant gas species. Ideally the micro capillary should be $100\,\%$ non-discriminating, which is difficult to ensure in the crossing from a continuum (viscous) flow to a molecular dominated flow regime [80]. A theoretical treatment of the capillary flow, as well as the general gas flow in the upstream gas system, will be presented later in this chapter.

From atmospheric pressure to UHV

The nature of the gas flow in the gas system presented in Figure 4.1 changes dramatically as the pressure transitions from atmospheric pressure ($\sim 1\,\text{bar}$) to UHV ($\sim 10^{-6}$ mbar). At atmopheric pressure a gas is "dense" and can be described as a continuum by averaged gas parameters like mass density, ρ, and dynamic viscosity, ν. This regime is thus often denoted as the viscous flow regime. At lower pressures, however, the average distance between molecules become so large, that the behavior of individual molecules starts dominating the flow. This regime is therefore denoted the molecular transport regime [81].

In order to be able to design the correct geometry of each section in the gas system presented in the above, an understanding of the underlying theory describing flows in the viscous and molecular regime, as well as in the transition between the two, is required. Therefore, in the following, the key equations governing the gas flow of a membrane chip gas system, will be presented.

In the viscous flow regime, gas flow can either be laminar or turbulent, depending on whether inertial or frictional forces are more dominant. This can be determined by the Reynolds number, Re, as:

$$\text{Re} = \frac{\rho v_0 l_0}{\nu} \ , \tag{4.3}$$

where v_0 is the flow velocity of the gas and l_0 is a characteristic length scale of the system, which for an arbitrary flow channel can be set to $l_0 = \frac{4A}{P}$, where A is the cross sectional area and P is the length of the cross sectional perimeter. For a circular cross sectional geometry, l_0 corresponds to the diameter of the channel. In practice all flows in the membrane chip system are laminar, given the small size scale of the channel system.

The transition from the viscous to the molecular flow regime depends on the *mean free path*, λ, of the molecules at a given pressure and can be calculated as:

$$\lambda = \frac{k_B T}{\sqrt{2}\pi\sigma^2 p} \ , \tag{4.4}$$

where σ is the kinetic diameter of the molecules. The transition to the molecular regime can be approximated to happen when the mean free path of molecules is comparable to the characteristic size, l_0, which can be described by the Knudsen number, Kn, as:

$$\text{Kn} = \frac{\lambda}{l_0} \; . \tag{4.5}$$

The flow is viscous and laminar if Re < 1100 and Kn < 0.01, and the flow is considered molecular if Kn > 1. In between, at 1 > Kn > 0.01, lies the transitional flow regime, in which flow is governed by viscous and molecular parameters simultaneously [74, 82].

Viscous flow through a circular duct with a radius, a, can be described as:

$$\dot{N}_{\text{vis}} = \frac{1}{k_B T} \frac{\pi}{8\nu} \frac{a^4}{l} \bar{p} \left(p_1 - p_2 \right) \; , \tag{4.6}$$

where $\bar{p} = \frac{p_1 + p_2}{2}$ represents the mean pressure in the channel and corrects for the compressibility of the gas and can be neglected for incompressible fluids or for slow gas flows. The pre-factor $G_{\text{h}} = \frac{\pi}{8\nu} \frac{a^4}{l}$ is the hydraulic conductance, which purely depends on the geometry of the gas channel and the dynamic viscosity, ν, of the gas. In Table 4.1 a list of G_{h} pre-factors for the relevant geometries can be found.

For a given molecular flow, $\dot{N}_0^{\text{chip}}$, through the membrane chip channel system, the pressure drop in each section upstream can be derived from Equation 4.6, and using G_{h} pre-factors, from Table 4.1, as:

$$\Delta p = p_1 - \sqrt{p_1^2 - 2 k_B T \dot{N}_0 \frac{1}{G_{\text{h}}}} \; . \tag{4.7}$$

In the molecular flow regime, the flow is best described with kinetic gas theory [74, 82], where for a circular duct, the molecular flow rate is given by:

$$\dot{N}_{\text{mol}} = \frac{1}{k_B T} \frac{2\pi}{3} \frac{a^3}{l} \bar{v} \left(p_1 - p_2 \right) \; , \tag{4.8}$$

where $\bar{v} = \sqrt{\frac{8 k_B T}{\pi m}}$ is the mean thermal velocity of the gas molecules and m is the molecular mass.

The transitional flow regime can now be described as a linear combination of a viscous flow (Equation 4.6) and a molecular flow (Equation 4.8), as:

$$\dot{N}_{\text{tran}} = \dot{N}_{\text{vis}} + \dot{N}_{\text{mol}} \frac{1 + 2 \frac{32}{3} \sqrt{\frac{2}{\pi}} \frac{\dot{N}_{\text{vis}}}{\dot{N}_{\text{mol}}}}{1 + 2.48 \frac{32}{3} \sqrt{\frac{2}{\pi}} \frac{\dot{N}_{\text{vis}}}{\dot{N}_{\text{mol}}}} \; , \tag{4.9a}$$

Table 4.1: List of hydraulic conductances for a set of geometries relevant for the membrane chip gas system [78].

Shape		G_{h}
Circle		$\dfrac{\pi}{8\nu}\dfrac{a^4}{l}$
Two parallel plates		$\dfrac{1}{12\nu}\dfrac{h^3 w}{l}$
Rectangle		$\dfrac{1-0.63(h/w)}{12\nu}\dfrac{h^3 w}{l}$
Square		$\dfrac{1}{28.4\nu}\dfrac{h^4}{l}$

corresponding to

$$\dot{N}_{\mathrm{tran}} = \frac{1}{k_B T}\frac{1}{l}\left(\frac{\pi}{8\nu}a^4\bar{p} + \frac{2\pi}{3}a^3\bar{v}\frac{1+2\frac{2\sqrt{2}}{\sqrt{\pi}}\frac{a}{\nu}\frac{\bar{p}}{\bar{v}}}{1+2.48\frac{2\sqrt{2}}{\sqrt{\pi}}\frac{a}{\nu}\frac{\bar{p}}{\bar{v}}}\right)(p_1 - p_2) \ , \qquad (4.9\mathrm{b})$$

where the pre-factors $2\frac{32}{3}\sqrt{\frac{2}{\pi}}$ and $2.48\frac{32}{3}\sqrt{\frac{2}{\pi}}$ come from experimental fits [74, 82]. From previous works with micro capillary flow [77,83], it has been found, that due to the last section of the capillary experiencing a purely molecular flow, a correction is needed to obtain a full description of the transition from atmospheric pressure ($\sim 1\,\mathrm{bar}$) to UHV ($\sim 10^{-6}\,\mathrm{mbar}$). The capillary flow, $\dot{N}_{\mathrm{cap}}$, from the viscous to the fully molecular regime, can thus be derived as a linear combination of $\dot{N}_{\mathrm{tran}}$ (Equation 4.9b) and $\dot{N}_{\mathrm{mol}}$ (Equation 4.8), as:

$$\dot{N}_{\mathrm{cap}} = \frac{1}{k_B T}\frac{1}{l}\left(\left(\frac{\pi}{8\nu}a^4\bar{p} + \frac{2\pi}{3}a^3\bar{v}\frac{1+2\frac{2\sqrt{2}}{\sqrt{\pi}}\frac{a}{\nu}\frac{\bar{p}}{\bar{v}}}{1+2.48\frac{2\sqrt{2}}{\sqrt{\pi}}\frac{a}{\nu}\frac{\bar{p}}{\bar{v}}}\right)(p_1 - p_{\mathrm{tran}}) + \frac{2\pi}{3}a^3\bar{v}\,(p_{\mathrm{tran}} - p_2)\right) \ ,$$
$$(4.10)$$

where the transition pressure p_{tran} is defined as the pressure at which the mean free path (Equation 4.4) is equal to the diameter of the micro capillary, $\lambda = 2a$:

$$p_{\mathrm{tran}} = \frac{k_B T}{2\sqrt{2}\pi\sigma^2 a} \quad \text{and} \quad \bar{p} = \frac{p_1 + \bar{p}_{\mathrm{tran}}}{2} \ . \qquad (4.11)$$

This equation has been experimentally verified as part of the microreactor development at SurfCat [77,83], as well as for an early iteration of the membrane chip design [79].

The governing equations presented in the above, can now directly be used to construct any desired geometry satisfying the design constraints presented in the beginning of this chapter. In order to do this specifically, a Python script was generated as part of this PhD work, which evaluated the performance of a membrane chip, given a set of geometrical parameters for each distinct section of the gas system, according to the schematic depiction in Figure 4.1.

Microfabrication

In principle the general concept of a membrane chip, as presented in Figure 4.1, can be realized in many ways, but through microfabrication it is possible to routinely create structure on the small (micrometer) size scale needed to satisfy the design constraints introduced above. Furthermore, Si and SiO materials exert good UHV properties and allow for clean surfaces with low sticking coefficients to be formed. All membrane chips developed as part of this PhD work were fabricated according to the same recipe, with minor adjustments to the overall microfabrication scheme. The fabrication scheme for the final iteration of the membrane chip can be found in section A.4. For further details on membrane chip fabrication, see [75, 79].

The microfabrication starts from a *silicon-on-insolator* (SOI) wafer, which consist of a thin layer of SiO_2 sandwiched in between two Si waters, with the top wafer referred to as the *device layer* and the bottom referred to as the *handle wafer*. The SOI wafer used herein is made of a thin $10\,\mu m$ device layer, a $3\,\mu m$ buried oxide layer (BOX) and a thick $\sim 350\,\mu m$ handle wafer. Two distinct etching techniques are then used to construct the membrane chip: dry *deep reactive ion etching* (DRIE), which preferably etches the Si and not SiO_2, and thereby can be used to make vertical structure in either the device layer or handle wafer on the front and back side, respectively; and wet *hydrofluoric acid etching* (HF), which preferably removes the SiO_2 and thereby can be used to etch away the inner BOX layer in the middle of the wafer.

The fabrication strategy is the following: First the porous membrane structure is etched into the thin device layer on the front side, until the BOX layer in the middle is reached. Then all gas channels are etched into the handle wafer on the backside, with deep through-holes reaching all the way through until again reaching the BOX layer in the middle. Then the entire wafer is etched with HF, which preferentially removes the center BOX layer and thus forms the sampling volume with a height of $3\,\mu m$ (defined by the thickness of the BOX layer) underneath the membrane. This step is timed in order to form a support structure underneath the membrane, ensuring mechanical stability. Finally a Pyrex wafer, with three through holes cut out by a CO_2-laser, is anodically bonded onto the handle wafer on the back side, in order to seal off all gas channels. In the end the entire wafer is covered with perfluorodecyltrichlorosilane (FDTS) using molecular vapor deposition (MVD), to make the membrane pores hydrophobic and to ensure chemical stability. All structures on the front and

back side of the membrane chip are defined using standard UV lithography and photo resist masking.

Using this general microfabrication strategy and the design toolbox based on the governing equations presented above, it is thus possible to construct any desired membrane chip configuration, within the design constraints presented in the beginning of this chapter.

Design iterations

The membrane chip presented in this thesis has undergone two main design iterations, as shown in Figure 4.2. As described above, the membrane is defined on the front side and all gas channels placed in-plane on the backside of the chip. In Figure 4.2a and c, the gas channels are on shown for each chip, with the individual sections highlighted by the color coding introduced in Figure 4.1. All through-holes, going either through the Pyrex glass, or through the handle wafer connecting to the sampling volume inside the chip, are depicted in black. The micro capillary on each membrane chip is designed according to Equation 4.10 and only constitutes the very last section of the "red" channel depicted in the illustrations, with a wider channel extending the high pressure (atmospheric) region to the start of the micro capillary.

The porous membrane is identical for all membrane chips used throughout this PhD work, and are made of an array of $2.5\,\mu$m diameter pores equidistantly spread $10\,\mu$m apart in a honeycomb structure. $50\,\mu$m large spots, equidistantly spread across the membrane $150\,\mu$m apart, are kept free of pores in order to form support pillars. Both the pore pattern, support pillars and the inner sampling volume can be recognized in the SEM image in Figure 2.1b shown in chapter 2.

The first membrane chip, as seen in Figure 4.2a-b, was designed with a $5\,$mm diameter membrane, in order to match the size of the $5\,$mm diameter electrode in the stagnant thin-layer cell presented in chapter 2. The carrier gas was introduced at one "side" of the sampling volume, and exited on the other. It was designed with a $6 \times 4.5 \times 3000\,\mu$m micro capillary yielding a molecular flow of $\dot{N}_0^{\mathrm{chip}}(\mathrm{He}) = 1.0 \times 10^{15}$ molecules/s and a $\tau_{\mathrm{res}} = 1.4\,$s. The rest of the gas system was designed accordingly to satisfy the design constraints. This first design iteration was designed as a proof-of-concept and used for testing various electrochemistry cell designs whereas the second iteration was designed specifically for the stagnant thin-layer cell presented in chapter 2.

In the second iteration of the membrane chip, as seen in Figure 4.2c-d the membrane size was increased to $7\,$mm in diameter, in order to ensure a $100\,\%$ membrane collection efficiency by capturing analytes which diffused radially from $5\,$mm diameter electrode. Furthermore, the gas flow in the gas flow in the sampling volume was changed to a radial flow pattern with the capillary connection to the MS placed in the center, and three carrier gas inlet channels connected at the rim of the sampling volume. This was done to hinder back-diffusion of analytes up into the thin-layer cell, and thereby ensure a fast
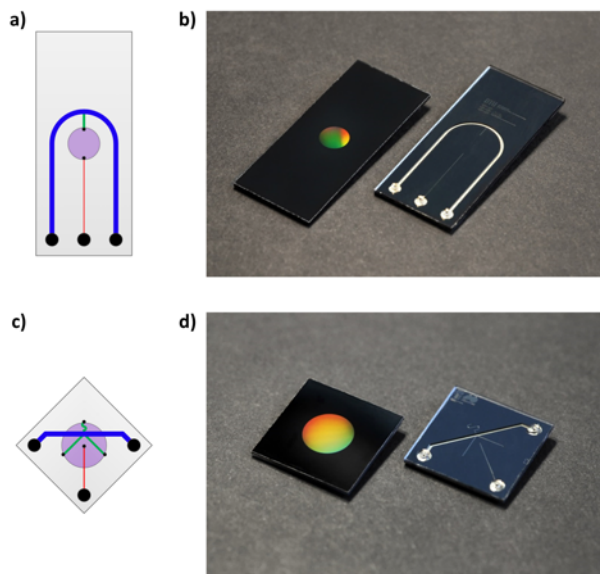
Figure 4.2: a) A 14.85 x 34.85 x 0.86 mm membrane chip with a
5 mm diameter membrane, designed to operate at 1 bar of chip pres-
sure with 2.5 μm diameter membrane pores and $\dot{N}_0^{\mathrm{chip}}(\mathrm{He}) = 1.0 \times$
10^{15} molecules/s, with a carrier gas flow from one side to the other,
and a residence time of $\tau_{\mathrm{res}} = 1.4\,\mathrm{s}$. The form factor allows for
10 chips on a 100 mm SOI wafer. **b)** A 15.00 x 15.00 x 0.86 mm
membrane chip with a 7 mm diameter membrane, designed to operate
at 1 bar of chip pressure with 2.5 μm diameter membrane pores and
$\dot{N}_0^{\mathrm{chip}}(\mathrm{He}) = 1.6 \times 10^{15}$ molecules/s. The carrier gas flow pattern is
radial from the perimeter (three inlets) to center (one outlet), with a
residence time of $\tau_{\mathrm{res}} = 1.7\,\mathrm{s}$. This form factor allows for 24 chips on a
100 mm SOI wafer.

response time of the membrane chip. The three inlet channels are made with
identical length and cross sectional geometries (causing one to obtain an odd
twisted shape in the design), which ensures a uniform flow pattern in the sam-
pling volume, and they are all connected to the same point on the carrier gas
reservoir channel ensuring a uniform pressure distribution. The capillary on the
second membrane chip iteration was designed with a $6 \times 6 \times 1000\,\mu$m micro
capillary yielding a molecular flow of $\dot{N}_0^{\mathrm{chip}}(\mathrm{He}) = 1.6 \times 10^{15}$ molecules/s and a
$\tau_{\mathrm{res}} = 1.7\,\mathrm{s}$. Again the rest of the gas system was designed accordingly to satisfy
the design constraints.

4.2   Interfacing to UHV

The membrane chip is interfaced to the external carrier gas handling system and to UHV, as shown in Figure 2.3, by means of an interface module as the one depicted in Figure 4.3. This is designed as an interface flange made of SS 316L stainless steel, with a recess fitting the membrane chip as well as four Viton O-rings making a UHV compatible seal between the Si chip and the stainless steel. The tolerances between making UHV tight seals and breaking the chip are somewhat low, so machining needs to be precise. The full assembly of the stagnant thin–layer EC cell presented in chapter 2 and the membrane chip, with this interface module, can be seen in Figure A.3 as an exploded view 3D rendering.

The concept of this interface module is trivial, but important considerations however still needs to be made, as this module effectively acts as a continuation of the conceptual flow diagram shown in Figure 4.1. This means that in order to ensure a fast exchange of the carrier gas flow in the carrier gas reservoir channel on the chip, the bore holes connecting to these channels should have as small an internal volume as possible, and in order to ensure a proper ballistic motion of molecules exiting the capillary, the bore hole connecting to the MS should be as large as possible. Even-though these are trivial design considerations, found in most vacuum physics textbooks [81], they are often not considered, even in
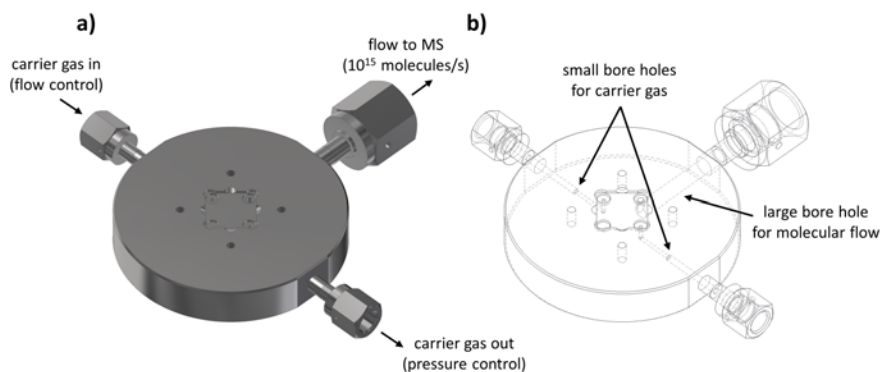

Figure 4.3: 3D rendering of the interface module used to interface the membrane chip to external gas handling and UHV. **a)** Shows a full 3D rendering of the module indicating the connection for the carrier gas flow and pressure control as well as the connection to the MS. **b)** shows a wire frame model of the module, revealing the inner bore channels connecting the gas lines. This interface module is made in a CF 40 flange format (70 mm in diameter), with a 1/8" female VCR fitting for both of the carrier gas connections and a 1/4" female VCR fitting to UHV.

commercial gas analysis systems.

Through design improvements of the interface module the response time for "sticky" compounds like EtOH (ethanol), from $\sim 30\,\mathrm{min}$ on an early iteration of the vacuum interface, to $2-3\,\mathrm{s}$, as illustrated in Figure 4.4. There a droplet of water containing $\sim 100\,\mathrm{ppm}$ EtOH is placed onto the membrane chip, while recording the MS response on $m/z = 31$. A similar experiment was conducted with $\sim 45\,\mathrm{ppm}$, which was detectable with a signal-to-noise ratio of ~ 1. This lower detection limit matches the anticipated lower detection limit predicted by the mass transport model presented in chapter 3. It should however be noted, that this measurement corresponds to the "infinite" reservoir case, described in chapter 3, which is why this response time does not directly compare to the anticipated response time in the case where a minute production of EtOH would be created on the surface of an electrode. The absolute amount of EtOH molecules present in this experiment is simply much more than would be created in a single pulse in an electrochemical experiment.
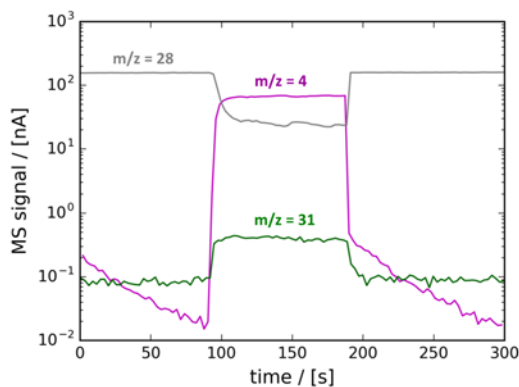

Figure 4.4: A droplet of water containing $\sim 100\,\mathrm{ppm}$ EtOH placed on the membrane chip. The measurement illustrates the lower detection limit and time response on the measurement of a "sticky" non-volatile analyte species, here represented by EtOH. The placement of the droplet is recognized by the onset of He presurization (see chapter 2). $m/z = 4$, 28 and 31, represent He, N_2 and EtOH, respectively. The response time is less than the mass spectrometer sample rate, which in this experiment was $\sim 2.8\,\mathrm{s}$.

4.3 Interfacing to electrochemistry

At the beginning of the present PhD work the focus was aimed towards developing a microreactor platform for analyzing chemical reactions in the liquid phase, inspired by the gas phase microreactor work done in the SurfCat group at DTU [77]. Thus the first interfacing of electrochemistry to the membrane chip, was done by an *electrode chip* as seen in Figure 4.5. Here metal electrodes were deposited onto a Pyrex chip, and a polymer photo resist was used to define a channel structure on top of the electrode pattern, in order to introduce electrolytes. This chip was then clamped onto a membrane chip, forming a hermetically sealed two-chip assembly. Initial electrochemistry experiments were performed in a two electrode configuration, and attempts were made on developing on-chip reference electrodes for various electrolytes. The liquid-phase microreactor poses many advantages in terms of having a closed assembly, free of atmospheric contaminants, and being potentially able to set and control potentials locally, by careful design of electrode patterns. The microreactor platform is however not a versatile platform in terms of sample choice. With further development, this system can prove highly useful in the future, but it has not been the main focus of the present PhD work.

As an alternative approach, focus was put into utilizing the membrane chip for probing electrochemical processes in bulk electochemistry setups, much inspired the OLEMS work introduced by Koper et al. [34] (see chapter 1). Work was therefore done in order to develop a "dip-stick" configuration of the membrane chip as seen in Figure 4.6, with the first iteration being an elongated membrane chip as seen in Figure 4.6a. In order to make the orientation of the actual membrane of the chip more versatile, a more advanced design was developed, where a small membrane chip was anodically bonded onto the polished end of a glass tube, containing inner gas channels for connecting to carrier gas flow and UHV. The assembly of such a system was demonstrated and thus
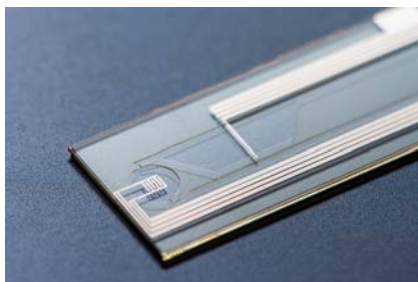

Figure 4.5: Photograph of an electrode chip with $200\,\text{nm}$ thin film Pt electrodes deposited onto a Pyrex chip, with a liquid channel system defined in a $\sim 100\,\mu\text{m}$ thick SU-8 polymer photo resist. The figure is from [P1].
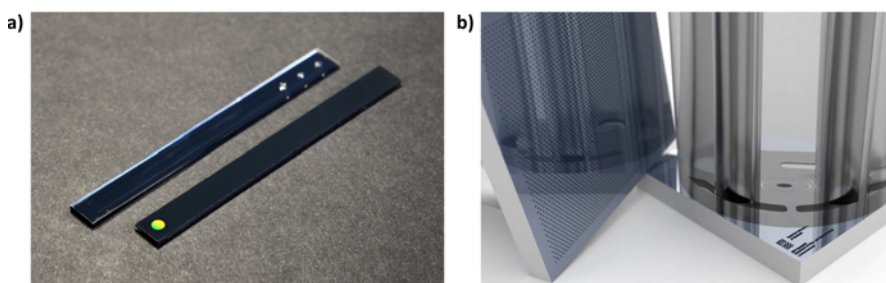
Figure 4.6: a) A 4.85 x 52.85 x 0.86 mm membrane chip with an 2 mm diameter membrane, designed to operate at 1 bar of chip pressure with 2.5 μm diameter membrane pores and $\dot{N}_0^{\text{chip}}(\text{He}) = 1.3 \times 10^{15}$ molecules/s, with a carrier gas flow from one side to the other, and a residence time of $\tau = 0.75$ s. This form factor allows for 14 chips on a 100 mm SOI wafer. **b)** Conceptual depiction of the final version of the dip-stick membrane chip.

proven possible, but never tried electrochemistry measurements. A 3D rendered concept illustration of this design can be seen in Figure 4.6b and the proof-of-concept system built can be seen in Figure A.5.

Preliminary experiments were performed using this dip-stick approach with Figure A.6 demonstrating an example of electrochemical CO_2 hydrogenation (see chapter 5 for an introduction to this field of research). It was however proven highly difficult to perform quantitative product detection, due to the ill-defined mass transport between the membrane chip and the electrode. Furthermore, with the liquid–vacuum interface being hydrophobic by design, in order not to flood the vacuum system with water, it is more prone to local sticking of gas bubbles. Furthermore, with only a part of the electrode being probed by the membrane, it is thus highly difficult to quantitatively correlate MS signals with any surface activity. As demonstrated by Koper et al. [34], the OLEMS technique does provide highly valuable insight into reaction mechanism through qualitative studies, but in this PhD work, further work with the dip-stick approach was discontinued. With further development, membrane chip dip-sticks could however introduce interesting possibilities of probing local electrochemical phenomena, especially with the added benifit of being able to dose reactant gases through the membrane chip system, as demonstrated in chapter 2.

Electrode on the membrane

As discussed in chapter 1 the "classic" DEMS techniques ensured 100 % membrane collection efficiency by depositing electrode material onto the membrane
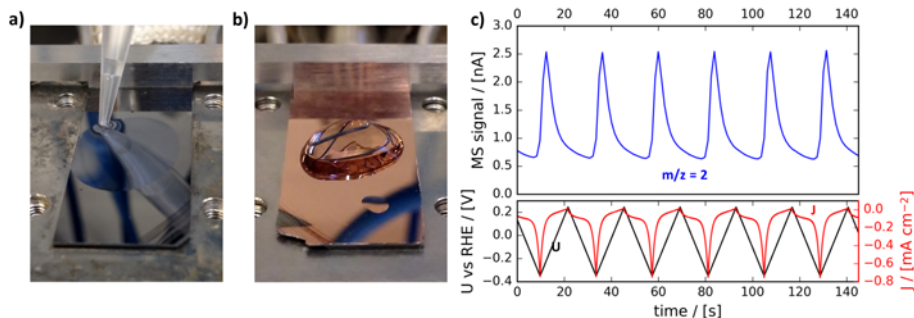
Figure 4.7: a) Chemical removal of FDTS coating from the top face of a membrane chip by exposure to 10 M KOH for a few minutes. After this treatment the membrane is wetted, as indicated by the water curvature at the tip of the pipette, while a suspended liquid–gas interface is maintained in the micro pores of the membrane. **b)** Membrane chip with 100 nm Cu thin film deposited onto the membrane, using physical vapor deposition. 2 nm Ti is used as an adhesion layer. **c)** "Classic" DEMS experiment performed with the membrane chip. HER is monitored during potential cycling between −0.35 and 0.25 V vs RHE with 50 mV/s in a 0.5 M potassium bicarbonate electrolyte (pH 12).

itself. This method also has the added benefit of having the electrode exposed to a bulk electrolyte bath, which makes it easier to utilize standard reference and counter electrodes, and prevents long term pH change given a larger electrolyte reservoir. It should therefore be highlighted that classical DEMS experiments with an electrode material deposited onto the membrane, were also tested on the membrane chip inlet system.

As the entire top face of the membrane chip is covered with FDTS it is somewhat difficult to adhere a metal. It is however possible to strip the topmost FDTS either chemically by a few minutes of exposure to 10 M KOH, or physically using vertically aligned Ar ion sputtering. If done properly the FDTS coating is preserved inside the micro pores of the membrane, while the top face becomes extremely hydrophilic, as seen in Figure 4.7a, where the membrane chip is wetted by a droplet of water, while suspending a liquid–gas interface across the micro pores.

Figure 4.7b shows a membrane chip covered with 100 nm Cu thin film deposited using *physical vapor deposition* (PVD) and in Figure 4.7c an electrochemistry experiment is conducted using a small "water tower" cell, inspired by the classical cell from Baltruscat et al. [29]. In Figure 4.7c the potential is cycled between −0.35 and 0.25 V vs RHE with 50 mV/s, demonstrating a fast time response on the detection of H_2 during HER.

The lessons learned from the above design iterations all led to the stagnant

thin–layer EC-MS system presented in chapter 2 of this thesis. Especially as the advantages of establishing a direct coupling between the MS and electro-chemistry through the membrane chip became apparent, the idea of capturing minute surface events during electrochemistry, as demonstrated in chapter 2, became highly intriguing. This, coupled with the desire for versatility in terms of sample choice, ultimately led to design of the stagnant thin–layer EC-MS system presented herein.

Transient CH$_4$ production on Cu

This chapter presents the discovery of a transient phenomenon during the electrochemical reduction of CO to hydrocarbons: By exposing a model system of Cu nanoparticles to oxygen, the catalytic mechanisms for CO electroreduction are briefly altered, making the catalyst more prone to CH$_4$ production. This phenomenon has a lifetime of only ~ 1 s, during which as few as $\sim 5 \times 10^{10}$ CH$_4$ molecules are generated, which makes the event difficult to detect without a sensitive real-time analysis tool like EC-MS.

The 5×10^{10} molecules/s observed in this study represent an even lower detection limit than the 30 nA HER limit discussed in chapter 2, due to the fact that CH$_4$ ($m/z = 15$) does not contain any physical background in the MS. Aside from giving insight to the mechanisms of CO electroreduction in itself, the following study thus provides a great example of what the membrane chip EC-MS presented in chapter 2 can be utilized for.

The nanoparticle synthesis and characterization presented herein, was done by Anders Bodin and Jakob E. Sørensen, and the EC-MS measurements was performed in collaboration with Søren B. Scott and Nicola Mazzanti. The following is an excerpt from [P3] which is under preparation for publication and attached to this thesis as a paper draft.

5.1 Electrochemical CO_2 reduction

When applying an electrical potential to an aqueous electrolyte, H_2O is split into H_2 and O_2 as demonstrated in chapter 2. However, when adding CO or CO_2 to the mix, i.e. when applying an electrical potential to a carbonated aqueous electrolyte, both C, H and O are simultaneously present as chemical building blocks, altering the chemistry drastically and making it possible to form reduced hydrocarbon products. This is referred to as the electrochemical CO_2 reduction reaction (CO2RR).

The first detailed study of CO2RR was presented by Hori et al. in 1985 [84], who demonstrated that several transition metal electrocatalysts form reduced carbon based reaction products, with Cu being particularly good at forming hydrocarbon reaction products. CO2RR on Cu was later mapped out in detail by Kuhl et al. [85] demonstrating 16 different reactions products for CO2RR on Cu alone, each with distinct reaction pathways involving various key reaction intermediates.

The goal of the CO2RR as a research field is to map out the catalytic dependencies of CO2RR in order to ultimately be able to tune selectivity for desired reaction species. To quantify overall faradaic efficiencies, methods like *gas chromotography* (GC), *liquid chromotography* (LC) or *nuclear magnetic resonance* (NMR), are often used to measure the average catalytic activity through the accumulation of products over a larger time period (15 minutes to a couple of hours). The faradaic efficiency of individual reaction products and intermediates is often low, and the catalysis highly time- and potential dependent. Much insight into reaction mechanisms can therefore be gained by using EC-MS to quantify time- and potential dependencies of reaction products and intermediates.

Today CO is well understood as being a key reaction intermediate for most hydrocarbon reaction pathways. Furthermore, the electrochemical reduction of CO_2 to CO alone is today a fairly optimized process, with a state-of-the-art catalyst like Au being capable of forming CO with $\sim 100\,\%$ selectivity, thereby suppressing HER almost entirely, at low overpotentials ($\sim 140\,$mV) [86]. It is thus useful to start from CO as a feed stock or chemical reactant, both in terms of research in order to understand further reduction steps better, and in terms of industrially applicable systems, which could be based on a two-step reaction process. The ultimate goal is however still to control a single direct pathway from CO_2 to a desired reduced carbon species.

A key result in the further reduction from CO was first preliminary demonstrated by Hori [87] and later mapped out and vastly improved by Kanan et al. [88], showing $\sim 43\,\%$ faradaic efficiency to pure EtOH (ethanol) alone, at modest overpotentials of $\sim 480\,$mV. This ignited the field of CO2RR even further, giving the hope that tuning of selectivities is in fact possible. The result was obtained on polycrystalline Cu sample, which was first thermally oxidized and then electrochemially reduced forming an oxide derived Cu (OD-Cu) ma-

terial. The mechanisms leading to such high selectivities on OD-Cu are still investigated and discussed in great detail [89–92]. With the latest studies investigating the direct influence of surface [93] or sub-surface [94, 95] oxygen. In the present study, the direct role of adsorbed surface oxygen, in isolation from the bulk, is investigated with EC-MS.

5.2   Sample preparation and characterization

The short-lived production CH_4 presented in this study was initially discovered on a sample containing small amounts of Cu impurities. Therefore, mass-selected Cu nanoparticles were used to establish a well-defined model system resembling low loading of Cu impurities, i.e. a catalyst system with large surface-area to volume ratio and a large fraction of under-coordinated sites.

The samples used in the present study were made by depositing (4.8 ± 0.2) nm mass-selected Cu nanoparticles onto a 5 mm diameter *glass carbon* (GC) disc electrode with a projected surface coverage of 5 % using a NanoBeam2011 nanoparticle source from Birmingham Instruments Inc. This corresponds to a total mass loading of 24 ng. The low loading was chosen to reduce particle-particle interaction and cross-talk phenomena caused by mass transport between particles.

The GC substrate was characterized using *X-ray photoelectron spectroscopy* (XPS) and *ion scattering spectroscopy* (ISS) both prior to and after deposition
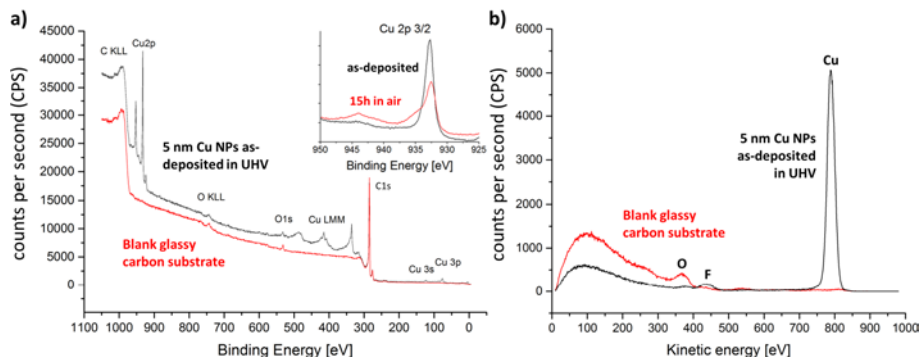

Figure 5.1: a) X-ray photoelectron spectroscopy (XPS) spectra of a glassy carbon (GC) substrate before and after deposition of Cu nanoparticles. A narrow scan of the Cu $2p_{3/2}$ peak (inset) shows the effect of exposing the sample to air for 15 hours, resulting in a chemical shift of the Cu $2p_{3/2}$ peak, indicating the formation Cu_2O. **b)** Ion scattering spectroscopy (ISS) spectra of glass carbon substrate before and after deposition of Cu nanoparticles, confirming a clean substrate prior to and a clear Cu signal after deposition.
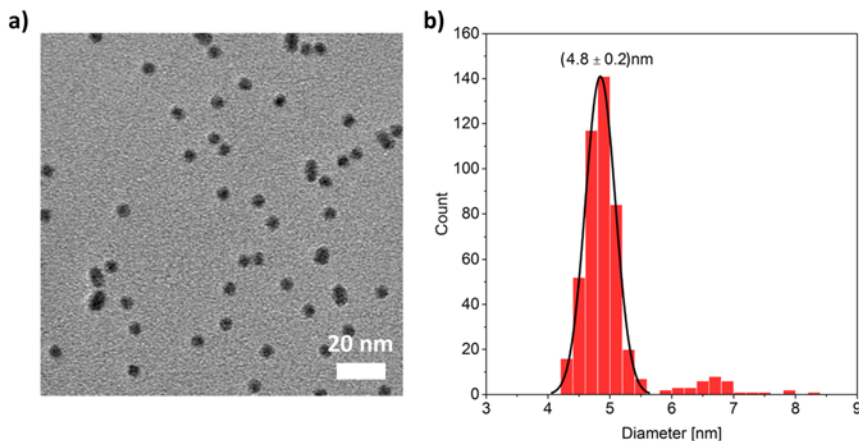
Figure 5.2: a) Transmission electron micrograph (TEM) image of Cu nanoparticles deposited with a mass of 350,000 amu onto a lacay carbon TEM grid with a projected surface coverage of 5 %. **b)** Histogram showing the size distribution of the average diameter gathered from the analysis of TEM images as the one shown in **a)**.

of nanoparticles. XPS and ISS are both very surface sensitive characterization techniques capable of verifying the chemical composition of the very surface of the sample, i.e. where catalysis occurs, with ISS probing the top-most surface layer. The XPS spectra in Figure 5.1a show a clean sample containing nothing but Cu, O and C. As samples were exposed to air during transfer from the UHV chamber to the EC-MS setup, an extra scan was obtained after 15 hours of air exposure, showing no other change than the formation of CuO_2, as indicated by the chemical shift of the Cu 2p 3/2 peak, as shown in the narrow scan in the inset of Figure 5.1. The ISS spectrum confirms a clean carbon substrate prior to and a clear Cu peak after deposition. Only minor impurities of oxygen and fluorine are present prior to deposition, with the latter presumably coming from a PTFE holder used during mechanical polishing of the GC substrate prior to deposition. The narrow size distribution of the mass-selected nanoparticles was verified by *transmission electron microscopy* (TEM) through micrograph images as shown in Figure 5.2a, from which a histogram of the average particle diameters was generated as shown in Figure 5.2b.

Prior to deposition all glassy carbon substrates were thoroughly cleaned using the following procedure: 1) Rinsing in ultrapure water 2) Cleaning in 65 % SupraPure nitric acid for one hour, then rinsing in ultrapure water 3) Polishing with $1/4\,\mu$m diamond paste 4) Sonicating two times for 10 minutes, first in ethanol and then in ultrapure water 5) Repeating the acid treatment (step 2) and 6) Sonicating two times in ultrapure water for 10 minutes.

After cleaning some substrates still showed trace amounts of transition metal impurities in ISS, which however is expected due to the extreme sensitivity of that technique.

5.3 Experimental procedure

All samples were introduced to the EC-MS immediately after deposition, being under electrochemical potential control within 60 minutes after air exposure, after which the sample was carefully monitored by EC-MS. All EC-MS experiments were conducted in a 0.5 M potassium bicarbonate buffer titrated to pH 12 with KOH. In Figure 5.3 the first part of an experiment series, prior to the onset of CO electroreduction experiments, is plotted with $t = 0\,s$ being the exact time where the sample is taken out of vacuum. In Figure 5.3a electrolyte is introduced around $t = 900\,s$, indicated by He pressurization of the membrane chip (see chapter 2 for details), after which Cu nanoparticles are reduced, from the CuO_2 state obtained during air exposure, for 30 minutes at a constant current of $-10\,\mu A$. This reduction is monitored through the gradual increase in HER and the nanoparticles are assumed to be fully metallic once steady-state HER is reached.

The potential is then cycled between -0.8 and $0.2\,V\,vs\,RHE$ at $20\,mV/s$ to see if the system is stable and to verify that no unexpected redox features are present in the Cu CV. These CVs are mostly dominated by the glassy carbon substrate. During cycling, CO is introduced in the carrier gas stream, as described in chapter 2 and shown in Figure 5.3b, with the cycle immediately prior to and after CO exposure plotted in Figure 5.3c and d, respectively. As Cu is a better HER catalyst than the glassy carbon substrate, is HER predominantly conducted by Cu at low overpotentials in a He saturated electrolyte. Upon CO exposure HER is however significantly suppressed due to CO poisoning and CO reduction to CH_4 ($m/z = 15$) and C_2H_4 ($m/z = 26$) sets in. Interestingly, CO poisoning does not occur on large polycrystalline Cu samples, indicating a much higher fraction of stronger binding under-coordinated sites on these nanoparticle samples, as would be expected.

The following EC-MS results are quantified through an internal calibration of H_2 and O_2 and an external calibration of hydrocarbon reaction products, through normalization against relative sensitivity factors (RSF) [68, 70], as described in chapter 2. The latter is considered precise within a factor of ~ 2, which was verified for CH_4 through a membrane chip gas calibration.

5.4 Important note on a systematic error

Upon exposure to the electrolyte a brief overshoot in the open circuit potential was found to cause a significant corrosion of the Cu nanoparticle sample prior
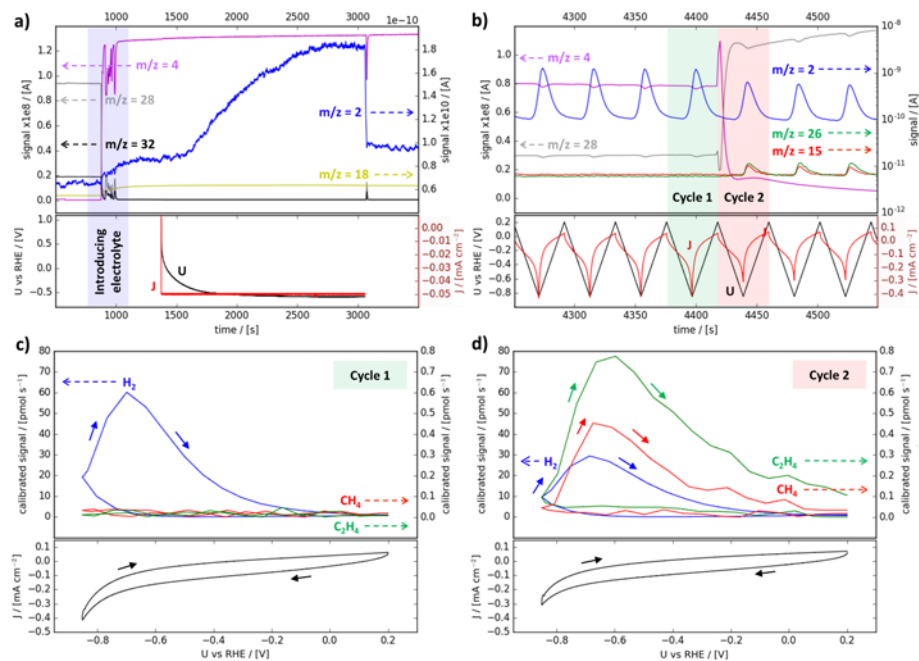
Figure 5.3: a-b) EC-MS plots illustrating the initial experimental steps between taking a sample out of vacuum at $t = 0$ s until the onset of CO electroreduction experiments at $t \approx 4400$ s. **a)** Sample mount and introduction of electrolyte after ~ 15 min (~ 900s) of air exposure. The sample is reduced at a constant current of $-10\,\mu A$ for 30 minutes until a steady-state HER production is obtained (seen in the $^{m}/_{z} = 2$ MS signal). **b)** Abrupt introduction of CO reactant gas by changing the carrier gas feed to the membrane chip (at $t \approx 4400$) from He ($^{m}/_{z} = 4$) to CO ($^{m}/_{z} = 28$). Here it is done while cycling the potential between -0.8 and 0.2 V vs RHE with a scan rate of 20 mV/s, with carrier gas change made exactly between two consecutive cycles plotted in a calibrated EC-MS plot vs potential in **c** and **d**. Calibration of H_2, CH_4 and C_2H_4, measured at $^{m}/_{z} = 2$, 15 and 26, respectively, is here done according to the procedure described in chapter 2. Prior to introduction of CO the sample is active for HER as seen in **c**, while the introduction of CO causes immediate CO poisoning with CH_4 and C_2H_4 starting to be produced.

to each experiment. This systematic error was discovered while drafting the appended manuscript [P3] and thus more work is needed to correct the error before submission of the manuscript. The error was systematic in the sense that many samples had similar overall CO reduction activities, with a few outliers acting more like blank glassy carbon. The present study is based on four samples
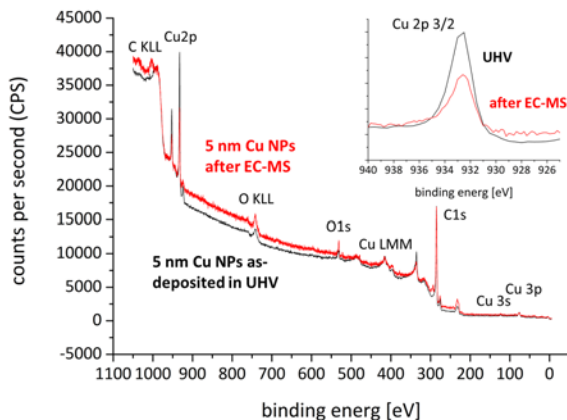
Figure 5.4: X-ray photoelectron spectroscopy (XPS) specta of a Cu nanoparticle sample before and after EC-MS experiments. The narrow scan of the Cu $2p_{3/2}$ (inset) shows large amounts of Cu after introducing the sample under potential control. The post EC-MS spectrum is taken after 5 minutes of Ar ion sputtering which was done in order to clean residue potassium from the surface. The loss of Cu is assumed to be primarily caused by the Ar ion sputtering, but these data are however still preliminary.

from this systematic grouping.

The few outliers formed a basis of suspicion leading to the development of the following well-defined procedure for mounting delicate samples under full potential control: An external three electrode setup containing a "dummy WE" is first connected to the inlet via a T-piece and a glass frit (see chapter 2 for a recap of the setup configuration). The sample WE is then short circuited to the dummy WE through a hardwired connection with similar (same or higher) ohmic resistance as the ohmic drop through the glass frit connection on the inlet, a resistance which is then compensated for by the potentiostat. This ensures that a fixed potential is set on the sample WE as soon as it is exposed to the electrolyte meniscus during filling of the EC cell. Once the cell is filled, the sample WE is brought to open circuit potential and briefly detached from the dummy WE, while moving the external CE and RE to the cell. The open circuit potential is recorded both before and after the temporary disconnect and is assumed to be stable in between these two recordings.

In Figure 5.4 two XPS spectra for as-deposited and post EC-MS are co-plotted for a sample mounted under potential control, illustrating that the above procedure works as expected. Comparing the general CO reduction activity of this sample, with the samples used in the following study, reveals that $\sim 90\%$ Cu was lost due to corrosion, with only $\sim 2.4\,\mathrm{ng}$ left. This is in itself a positive

result in terms of instrumental sensitivity, but invalidates the claim of having a well defined model system, without the proposed mounting procedure.

This systemic error does however not alter the qualitative observations in the following. The transient phenomena observed in this study have been observed on samples ranging from small Cu impurities to large loadings of nanoparticles, being only more pronounced in the former. The phenomenon is assumed to have more to do with high densities of under-coordinated catalytic sites than with the specific nanoparticle sample. Experiments are currently being redone before final submission of the study with only minor changes made to the attached paper draft.

5.5   Experimental results

In Figure 5.5a an EC-MS plot demonstrates the key result of this study: by exposing Cu nanoparticles to gaseous dioxygen (O_2), while resting the working electrode at $0.0\,V$ vs RHE, a high transient production of CH_4 is seen at the onset of constant-potential CO electoreduction. Interestingly, this transient behavior is not observed on H_2 or C_2H_4, which indicates that only the reaction pathway towards single–carbon reaction products is affected. Here, dioxygen is introduced by flushing the working volume for $5\,s$ with aerated electrolyte, resulting in a sharp O_2 pulse seen by both the MS as a rise in the O_2 signal and the by the electrode indicated by an oxygen reduction current measured in the electric current signal. The working electrode potential is stepped from 0.9 to $-0.8\,V$ vs RHE for five minutes while monitoring reaction product with the MS. The electric current signal is strongly dominated by double-layer capacitance from the GC substrate at the onset of the constant-potential experiment.

In order to quantify the potential dependence of the transient phenomenon, the experiment in Figure 5.5a was conducted at multiple potentials, as seen in Figure 5.5b, starting at $-0.6\,V$ vs RHE, just before hydrocarbon products are detectable in this system. The integrated MS signal for each reaction product, from consecutive one minute constant-potential step experiments, is plotted against working electrode potential. The samples were exposed to $5\,s$ of aerated electrolyte prior to each experiment, while resting the potential at $0.0\,V$ vs RHE. The transient CH_4 production is separated from the steady-state CH_4 by defining the last half of the signal as steady-state and integrating as indicated in the inset in Figure 5.5b. The error bars in the figure represent mean and standard deviation between measurements on four separate samples. A control experiment on a blank glassy carbon substrate is inserted with semi-transparent data points, showing minute levels of hydrocarbon formation. This is attributed to the trace impurities, as also reported previously in literature [96].

From Figure 5.5b it is clear, that the steady-state and transient components of CH_4 have different potential dependencies, with a Tafel slope of 91 mV/decade and 151 mV/decade, respectively, indicating different reaction mech-
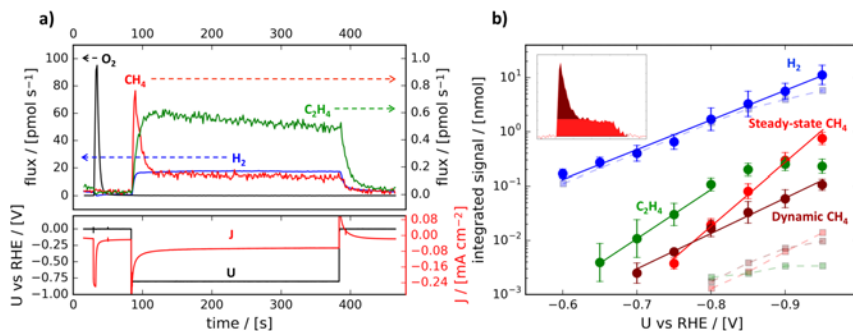
Figure 5.5: a) EC-MS plot demonstrating transient production of CH_4 after exposing a Cu nanoparticle sample to gaseous O_2 immediately prior to a constant-potential CO electroreduction experiment performed at $-0.8\,V\,vs\,RHE$. Note that only the production of CH_4 is affected, with H_2 and C_2H_4 remaining largely unchanged. H_2, O_2, CH_4 and C_2H_4 are measured on $m/z =2$, 32, 15 and 26, respectively, and calibrated according to the procedure described in chapter 2.) **b)** Tafel plot of the integrated production of CO reduction products after consecutive 1 min experiments at different potentials. Steady-state and transient CH_4 signals are integrated individually as illustrated in the figure inset. Data points and error bars represent the mean and standard deviation, respectively, of measurements on four separate samples.

anisms. C_2H_4 has a Tafel slope of 122 mV/decade at more cathodic potentials and then tapers of towards more cathodic potentials, due to C-C coupling being gradualy prevented by the increased rate of C1 product formation (CH_4). This trend, and the recorded Tafel slopes for steady-state CH_4 and C_2H_4 production, are in good agreement with previous studies on polycrystalline Cu reported in literature [85, 87].

Effect of oxygen on transient CH_4 production

To verify that dioxygen is truly causing this transient behavior, an experiment was conducted where a two minute pulse of gaseous O_2 was dosed into the carrier gas stream, as demonstrated during the CO stripping experiment in chapter 2. As a control, the same experiment was conducted with Ar pulse injection prior to the introduction of O_2, as seen in Figure 5.6. This shows, that when exposing the sample to Ar at a resting potential of $0.0\,V\,vs\,RHE$, no transient CH_4 production follows, while exposure to O_2 under the same conditions activates the transient.

To map out the conditions necessary to activate the transient CH_4 production, the experiment shown in Figure 5.5a was conducted with the CO reduction potential kept at $-0.85\,V\,vs\,RHE$ for one minute for each consecutive experi-
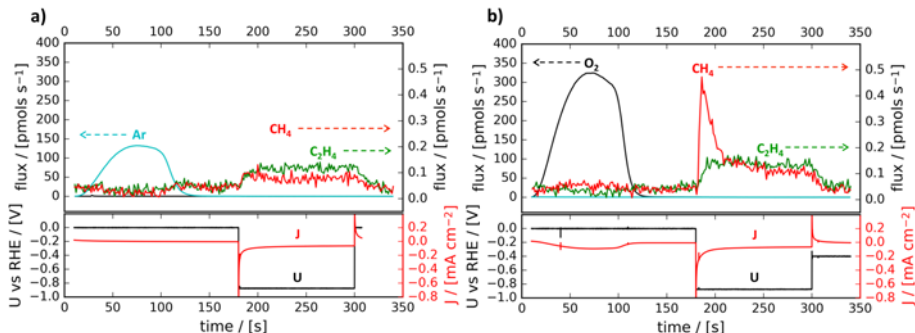
Figure 5.6: The effect of oxygen demonstrated by two consecutive constant-potential CO electroreduction experiments performed at $-0.9\,V\,vs\,RHE$. Gaseous Ar (**a**) and O_2 (**b**) is injected as $\sim 90\,s$ pulse injections into the carrier gas stream of the membrane chip, while holding the potential at $0.0\,V\,vs\,RHE$. This demonstrates that only gaseous O_2 is able to activate the transient production of CH_4.

ment, while varying the resting potential during which dioxygen is introduced, as shown in Figure 5.7. The introduction of O_2 is here again done in a repetitive manner by a $5\,s$ flush of aerated electrolyte prior to each constant-potential experiment. Similar to Figure 5.5b the transient and steady-state components of the CH_4 production are considered individually through separate peak integration as discussed above.

This experiment demonstrates that the transient CH_4 production is only activated when dioxygen is introduced at potentials anodic of $-0.20\,V\,vs\,RHE$, after which the amount of transient CH_4 steadily increases with more anodic resting potentials. A plateau is reached at potentials around $+0.20\,V\,vs\,RHE$, seemingly due to the catalyst getting somehow saturated with oxygen. Similar experiments were conducted, keeping the resting potential fixed and instead changing the duration of oxygen exposure, showing the same trend and thereby supporting this oxygen saturation hypothesis.

Interestingly, for resting potentials anodic of $0.0\,V\,vs\,RHE$, the steady-state production of CH_4 and C_2H_4 starts increasing, without affecting the transient. This indicates, that a higher degree of oxidation activates the general CO reduction activity, which is consistent with observations on oxide-derived Cu surfaces [86, 88].

Necessity of potential stepping

This entire study further exemplifies the importance of keeping the input parameter, i.e. the electric potential, constant in time when analyzing an electrochemical system exhibiting a strong time-dependent behavior, as discussed
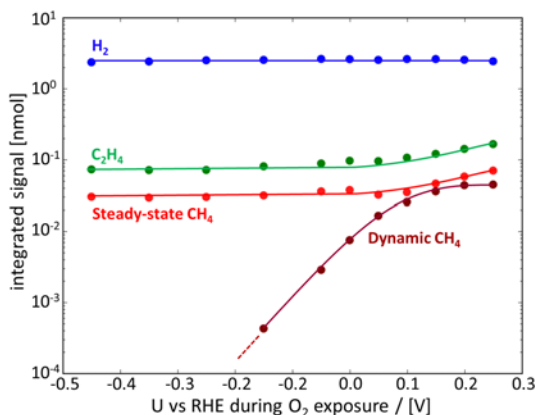
Figure 5.7: Integrated signal from CO electroreduction product formation as a function of the resting potential during which dioxygen is introduced. Each data point represents a 1 min constant-potential experiment at $-0.85\,\mathrm{V}$ vs RHE with dioxygen introduced by a $5\,\mathrm{s}$ flush of aerated electrolyte prior to each experiment.

in chapter 2. Historically, many DEMS studies have focused on mapping out potential dependencies, with previous EC-MS studies of CO electroreduction being no exception [97–99]. Figure 5.8a-b shows a linear sweep voltamogram with a scan rate of $5\,\mathrm{mV/s}$ plotted against time (a) and potential (b), on the present nanoparticle system in the presence of CO. The transient CH_4 production might have been visible as a shoulder on the CH_4 signal during the cathodic potential sweep, but as this catalyst has proven to be particularly sensitive to the oxidation state of the surface, the oxygen is simply reduced off before the relevant CH_4 formation potentials are reached, hence no shoulder is observed.

Figure 5.8c-d shows an experiment demonstrating the activation and deactivation of the transient CH_4 by oxygen exposure. Experiment A (circular data points) is similar to the experiment shown in Figure 5.7 and in experiment B a gradually increasing intermediate potential is set after a $5\,\mathrm{s}$ dioxygen exposure at a resting potential of $0.0\,\mathrm{V}$ vs RHE. This demonstrates first of all a different activation and deactivation potential, and secondly it shows that the oxygen activation, and thus the transient phenomenon disappears at potentials cathodic of $-0.5\,\mathrm{V}$ vs RHE, which is before the onset of both steady-state and transient CH_4 production according to both Figure 5.8a-b and Figure 5.5b.
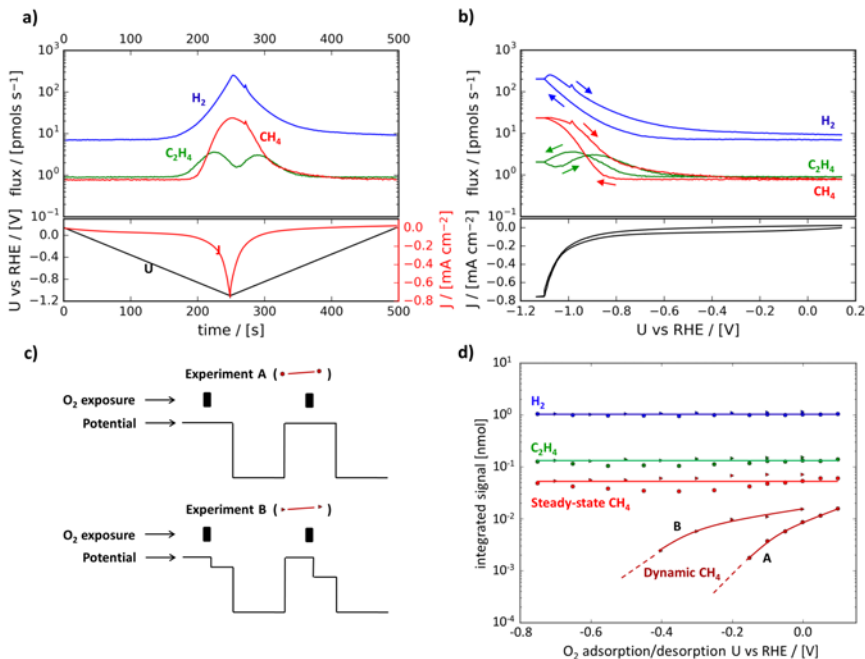
Figure 5.8: a-b) EC-MS plot showing a potential scan between 0.2 and $-1.1\,\text{V}$ vs RHE performed with $5\,\text{mV/s}$. **c)** Schematic of the experimental procedure for probing the oxygen adsorption and desorption potentials, respectively. In experiment A, the resting potential during O_2 exposure is gradually varied between a series of constant-potential experiments at $-0.85\,\text{V}$ vs RHE. In experiment B oxygen is introduced at $0.0\,\text{V}$ vs RHE for each experiment, whereas an intermediate desorption potential is instead gradually varied. **d)** Integrated signal from each CO electroreaction experiment from the A and B experimental procedures, respectively.

5.6 Computational modeling

In order to provide an explanation for the transient activation of CH_4 production by exposure to dioxygen, a computational model based on *density function theory* (DFT) was established by Alexander Bagger, a PhD student from the Rossmeisl theory group at the University of Copenhagen. Details on the computational model can be found the "Methods Summary" in [P3].

Figure 5.9a shows a Wulff construction of a Cu nanoparticle containing 5900 Cu atoms, corresponding to an average particle diameter of $\sim 5\,\text{nm}$ ($\sim 375,000\,\text{amu}$), representing an ideal version of the nanoparticle catalyst studied experimentally. Each surface atom is color-coded according to its *coordina-*
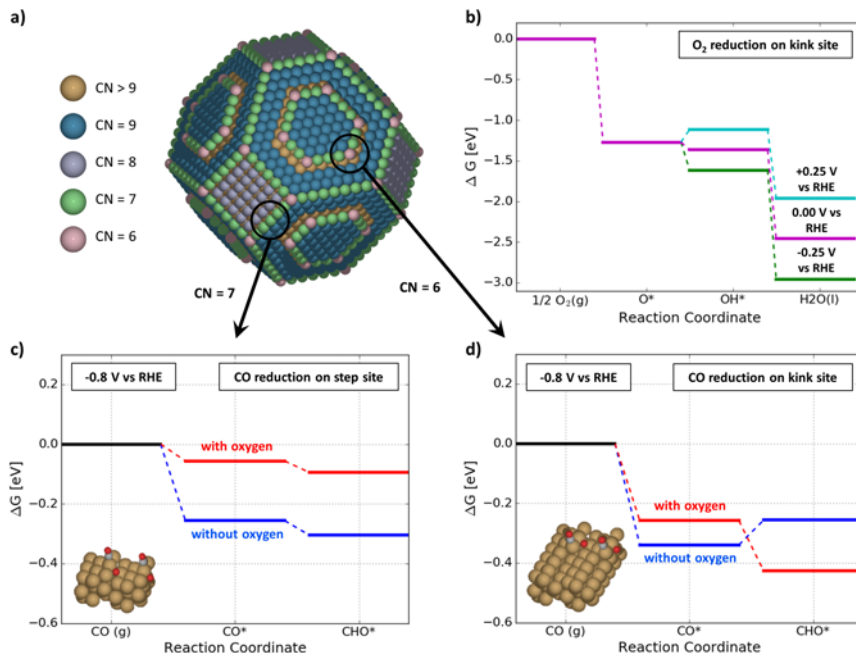
Figure 5.9: **a)** Wulff construction of a Cu nanoparticle containing 5900 Cu atoms, corresponding to a particle size of $\sim 5\,nm$, used for experiment in the present study. The surface atoms are color-coded according to their coordination number (CN). **b)** Free energy diagram of the reduction of $O_2(g)$ to $H_2O(l)$ on a kink site, plotted for three different applied potentials, illustrating the stability of *O at potentials anodic of $\sim 0.0\,V\,vs\,RHE$. **c-d)** Free energy diagrams of the first two rate-limiting steps for electroreduction of CO to CH_4 on step (**c**) and kink (**d**) sites, respectively, with (red) and without (blue) a surface adsorbed oxygen adjacent to the catalytic site.

tion number (CN) depicting the number of nearest neighbor atoms in the lattice.

Several previous DFT studies have been conducted on CO_2 and CO electroreduction investigating the rate-limiting steps on the reaction pathway towards CH_4 on different Cu surfaces [100]. Flat terrace sites (CN = 8 or 9) are thus known to be limited by the adsorption of CO onto the surface, given small binding energies for *CO ($< 0.1\,eV$). These sites are therefore not expected to contribute significantly to the formation of CH_4. On more under-coordinated sites, which bind CO strong enough to get the reaction started, the rate-limiting reaction step is however considered to be the first proton-electron transfer to *CO forming *CHO, which is potential-limited. All subsequent reaction steps towards CH_4 after *CHO, are down-hill in energy.

CO binds stronger to the surface than CHO on under-coordinated sites (CN = 6 or 7), as it forms a double-bond to the surface whereas CHO only forms a single-bond. This effect is more pronounced on highly under-coordinated kink sites (CN = 6) compared to step sites (CN = 7), causing kink sites to have a higher limiting potential for overcoming the strong binding of CO. This implies that the majority of CH$_4$ production should occur in step sites (CN = 7). This trend is reproduced using this DFT model, as shown in the free energy diagrams in Figure 5.9c-d indicated by the blue traces (marked 'without oxygen') for step and kink sites, respectively. Here an electrical potential of -0.8 V vs RHE has been applied to the computational results as an adjustment to the reference state of hydrogen, i.e. by the *computational hydrogen electrode* (CHE).

Using the same DFT model it is now possible to investigate the effect of adsorbing oxygen (*O) onto an adjacent sites with respect to a *CO or *CHO. The respective *O sites chosen for this model are the ones less prone to reducing *O further to H$_2$O(l). i.e. by the stability of *O with respect to *OH, as shown in free energy diagram in Figure 5.9b for the kink site and as indicated in the inset figures in Figure 5.9c-d, respectively. With oxygen adsorbed to the surface, the DFT model show that *O weakens the binding for *CO on both kink and step sites, whereas *CHO is stabilized on step sites and destabilized on kink sites. Thereby the kinks sites, which were previously inaccessible to CH$_4$ production, gets activated, as shown in the red lines (marked 'with oxygen') in Figure 5.9c-d.

The fact that *CHO is stabilized by an adjacent *O on kink sites, but destabilized on step sites, is due to a geometric effect, causing *CHO to tilt in order to orient itself favorably with respect to *O. CO forms a stronger double-bond to the surface it is therefore less capable of tilting. This is a general trend which is observed irrespective to the precise position of *O.

Life-time of the transient

The transient nature of the activated additional pathway towards CH$_4$ production is due to the fact that *O reduces quickly to H$_2$O(l) at CO electroreduction potentials, as shown in Figure 5.9b for the kink site. At potentials anodic of $+0.25$ V vs RHE, *O is thermodynamically stable on kink sites, with further reduction to *OH becoming favorable around 0.0 V vs RHE. These calculations does however not include kinetic barriers between reaction intermediates, so in the presence of any kinetic barrier from *O to *OH, it is likely that *O can exist in a meta-stable configuration below 0.0 V vs RHE, as indicated by the above EC-MS experiments.

The life-time of the transient phenomenon is estimated to be of the order 1 second at -0.85 V vs RHE, by utilizing the EC-MS mass transport model presented in chapter 3. Figure 5.10 shows the predicted peak shape of the transient CH$_4$ MS signal, with the total amount of measured CH$_4$ being released from the electrode on different time scales. The anticipated peak shape given a 1 s pulse
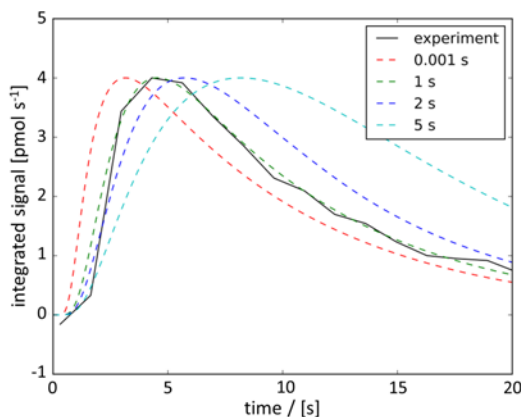
Figure 5.10: Comparison between the experimental and anticipated transient CH_4 peak shapes assuming various life-times of the transient phenomenon. The anticipated peak shapes are generated using the mass transport model introduced in chapter 3.

duration seems to match the experiment very accurately. The tail of the steady-state CH_4 production is used as an internal verification of the transport model, through the matching of the anticipated and measured time-constants. During this life-time a single active site turns over 2-20 CH_4 molecules, given a potential of $-0.95\,V$ vs RHE. This turn-over number is estimated by matching the total amount of transient CH_4 generated at $-0.95\,V$ vs RHE (from Figure 5.5b, with the average total number of surface atoms (~ 1300) and kink sites (~ 70) obtained from generating 8 different Wulff constructions of nanoparticles with a mass of $\sim 350,000\,amu$, representing a lower and upper estimate, respectively. It is furthermore estimated under the assumption of having a full loading of the $\sim 24\,ng$ of Cu nanoparticles. In the light of the sample corrosion discussed earlier in this chapter, this is more likely to be of the order 20-200 CH_4 molecules per second per site on the present samples. A turn-over number > 1 indicates that the phenomenon is in fact catalytic and not just an artifact of a chemical reaction forming CH_4 by consuming surface adsorbed oxygen in the process.

In summary, this DFT model suggests that the under-coordinated kink sites on Cu, which otherwise bind CO too strongly, get activated towards CH_4 production in the presence of a nearby surface adsorbed oxygen atom, which is reduced away after a few CH_4 turn-overs at CO electroreduction potentials. The activation is due to the highly electronegative oxygen atom stabilizing the *CO reaction intermediate while destabilizing *CHO due to a geometric effect. The latter is in itself an interesting aspect of the model, as CO and CHO binding energies normally scale with each other [101, 102]. The mere fact that a change

made to a catalytic surface affects one reaction intermediate differently than the other, here by a simple geometric effect, potentially opens up for a whole new aspect of tuning reaction mechanisms [103]. The dream of altering the behavior of individual reaction intermediates, in order to thereby be able to tune reaction pathways directly, is a central topic in modern catalysis [104].

5.7   Concluding remarks

Previous studies have shown that an oxidative pre-treatment of Cu increases CO-electroreduction activity [88], and surface oxides [93] and sub-surface oxygen [95] have been proposed to promote C-C coupling and thus the formation of C2 hydrocarbon products (C_2H_4). The latter stands in contrast with the present study, where C1 product formation (CH_4) is increased with C2 product formation remaining unaffected. This study however confirms the current understanding that C1 and C2 products are formed with distinct mechanisms and with different limiting potentials as shown in Figure 5.5b [105,106].

The main difference between the present and other studies, is the high sensitivity enabled by the membrane chip EC-MS system, in combination with a well–defined control of the dissolved gas environment seen by the electrode, as well as the constant–potential approach allowing the EC-MS to monitor the dynamic change of the catalytic system as a function of time. The added sensitivity, currently only achievable using the membrane chip EC-MS system, makes it possible to isolate the effect of surface oxygen, from further oxidation of the sample, and analyze minute changes in catalytic activity on a fast time-scale.

CHAPTER 6

Anodic H$_2$ desorption on Cu

This chapter presents a preliminary study on polycrystalline Cu demonstrating electrochemical desorption of gaseous H$_2$ at potentials anodic of the reversible hydrogen potental (RHE). The chapter will present what is currently known about the phenomenon, which is seemingly novel, and will discuss possible explanations for the observations, as well as proposed ideas for future studies. As with the transient CH$_4$ study presented in chapter 5, this study likewise provides an elegant demonstration of the capabilities of the membrane chip EC-MS system presented in this thesis.

EC-MS measurements in the following have been conduction in collaboration with Søren B. Scott and Nikolaj R. Knøsgaard. At the time of writing Søren B. Scott is working on calculating ad- and desorption energies for the electrochemical system presented herein, using density functional theory (DFT), in order to explain the present phenomenon. This will, together with the data presented in the following, constitute [P4].

The following study couples directly to the work on electrochemical CO$_2$ reduction presented in chapter 5, as adsorbed hydrogen species potentially play a vital role as reactants in the formation of hydrocarbon species through electrochemical CO$_2$ hydrogenation [107]. However, as discussed in chapter 5, the exact mechanisms are still being debated [85]. Furthermore, with hydrogen evolution being a competing reaction to the CO$_2$ reduction reaction pathways, it is highly valuable to gain insight into the mechanisms of ad- and desorption of hydrogen species on Cu.

6.1 Sample preparation

All measurements presented in the following have been conducted on a 5 mm Cu disc electrode, using the EC-MS setup presented in chapter 2. The electrode was mechanically polished with 1/4 μm diamond paste prior to experiments. Experiments were conducted in either 0.1 M KOH at pH 13, or in a 1.0 M bicarbonate buffer titrated to either pH 7.8, 9, 10.5 or 12 with 1.0 M KOH. As low faradaic currents are experienced in these experiments, the pH in the working volume of the stagnant thin–layer cell is assumed stable, and no apparent changes were observed, even across longer experiment sessions. The pH of a given experiment will be indicated in the figures below.

6.2 Demonstrating anodic H$_2$ desorption

When cycling the electrical potential of a Cu electrode between -0.3 to 0.45 V vs RHE a surprising double feature appears in the H$_2$ formation on the electrode, as seen in Figure 6.1a, where the calibrated H$_2$ signal recorded with the MS is plotted together with electric current and potential in an EC-MS plot as a function of time. At cathodic potential H$_2$ evolves as expected due to HER, while scanning to potentials anodic of the reversible hydrogen potential, triggers a second desorption of gaseous H$_2$. This is surprising as reduction of water to H$_2$ is thermodynamically prohibited at these potentials. Integration of the second desorption feature yields ~ 50 pmol of hydrogen, which corresponds to $\sim 10\%$ of a monolayer, assuming a flat Cu surface with an average surface site density corresponding to Cu(100). The anodic desorption phenomenon is only seen if the potential is scanned cathodic to the (near) HER region prior to the anodic sweep, indicating that a surface hydrogen reservoir is being filled at sufficiently cathodic potentials and then emptied again at more anodic potentials.

Increasing the anodic potential limit to 0.45, 0.60 and 0.85 V vs RHE, respectively, as shown in Figure 6.1b, reveals that the anodic desorption phenomenon happens regardless of whether the anodic sweep passes through the typical Cu redox features or not, and is therefore not coupled to the oxydation or reduction of the Cu electrode. By varying the potential scan rate, as seen in Figure 6.1c, it is seen, that the integrated anodic H$_2$ desorption signal remain unaffected, still yielding ~ 50 pmol of desorping H$_2$, while the rate of desorption decreases with gradually lower scan rates, indicating that the desorption phenomenon is triggered by the potential and not merely a time delay.

To confirm that this phenomenon is in fact electrochemically triggered, an experiment was performed where the anodic H$_2$ desorption feature was isolated by resting the electrode at an intermediate potential of -0.05 V vs RHE for 60 s and 120 s, respectively, in between evolving H$_2$ by HER at cathodic potentials and anodic desorption of H$_2$, activated by sweeping the potential anodic to 0.45 V vs RHE with 50 mV/s. As shown in Figure 6.1d this again demonstrates
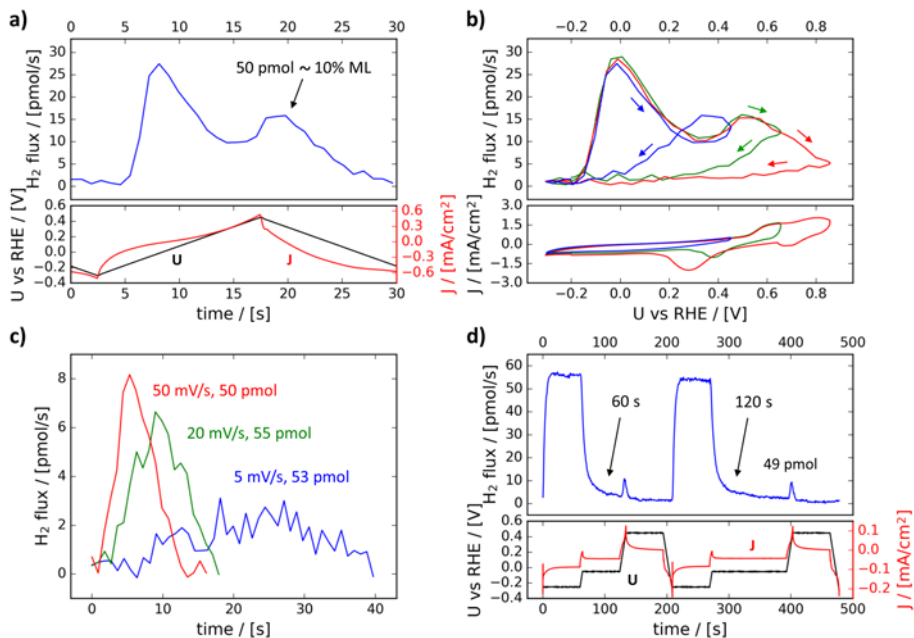
Figure 6.1: a) EC-MS plot demonstrating the electrochemical desorption of gaseous H$_2$ both at cathodic potential during HER and at potential anodic of the reversible hydrogen potential. The phenomenon shows during potential cycling from -0.3 to 0.45 V vs RHE at a scan rate of 50 mV/s. Note that the onset of the MS signal is delayed compared to the electric current and potential signals, due to diffusive transport in the stagnant thin–layer cell, as described in chapter 2. **b)** EC-MS measurements plotted as a function of potential, where the anodic potential limit is set to 0.45, 0.60 and 0.85 V vs RHE, plotted in blue, green and red, respectively. Arrows indicate the direction of the potential scan during MS data acquisition. Note again the slight time–delay. **c)** MS measurement of the anodic H$_2$ desorption feature at different scan rates, indicating a strong potential dependence. **d)** Isolation of the anodic desorption feature by resting the electrode at an intermediate potential of -0.05 V vs RHE for 60 s and 120 s, respectively, in between HER and anodic desorption. HER is performed at -0.25 V vs RHE and anodic desorption is performed by sweeping the potential to 0.45 V vs RHE with 50 mV/s. All experiments were performed in pH 12 and H$_2$ was measured on $^{m}/_{z} = 2$ and calibrated internally as described in chapter 2.

that the anodic H$_2$ remains unaffected, still yielding ~ 50 pmol, which confirms that the anodic desorption of H$_2$ is triggered by a potential change. Similar experiments were conducted with several intermediate potentials, including control experiments demonstrating no anodic H$_2$ desorption when going straight from intermediate to anodic potentials without prior HER. In Figure 6.1d HER was performed by constant–potential electrolysis at -0.25 V vs RHE for 60 s to test whether it was possible to prime the electrode with larger amounts of hydrogen prior to anodic desorption. This was likewise tested at HER durations from 10 s to 120 s, at varies cathodic potentials, again without affecting the anodic H$_2$ desorption feature. Note that the electric current feature during the anodic scan is due to double–layer capacitance charging and is thereby not associated with the H$_2$ desorption phenomenon. As seen in the cyclic voltammograms in the bottom panel of Figure 6.1b, no apparent faradaic current measurement seems to be associated with the anodic desorption of H$_2$.

6.3   Probing the mechanism

In order to probe the mechanism of the anodic H$_2$ desorption phenomenon, experiments were conducted where the cathodic and anodic potential limits were gradually varied, while cycling the potential at 20 mV/s. By gradually increasing (towards positive) the cathodic potential limit in 50 mV increments, it proved possible to isolate the anodic H$_2$ desorption feature, without any H$_2$ evolving from HER, as seen in Figure 6.1a. The crossover potential, where the primary H$_2$ feature from HER is no longer visible, is denoted the hydrogen adsorption potential, U_{ads}, which in pH 10.5 is probed to be -0.125 V vs RHE. This is in Figure 6.1a interpreted as the crossover between the last two potential increments.

Similarly, it is possible to probe the hydrogen desorption potential, U_{des}, by gradualy decreasing (towards negative) the anodic potential limit, and thereby isolate H$_2$ formation from HER, with the anodic desorption of H$_2$ no longer occurring, as shown in Figure 6.1b. The hydrogen desorption potential is in pH 10.5 probed to be 0.05 V vs RHE, taken to be the crossover between the last two potential increments in Figure 6.1b.

The above experiment was then repeated in different electrolytes spanning the pH range of 7 to 13 in order to determine the pH-dependence of the probed ad- and desorption potentials. In Figure 6.2c these results are plotted as a function of pH, with the data overlaying a Pourbaix diagram from [108]. This demonstrates, that the hydrogen ad- and desorption potentials are largely inveriant with respect to pH in the RHE scale, which eludes to the fact that the anodic H$_2$ desorption mechanism rely on a certain number of H$^+$ and OH$^-$ in solution.

A possible explanation of the phenomenon could be, that H$_2$ is released through a surface replacement reaction, where adsorbed hydrogen species are
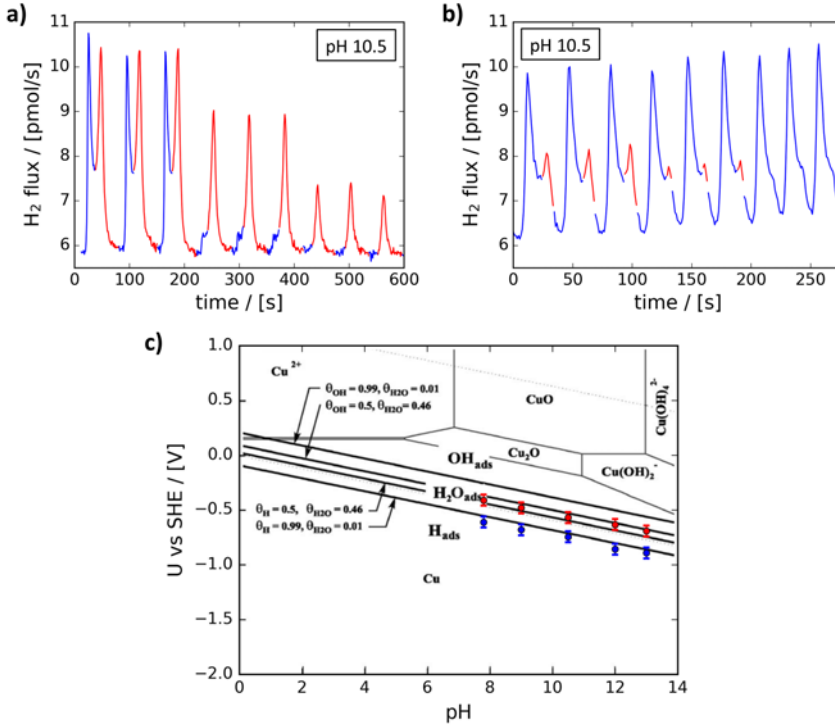
Figure 6.2: a-b) Isolation of the anodic H_2 desorption (red) and cathodic H_2 evolution by HER (blue), obtained by gradualy varying the cathodic (**a**) and anodic (**b**) potential limits in 50 mV increments, while scanning the potential at 50 mV/s. The crossover point where primary HER is no longer visible (**a**) is taken to be the hydrogen adsorption potential, U_{ads}, and the crossover point where anodic H_2 desorption is no longer visible (**b**) is taken to be the hydrogen adsorption potential, U_{des}. **c)** Hydrogen adsorbtion (blue) and desorption (red) potentials obtained from performing the experiment shown in **a)** and **b)** at pH 7.8, 9, 10.5, 12 and 13, respectively. Error bars represent the unsertainty in the evaluation of the respective crossover points, which is here set to be 50 mV, given by the size of the potential increments. The data is here plotted overlaying a Pourbaix diagram from [108] showing the calculated equilibrium potentials adsorbing hydrogen (H_{ads}), hydroxyl (OH_{ads}) and water (H_2O_{ads}) on copper (111) at 25°C. These measurements demonstrate that the H_2 desorption phenomenon is largely invariant with respect to pH on an RHE scale.

replaced with surface adsorbed OH, once the latter becomes more energetically favorable. Whether the adsorbed hydrogen species would then be in the form of *H is unclear. The fact that only $\sim 10\,\%$ of a monolayer is observed indicates that only a certain subset of surface sites, e.g. step sites, bind hydrogen strong enough to comped with the binding of OH. In Figure 6.2c calculated equilibrium potentials for adsorbed hydrogen (H_{ads}), hydroxyl (OH_{ads}) and water (H_2O_{ads}) for a Cu(111) surface at 25°C (from [108]), together with calculated H and OH coverages are co-plotted. In comparison with the measurements presented herein, this demonstrates, that anodic H_2 desorption should happen in the crossover region between H and OH each exhibiting a surface coverage of $\sim 50\,\%$. With the DFT calculations currently being carried out by Søren B. Scott, it will be possible to verify the validity of the above theory.

These experiments demonstrate another example of the importance of sub-monolayer sensitivity in EC-MS studies, here necessary due to sub-monolayer coverage of the adsorbed analyte species.

6.4   Proposed future EC-MS studies

Given the fact, that the membrane chip EC-MS system provides the posibility of dosing reactant gases in highly controlled manner, as demonstrated in chapter 2 and chapter 5, it is intriguing to test whether the Cu surface in the above mentioned experiments can be primed with gaseous H_2 as opposed to H_2O. This could be done by introducing an H_2 pulse injection through the membrane chip, while resting the electrode at an intermediate potential, as demonstrated with O_2 in chapter 5.

Surface science studies show, that gaseous H_2 adsorbs onto Cu thin films [109], indicating that this could be done. If proven possible, the natural next step would then be to prime the surface with D_2, in order to test the dynamic behavior of adsorbed hydrogen at more cathodic potentials, by scanning the potential cathodic to HER potentials, followed by an anodic desorption sweep, while looking for H_2 ($m/z = 2$), HD ($m/z = 3$) and D_2 ($m/z = 4$) in the MS. This would reveal whether the pre-adsorbed hydrogen species participates in HER or not. In either case, the result would be interesting, as it either gives insight into the fundamental reaction mechanisms of HER, or into what a Cu surface looks like at reducing conditions. Similar experiments can likewise be performed where the Cu surface is primed with D_2 prior to introducing CO or CO_2 reactant gases, which would make it possible to form isotope labeled hydrocarbon products, using pre-adsorbed hydrogen surface reactants. This would yield direct insight into the fundamental reaction mechanisms of CO_2 electroreduction.

Furthermore, given the recent focus of the influence of oxygen in the electrochemical CO_2 hydrogenation reaction, the transient CH_4 presented in chapter 5 included, the present study on surface adsorbed hydrogen might give valuable

insight into the interplay between hydrogen and oxygen in or on the surface. Maybe surface/sub-surface oxygen prevent adsorbtion of hydrogen surface reactants, and thereby alter the electrocatalytic mechanisms drastically. These are purely speculations for now, but they non the less illustrate some examples of future studies made possible by the membrane chip EC-MS methodology presented herein.

CHAPTER 7

Conclusion

The overarching goal of this thesis has been to demonstrate technical and methodological considerations that are needed in order to study minute desorption phenomena during electrochemistry experiments and thereby gain insight into the fundamental reaction mechanisms of electrochemical processes.

As discussed in the beginning of this thesis, laboratory scale electrochemistry experiments often involve desorption phenomena yielding on an order of 10^{15} analyte molecules per second. This makes mass spectrometry an ideal detection method given its instrumental capability of analyzing small amounts of gaseous analyte species with a fast time–response. Indeed, mass spectrometry is operated with pumping rates which are typically also on an order of 10^{15} molecules per second. However, coupling a mass spectrometer, with an operational pressure of $\sim 10^{-6}$ mbar directly to an electrochemical experiment is not a trivial task. Conventional methods of designing this interface rely on a membrane to separate the liquid and vacuum environments. This results in a high rate of solvent evaporation lowering sensitivity towards the analyte.

This thesis has presented a unique way of coupling a mass spectrometer directly to an electrochemical test environment by means of a microfabricated membrane chip. The membrane chip acts as an equilibration zone for volatile analyte species between the electrolyte and the MS. The membrane samples the vapor pressure of any volatile analyte into a sampling volume inside the membrane chip, which is continuously delivered to the mass spectrometer. By incorporating the membrane chip with a stagnant thin–layer electrochemistry cell, a direct coupling between analyte production at a working electrode and detection at a mass spectrometer was thereby established. Furthermore, the membrane chip enables full control of the dissolved gas atmosphere at the work-

ing electrode, allowing transient or steady-state dosing of reactant gases, as demonstrated in chapter 2. Modeling of the well-characterized mass transport in this setup makes it possible to compare the anticipated analyte collection rate, based on the current measurement from the electrode, to the measured mass spectrometer signal. As the method is refined, it will become possible to map mass spectrometer measurements directly back to a faradaic current on the surface of an electrode and thereby deconvolute the signal.

In presenting the membrane chip I have also sought to introduce a new design paradigm for inlet systems for mass spectrometry. This paradigm, introduced in chapter 1 and discussed in chapter 4, is essentially to use the standard microfabrication toolbox to facilitate the matching of the anticipated analyte production rates with the abilities of the mass spectrometer. This principle can be used together with the considerations at the end of chapter 3 to guide further improvement of the system, e.g. by tuning the pressure in the sampling volume or the temperature of the interface. There are trade-offs to consider, but these should be guided by choice and not out of necessity. While this entire thesis has focused on electrochemistry studies, it is also worth mentioning, that the same design paradigm might be equally applicable to e.g. biochemical reaction studies.

Electrochemical phenomena newly discovered using the membrane chip were presented in chapter 5 and chapter 6. Both have relevance for electrochemical reduction of carbon dioxide. chapter 5 described how oxygen exposure transiently activates Cu nanoparticles for CO reduction to CH_4. chapter 6 provides insight to the state of adsorbed hydrogen, a key surface reactant in CO_2 reduction, through observation of anodic H_2 desorption.

These two studies, in addition to providing fundamental electrocatalytic insight, exemplify the importance of the present methodology and instrumentation. Both the transient CH_4 production and the anodic H_2 desorption are examples of phenomena occuring only on a subset of the surface sites of an electrode. The transient CH_4 production is furthermore limited by faradaic efficiency below 100 % and by the fact that only a few catalytic turn-overs occur during the short lifetime of the active site. These limitations are not by any means unusual in electrochemistry studies and are therefore important to consider in order to obtain the full picture of desorption events during electrochemistry measurements. Furthermore, these studies represent both highly time-dependent and highly potential dependent electrochemical desorption phenomena, highlighting the importance of choosing the right form of potential input in electochemistry experiments. It is therefore necessary to apply the right measurement methodology, and to have sufficiently sensitive instrumentation, in order to gain insight into results like the ones shown herein.

It is my hope that the instrumentation presented herein, and the general framework that it represents, will lead to more in-depth studies of sub-monolayer desorption phenomena in the future. This will accelerate advances in electrocatalysis, contributing to the transition to a more sustainable future.

Appended content

This chapter included supplementary figures and procedures helping to clarify the description and functionality of the EC-MS instrumentation presented in this thesis.
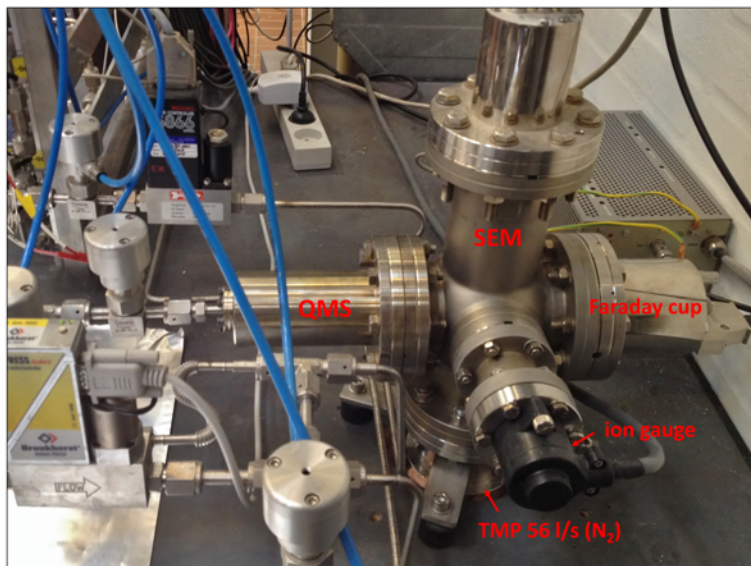
A.1 Experimental setup

Figure A.1: Close up photograph of the Pfeiffer QMA 125 quadropole mass spectrometer (QMS) used for this PhD work. The QMS uses an open axial beam filament for ionization at $100\,\mathrm{eV}$ and a Pfeiffer QMA 125 with a 90 degree secondary electron multiplier (SEM) or a Faraday cup for detection. The QMS is pumped with a single turbo molecular pump (TMP), also from Pfeiffer, with a pumping speed of 56 l/s (N_2).
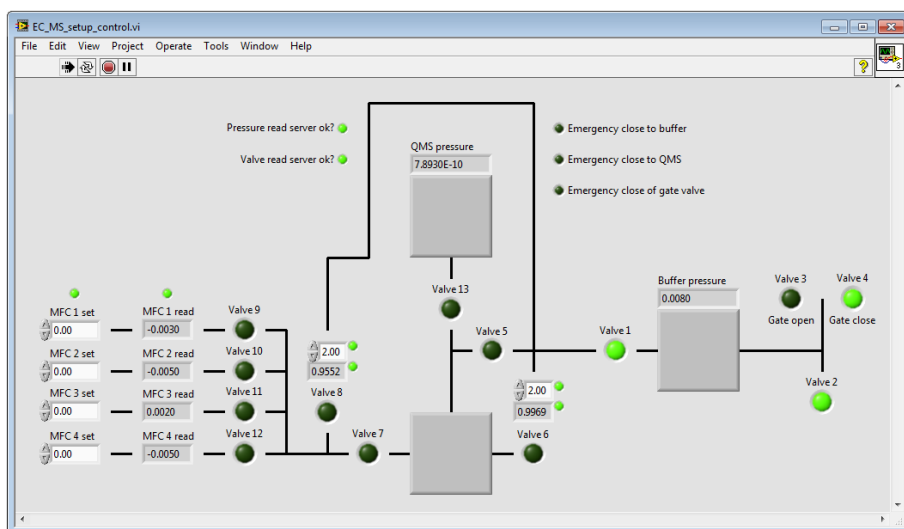
Figure A.2: EC-MS setup control panel program, built with a Lab-View based front-end and a Python based back-end. All components are interfaced with Python drivers communicating through RS-232 serial connections and controlled using socket-server network variables. This control software enables a high degree of control of chip pressures (front and back) and carrier gas feeds.
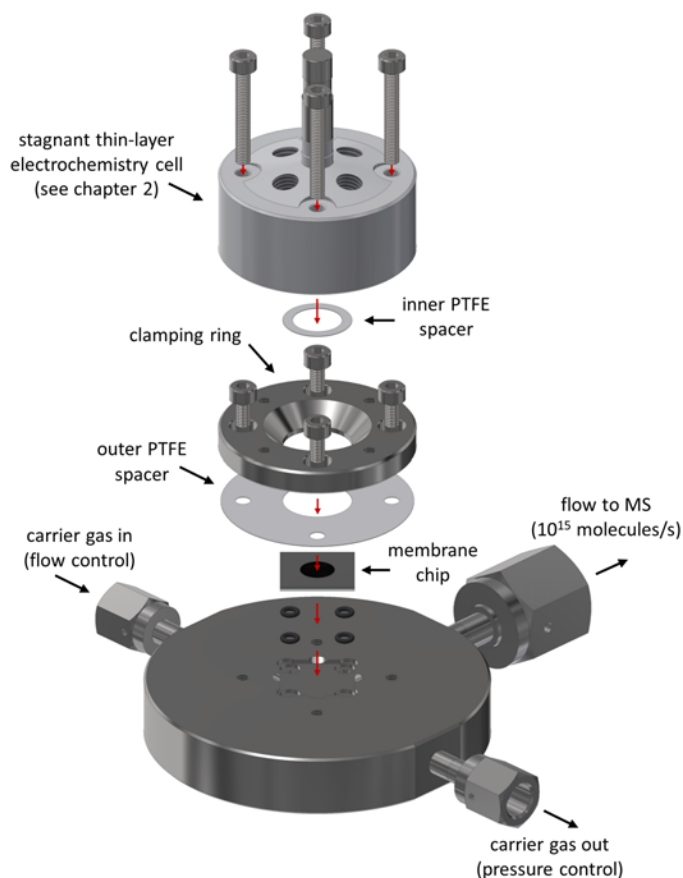
A.2 Full EC-MS cell assembly

Figure A.3: 3D rendering of the full assembly of the membrane chip electrochemistry mass spectrometry (EC-MS) setup. The stagnant-thin layer EC cell is assembled as shown in Figure 2.4 in chapter 2. The membrane chip is connected to the carrier gas feed, pressure control and the mass spectrometer via the interface flange shown in Figure 4.3. A set of Viton O-rings are used to make a gas tight connections between the membrane chip and the interface flange, which in turn is connected to gas and vacuum with UHV compatible VCR connections. An inner PTFE spacer is used to ensure a well–defined working distance between the working electrode in the EC cell and the membrane, and to make tight leak free seal against the membrane chip. An outer PTFE spacer is use to level the EC cell in order to ensure a uniform force distribution on the inner spacer.
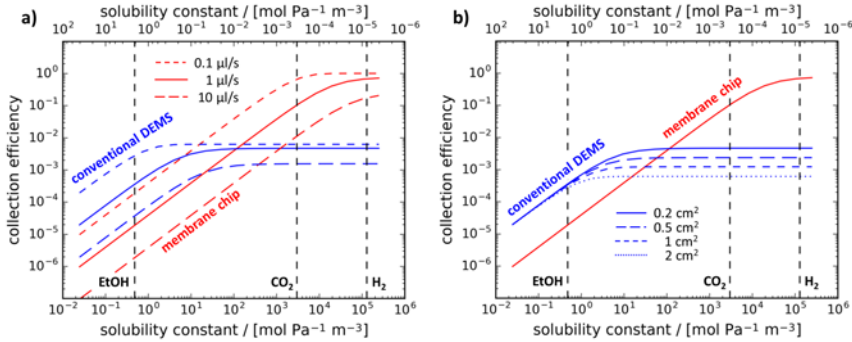
A.3   Extra modeling data

Figure A.4: Modeling of the total collection efficiency in the membrane chip (red) and conventional DEMS (blue), as shown in main figure Figure 3.3b, but here plotted at **a)** different flow rates and at **b)** different membrane areas. The former illustrates that at flow rates above $\sim 1\mu l/s$, mass transport starts to become diffusion limited, resulting in less than 100% membrane collection efficiency even for volatile species like H_2. This effect is independent of the membrane inlet system. The latter illustrates, that the membrane area can scale arbitrarily on the membrane chip, given the coupling of liquid–gas and gas–vacuum mass transport, whereas the total collection efficiency scales with membrane area in conventional DEMS, given a gradually larger water evaporation.

A.4   Membrane chip microfabrication scheme

1. The silicon chip is fabricated from a *silicon-on-insulator* (SOI) wafer with a $10\,\mu$m thick Si device layer, a $3\,\mu$m thick buried oxide and a $\sim 350\,\mu$m Si handle wafer.
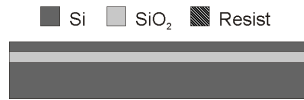
2. The first process is to etch the $2.5\,\mu$m diameter and $10\,\mu$m deep micro pores that separate the liquid and gas phases. The pattern is defined in a $1.5\,\mu$m layer of AZ MiR 701 photoresist on the device layer (front). This is used as an etch mask in a *deep reactive ion etch* (DRIE) process (SPTS Pegasus DRIE system). The etch is performed to a depth of $10\,\mu$m and stops on the buried oxide. The photoresist is then removed in an oxygen plasma.

3. A new photolithography step is carried out on the handle (back) side of the wafer. This step uses a $1.5\,\mu$m thick layer of AZ MiR 701 photoresist to define the capillary and carrier gas inlet channels of the device. The capillary is created by a $6\,\mu$m DRIE process (again on the SPTS Pegasus DRIE system). For the second iteration of the membrane chip, the capillary dimensions are 6 x 6 x $1000\,\mu$m. Again the resist is removed in an oxygen plasma.

4. In the next steps both the holes going through the wafer to the buried oxide and the $\sim 200\,\mu$m deep gas channels are formed. Since it is difficult to perform spin coating based lithography on a substrate with deep structures, these two etches are performed with the use of a latent oxide mask in the following way: First an RCA clean is performed and a $300\,$nm thermal oxide is grown. This oxide will serve as a latent etch mask later on. Next, the oxide layer is patterned by a photolithography process ($2.2\,\mu$m AZ 5214E) and BHF etch to transfer the gas channel pattern into the oxide layer. The resist is again removed by an oxygen plasma.

5. In the next step another photolithography step ($2.2\,\mu$m AZ 5214E) is used to define the pattern of the $100\,\mu$m diameter through holes which coincides with the ends of the deep gas channels defined in the previous step. The wafer is then subjected to a DRIE process to a depth of about $\sim 200\,\mu$m.
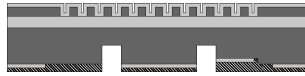
6. The resist layer is then stripped in an oxygen plasma and the wafer is subjected to a new DRIE process. This process will etch both the through holes and the gas channels using the latent oxide mask revealed by removing the photoresist mask. This etch is again performed to a depth of $\sim 200\,\mu$m, at least in the channel regions. In the through hole areas the etch will stop on the buried oxide.
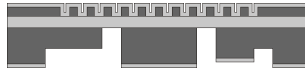
7. In the next step, the buried oxide layer is etched away to create a suspended membrane. This is done by immersing the wafer into a $40\,\%$ HF solution for 8 min. This step is timed, in order to leave buried oxide in selected regions to form a mechanical support structure for the membrane.

8. An RCA clean is then performed and a $50\,$nm thermal oxide is grown (not shown in figure). The wafer is then anodically bonded at $400°$C to a Pyrex wafer hereby creating the sealed gas channels. Prior to bonding $1\,$mm diameter holes has been cut in the Pyrex wafer to create inlet and outlet holes. This is done with a CO_2 laser.
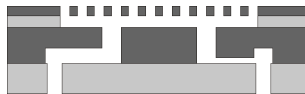
A.5 Dip-stick membrane chip
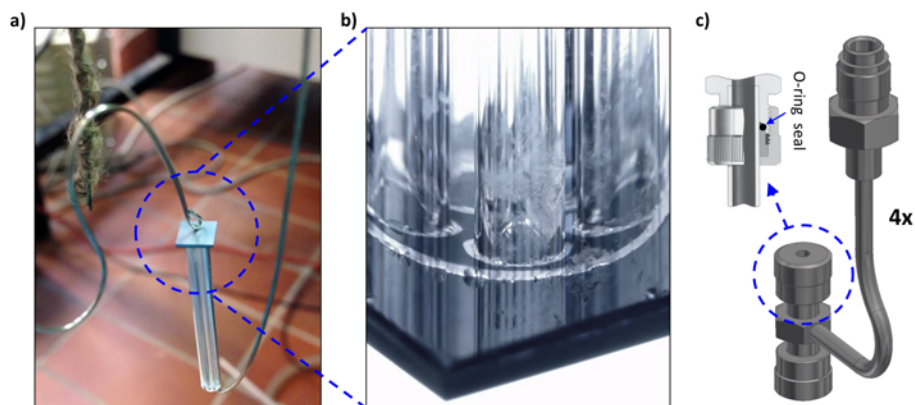
Figure A.5: a) Bonding of a microchip to the end of a polished glass tube containing four inner gas channels. **b)** Microscope image showing successful bonding, indicated by the lack of Newton rings around each inner gas channel. **c)** Illustration of the interface module for connecting the dip-stick membrane chip to carrier gas feed, pressure control and UHV. The module consist of four UltraTorr unions with a Swagelock VCR connection on the center nut. The double UltraTorr connections then form a sealed enclosure around four separate holes along the glass tube.
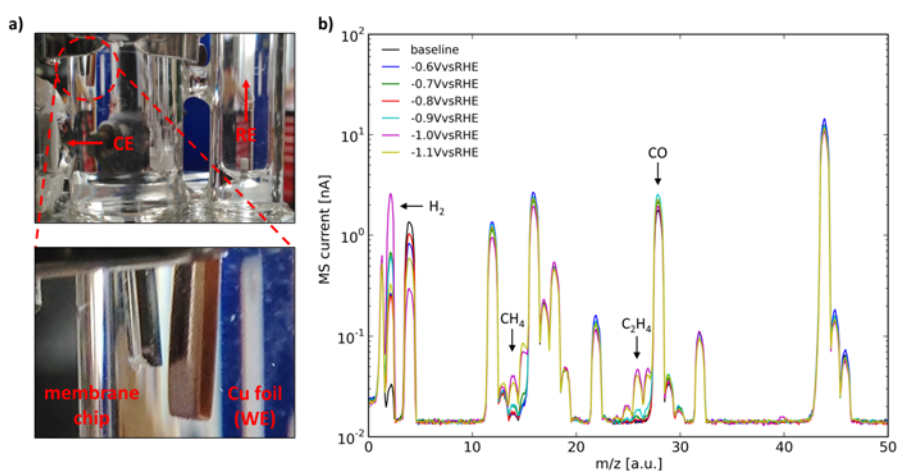
Figure A.6: **a)** Introduction of the elongated membrane chip into a standard H-cell for monitorization of the electrochemical reduction of CO_2 to hydrocarbons. **b)** Experimental results, indicating the presence of CO_2 electroreduction products at different working electrode potentials. The trend in product formation as a function of temperature, resembles what is known from literature [85], but due to in ill-defined mass transport between the electrode and the membrane, any quantitative conclusion are hard to make.

Appended publications

Paper I

Fast and sensitive method for detecting volatile species in liquids [P1]
Daniel. B. Trimarco, Thomas Pedersen, Ole Hansen, Ib Chorkendorff, and Peter
C. K. Vesborg

Fast and sensitive method for detecting volatile species in liquids

Daniel B. Trimarco,[1] Thomas Pedersen,[2] Ole Hansen,[2] Ib Chorkendorff,[1]
and Peter C. K. Vesborg[1,a)]
[1]*Department of Physics, Technical University of Denmark, Fysikvej, Building 312,*
DK-2800 Kgs. Lyngby, Denmark
[2]*Department of Micro- and Nanotechnology, Technical University of Denmark, Ørsteds Plads, Building 344,*
DK-2800 Kgs. Lyngby, Denmark

This paper presents a novel apparatus for extracting volatile species from liquids using a "sniffer-chip." By ultrafast transfer of the volatile species through a perforated and hydrophobic membrane into an inert carrier gas stream, the sniffer-chip is able to transport the species directly to a mass spectrometer through a narrow capillary without the use of differential pumping. This method inherits features from differential electrochemical mass spectrometry (DEMS) and membrane inlet mass spectrometry (MIMS), but brings the best of both worlds, i.e., the fast time-response of a DEMS system and the high sensitivity of a MIMS system. In this paper, the concept of the sniffer-chip is thoroughly explained and it is shown how it can be used to quantify hydrogen and oxygen evolution on a polycrystalline platinum thin film *in situ* at absolute faradaic currents down to ~30 nA. To benchmark the capabilities of this method, a CO-stripping experiment is performed on a polycrystalline platinum thin film, illustrating how the sniffer-chip system is capable of making a quantitative *in situ* measurement of <1 % of a monolayer of surface adsorbed CO being electrochemically stripped off an electrode at a potential scan-rate of 50 mV s^{-1}. © *2015 AIP Publishing LLC.* [http://dx.doi.org/10.1063/1.4923453]

I. INTRODUCTION

In many scientific as well as industrial fields, it is of interest to measure the amount of a certain species dissolved in a liquid and to do so with a high sensitivity and fast time-response. For instance, in the field of electrocatalysis, where many different products are electrochemically evolved at an electrode submerged in an aqueous electrolyte,[1] or in the field of biotechnology where, e.g., carbon dioxide is evolved in fermentation processes.

A fast and precise way to measure such species is using a vacuum based mass spectrometer (MS), such as a quadrupole mass spectrometer (QMS). It is naturally not possible to expose a QMS vacuum instrument directly to a liquid bath, but if it is possible to extract the species from the liquid phase and into the MS, this is a very useful method.

This paper presents a microchip, the "sniffer-chip," which is able to extract volatile species from liquids and send them directly to a MS for measurement, all in a novel fashion, which results in a higher sensitivity and faster time-response than known techniques can provide.

A. Previous technologies

Today there are two types of technologies making use of a MS for detection of species dissolved in liquids. These can be categorized as follows.

- Membrane inlet/introduction mass spectrometry (MIMS) (see Figure 1(b)).[2,3]

- Differential electrochemical mass spectrometry (DEMS), also referred to as on-line electrochemical mass spectrometry (OLEMS) (see Figure 1(a)).[4–7]

These two technologies are at first glance quite similar and their acronyms are sometimes used interchangeably, but they represent a simple grouping of the known technologies, which fall into two distinct categories. A simplified schematic of each technology is presented in Figures 1(a) and 1(b).

In MIMS a relatively thick permeable membrane, e.g., dimethyl silicone with a thickness of ~0.5 mm–1.0 mm, is often used to separate the liquid and the MS vacuum chamber. This allows small amounts of solvent and solute to diffuse through the membrane material and directly into the mass spectrometer. The flux of species through the membrane depends on the pressure difference across the membrane, the thickness and area of the membrane, and the solubility and diffusivity of the species inside the membrane. Thus, by using a thick solid membrane the flux is reduced to a limit that makes it possible to maintain a low pressure inside the MS vacuum chamber using a turbomolecular pump (TMP) ($<10^{-6}$ mbar), allowing the MS to operate optimally. However, this low flux results in a slow time-response of the system, which can be of the order of minutes or longer, depending on the species and membrane involved.[2,3] The solubility and diffusivity of species inside the membrane also vary from species to species, which can be an advantage, since a membrane selective towards a certain species may be used, but that in itself can also be a disadvantage, as no two species behave similarly.

In DEMS/OLEMS on the other hand there is a stronger focus on the time-response, which is often poor in MIMS systems. Therefore, DEMS systems often use a much thinner

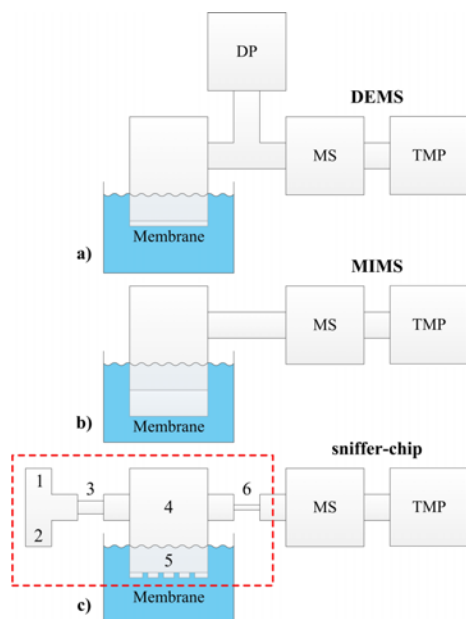a)peter.vesborg@fysik.dtu.dk; URL: http://www.fysik.dtu.dk/.

FIG. 1. Schematic block diagram of differential electrochemical mass spectrometry (DEMS), membrane inlet mass spectrometry (MIMS), and the sniffer-chip concept. The sniffer-chip is enclosed by a red dashed line and each part of the conceptual structure is numbered and explained in the main text. The same numbering is used in Figure 2 illustrating the practical realization of this concept in the form of a silicon microchip. The sniffer-chip and MIMS system are coupled to a mass spectrometer (MS) and a turbomolecular pump (TMP), and the DEMS systems are furthermore coupled to a diaphragm pump (DP) for differential pumping.

membrane, either made from a solid permeable material like the dimethyl silicone used in MIMS, or a porous and hydrophobic material like, e.g., Gore-Tex with pore sizes down to ~20 nm, both typically supported by a glass or steel frit.[6] In either case, the advantage is that flux of solvent and solute through the membrane are much higher, which leads to a faster and non-discriminating time-response. The downside, however, is that this high flux leads to a large pressure in the MS vacuum chamber, preventing the MS from working properly. In order to prevent this pressure rise, a differential pumping stage (DP) is therefore introduced between the membrane and the MS, hence the word "differential" in the name. This is typically a diaphragm pump, which brings the pressure down to about ~1 mbar, after which the TMP backing the MS vacuum chamber is able to maintain a reasonable working pressure $<10^{-6}$ mbar.[6] The gas flow out through the differential pumping stage is ~99 % of the total flow and thus only ~1 % of the total gas flow is flowing to the MS. The gas that is pumped away contains evaporated solvent and solute in proportions equal to those in the liquid, so most of the analyte is thereby lost. Thus, a differential pumping stage intrinsically causes a drop of at least a factor of 100 in

sensitivity compared to MIMS, depending on the particular differential pumping system used. Another consequence of the high gas flux can be a rapid local cooling near the membrane causing a risk of the inlet freezing or an up-concentration of the electrolyte, both due to water evaporation. Also a high water evaporation leads to a high water background in the MS resulting in high cracking signals of H_2 and O_2, so in the case of electrochemical hydrogen- and oxygen evolution reaction studies, the sensitivity of the system is reduced even further.

To sum up, a MIMS-like system maintains a low gas flux into the MS vacuum chamber by, e.g., having a thick membrane inlet. This results in a high sensitivity as the species being measured are sent directly to the MS, but leads to an intrinsically slow time-response. In a DEMS-like system, a much larger gas flux is realized by, e.g., using thinner or even porous membranes. This leads to a much faster time-response, but at the same time a drop in sensitivity of at least a factor of 100 due to the use of a differential pumping stage. Many variations of the generalized DEMS and MIMS systems of course exist, but they all fall into either of the two categories. Either way, a compromise between high and low gas flux regarding sensitivity and time-response has to be made and the question of making use of a differential pumping stage or not is common for all.

II. THE SNIFFER-CHIP

The sniffer-chip combines the best of both worlds, i.e., the fast time-response of a DEMS system and the high sensitivity of a MIMS system, since a differential pumping stage is not needed.

A. Concept

The concept of the sniffer-chip is schematically shown in Figure 1(c) and goes as follows: an inert carrier gas, e.g., He, is let in through the carrier gas inlet (1) after which most of it flows directly out again through a pressure controller outlet (2). The remainder of the carrier gas flows through an inlet capillary (3), which acts as a restricting channel section that increases the flow-velocity and thereby prevents back-diffusion from the following chamber. This part of the carrier gas flows through a low volume gas-chamber (4) underneath a perforated and hydrophobic membrane (5), which supports a liquid-gas interface. The absolute pressure in (4) is maintained at the ambient pressure in the liquid using the pressure controller at (2), to prevent collapse of the liquid-gas interface. Thereby it is able to support a large liquid-gas interface area, across which volatile species can diffuse and evaporate. Due to the partial pressure difference across the liquid-gas interface, the carrier gas is continuously saturated with analyte from the liquid, being either liquid or gaseous species, and naturally vapor from the solvent itself. From (4) the carrier gas, now saturated with measurable species, flows through a narrow outlet capillary (6), over which a pressure drop from ~1 bar (ambient pressure) to $<10^{-6}$ mbar occurs. The saturated carrier gas is then let directly to a MS for detection. It is important that the gas chamber (4), and the
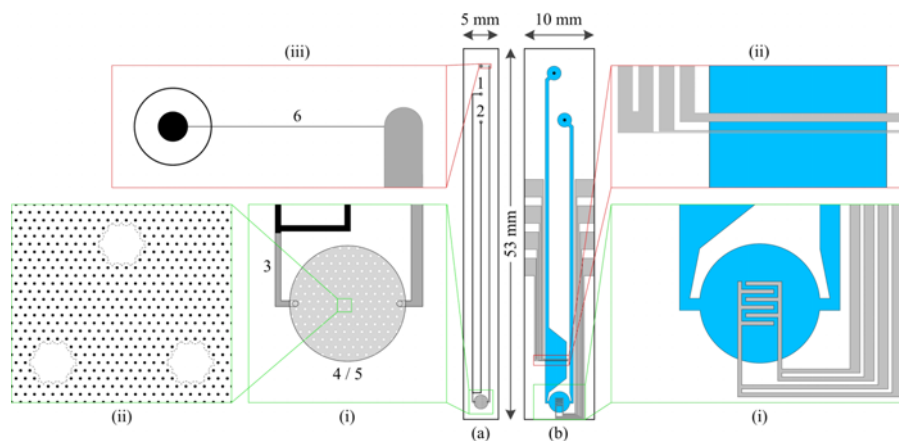
FIG. 2. Illustration of the sniffer-chip projected view with both front- and backside overlaid (a) and electrode-chip (b). Both illustrations contain zoom boxes of relevant structures and on the sniffer-chip each part of the structure is numbered with the same numbering as in Figure 1 showing a schematic block diagram of the sniffer-chip concept. Both the numbering and the zoom boxes are referred to and explained in the main text.

downstream gas channels for that matter, has a small internal volume in order for the residence-time of the atmospheric pressure part of the system to be kept at a minimum. This residence-time defines the time-response of sniffer-chip. After the capillary (6), the gas flow can be assumed to be ballistic (free molecular flow) and hence very fast.

B. Practical realization

The practical realization of the sniffer-chip concept is a micro-fabricated silicon chip made by standard clean room techniques. The primary reason for this is to make it easy to fabricate all parts of the system in a well defined and simple manner and to keep the internal volume of the pre-vacuum gas system small, the importance of which was previously mentioned. Thus, all parts enclosed by the red/dashed box in Figure 1(c) are made in a one silicon chip design. The same concept could also be realized otherwise, through, e.g., micro-machining in stainless steel. In Figure 2(a), an illustration of the sniffer-chip is shown in a projected view, with both front- and backside overlaid. In Figure 3, a simplified fabrication process flow for the sniffer-chip is shown together with an electrode-chip that will be described in Section II C.
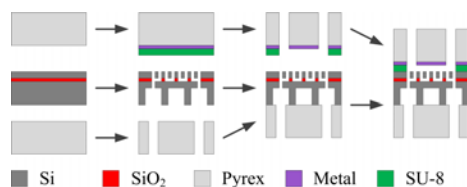
FIG. 3. Simplified fabrication process flow for the sniffer-chip and the electrode-chip illustrating their individual internal structure as well as the structure of the full two-chip assembly.

Following the bottom part of this process flow helps understanding how gas channels and chambers are connected inside the sniffer-chip. In Figure 4(a) a photograph of three sniffer-chips is shown, presenting the membrane, the gas channel system, and the three interfacing holes simultaneously. The sniffer-chip presented in this paper is designed in an elongated fashion with the membrane in one end and interfacing gas
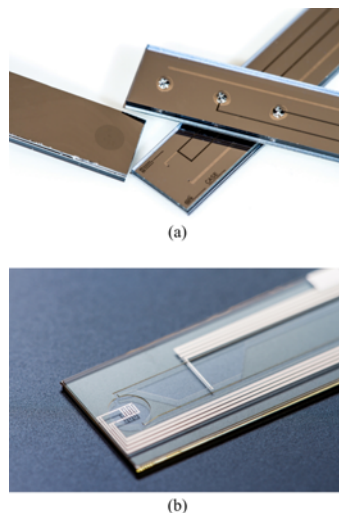
FIG. 4. Photographs of the sniffer-chip (a) and the electrode-chip (b), respectively. In (a), three sniffer-chips are stacked to make the membrane, the gas channel system, and the interfacing holes visual simultaneously. In (b), the channel system defined in the 100 m thick layer of SU-8 is seen.

holes in the other. This is done on order for the chip to easily dip into various liquids for basic testing and electrochemical experiments.

The sniffer-chip is made from a 100 mm silicon on insulator (SOI) wafer with a 15 μm device layer, a 3 μm oxide layer and a 330 μm handle wafer, and a 100 mm Pyrex wafer with a thickness of 500 μm. The assembled sniffer-chip itself is 5 mm by 53 mm with a total thickness of 848 μm. The membrane is defined in the device layer co-planar with the chip surface and all gas channels are defined on the backside of the chip in the handle wafer. All structures, including the holes perforating the membrane, are etched using deep reactive ion etching (DRIE).[8] The membrane is released in a timed wet hydrofluoric acid (HF) etching process that removes the underlying oxide layer under part of the perforated membrane, but leaves an array of supporting oxide pillars for improved mechanical stability. In this fashion, a fully connected 3 μm tall gas-chamber is formed below the membrane. The gas channels on the backside and the gas chamber beneath the membrane are connected with two through-holes, also formed in DRIE. The gas channels on the backside are sealed off with Pyrex using anodic bonding, which completes the assembly.[9] Three through-holes are drilled in the Pyrex with a CO$_2$-laser in order to interface with the gas channels. Finally, the frontside of the sniffer-chip, i.e., the membrane, is coated with 1H, 1H, 2H, 2H–perflurodecyltrichlorosilane using molecular vapor deposition (MVD) to make it hydrophobic. The layout of the gas channels, and the actual interfacing with a macroscopic gas handling system, is similar to that used in the so-called μ-reactor, which was developed in our group in 2009.[10]

Following the illustration in Figure 2(a), with the block diagram in Figure 1(c) in mind, the design and function of the sniffer-chip goes as follows. The carrier gas is let in through (1) and downward through a 40 mm long and 100 μm wide channel to a Y-crossing. The main part of the carrier gas is then let out to the pressure controller at (2) through a similar channel, while the remainder of the gas flows through a capillary inlet (3) towards the gas chamber (4) underneath the membrane (5). The initial channel system (1-2) acts as an on-chip pressure regulated carrier gas reservoir and is etched to a depth of ~200 μm to ensure low pressure drop even at high flow-rates. This gas flow is of the order $1 - 10$ ml min^{-1} and ensures a short residence-time in the external gas control system and a flow-rate in a range controllable with standard mass flow controllers (MFC). Finally, this high flow-rate helps to keep the gas-stream at the entrance to the gas-chamber pure.

Illustrated by the zoomed box marked by green in Figure 2(a), (i) a small fraction of the carrier gas is the lead from the Y-crossing through a 1.5 μmm long and 100 μm wide channel (3). This channel section, as well as the remainder of the channel system on the backside of the sniffer-chip, is etched to a depth of 3 μm. In this channel section in particular, the small cross-section ensures a high flow velocity and thereby a minimal back-diffusion from the gas chamber (4). From here the carrier gas is lead through a ~300 μm long through-hole with a diameter of 100 μm to the other side of the sniffer-chip to the gas-chamber (4), which has a diameter of 2.0 mm and a height of 3 μm given by the thickness of the buried oxide layer. The perforation of the under-etched

membrane is ~7.3% and the holes are 3 μm in diameter placed in a honeycomb mesh. To ensure mechanical stability of the membrane, it is supported under ~10% of its area by silicon dioxide support pillars with a diameter of ~50 μm. The support pillars are formed by careful timing of the HF etch for releasing the membrane. The final etching front is marked by a dashed line in Figure 2(a) (ii) (second green box) and the resulting volume of the under-etched gas chamber is ~8.5 nl. A secondary electron multiplier (SEM) micrograph of the perforated membrane after release etch is shown in Figure 5.

The FDTS treated silicon surface has a water contact angle of ~110° at room temperature and the FDTS coating covers all surfaces of the chip, including top and bottom surfaces of the membrane as well as the perforation holes. Using the dimensions of membrane holes, the curved liquid gas interface can be expected to support a pressure difference of ~33 kPa before water breaks through.

After the gas chamber (4), the carrier gas is once again led out through a vertical through-hole to the backside of the sniffer-chip, where a 48 mm long and 200 μm wide channel leads it to a narrow capillary (6) at the top of the sniffer-chip as seen in Figure 2(a) (iii) (red box). The long channel section is made wide as a compromise between minimal flow resistance and minimal volume, and thereby minimal residence-time. It is desired that the flow-rate is dominated by the capillary at the end (6). The capillary is ~1 mm long and has a cross-section of 5 μm by 3 μm. The pressure drop across this capillary alone is practically of the order 1 atm resulting in a pressure on the backside of the capillary of the order 10^{-6} mbar. Thus, it is possible to connect the sniffer-chip directly to a MS without the use of differential pumping.

The total internal volume of the sniffer-chip after, and including, the gas chamber is ~31 nl and the flow-rate through the capillary to the MS is ~1.5×10^{15} molecules s^{-1} or ~60 nl s^{-1} with atmospheric pressure inside the chip. This results in a ~0.5 s residence-time of the sniffer-chip, which gives the chip an almost instant time-response and since the
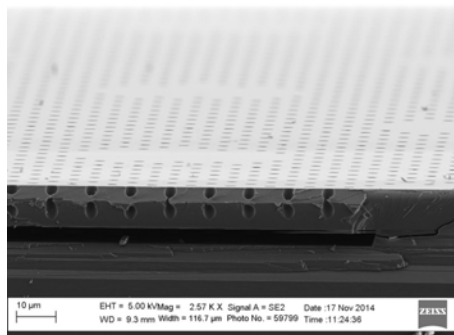

FIG. 5. SEM micrograph of the membrane showing the perforating holes, the under-etched gas chamber, and the silicon dioxide support pillars. The sample is imaged at a tilt angle of 80 degrees. In order to enhance depth of field, it is composited of seven images obtained at varying working distance.

capillary outlet allows the chip to be coupled directly to a MS, no compromise is made in terms of sensitivity. This is what makes the sniffer-chip unique compared to the existing DEMS and MIMS systems. By avoiding the liquid-vacuum interface in the DEMS system, the sniffer-chip also benefits from much less solvent evaporating into the analyte gas stream in sniffer-chip, since the carrier gas saturates at the vapor pressure of the solvent and solvent transfer is thus, in the worst case, limited to the vapor pressure equilibrium. In comparison to the MIMS system this membrane also treats all species equally, where the MIMS membrane acts preferentially towards some species.

From a functional perspective, the sniffer chip can be considered a "micro-fabricated silicon membrane," which interfaces the liquid phase to the QMS and extracts volatile species from the liquid. In this paper the sniffer-chip is exemplified in an elongated version, but the chip can just as well have a square form factor with a membrane in the middle, coplanar with the surrounding silicon. In effect, the sniffer-chip is practically interchangeable with the Gore-Tex membrane used in most DEMS setups, except from the interfacing of the carrier gas inlet and pressure regulating outlet of the sniffer-chip. Thereby, standard DEMS cell configurations are directly applicable with the sniffer-chip, being either rotating disc electrode (RDE) DEMS cells,[11–13] thin layer DEMS cells,[14,15] hanging meniscus DEMS cells,[16–18] or others.[7,19–23]

C. The electrode-chip

With the membrane of the sniffer-chip directly exposed to ambient and with the elongated design of the chip, it is easy to dip the sniffer-chip into an aqueous solution and measure any volatile species dissolved in it. This approach can, e.g., be applied to interface the sniffer-chip with a macroscopic electrochemical cell and measure products evolved at the working electrode. However, as previously realized in the field of DEMS studies,[6] it is difficult to quantify the product formation in a reproducible manner in this case, since the distance between the working electrode (WE) and the sniffer-chip membrane is ill defined. It is also difficult to get the sniffer-chip in close enough proximity to the WE to collect all products. As a result the bulk electrolyte may saturate, which results in a drifting background signal. Therefore, in order to make quantifiable benchmark measurements with the sniffer-chip an add-on electrode-chip was developed. The electrode-chip comprises electrodes and fluidic channels for the electrolyte and is inspired by the thin layer DEMS cell concept known from the literature,[6,14,15] but with both WE, counter electrode (CE), and reference electrode (RE), as well as microfluidic channels on a single microchip. Together with sniffer-chip the electrode-chip thereby forms an enclosed two-chip assembly, a form of electrochemical flow cell, giving full control of the electrochemical environment inside. In Figures 2(b) and 4(b), a schematic illustration and a photograph of the electrode-chip are shown, respectively. Once again, Figure 3 shows a simplified fabrication process flow of the sniffer-chip together with the electrode-chip, which in the final panel also illustrates how the completed assembly looks. Again this is just one practical realization of a general concept, where the main point is that the capabilities of the sniffer-

chip regarding electrochemical measurements and product detection are fully realized by interfacing it with a sort of electrochemical flow cell, in this case demonstrated by the "electrode-chip."

The electrode-chip is a Pyrex chip with metal electrodes deposited using e-beam evaporation in a 200 nm thick layer and patterned with standard UV lithography. On top of the electrode pattern, a 100 μm thick SU-8 film is spun on and a channel system is the defined in the SU-8 film by UV lithography. Inlet and outlet holes are made through the Pyrex using a CO_2-laser after electrode deposition and SU-8 processing. By clamping the electrode-chip onto the sniffer-chip, the channels defined in SU-8 are sealed against the device layer of the sniffer-chip. The electrodes of the electrode-chip are positioned exactly above the membrane at a distance defined by the thickness of the SU-8 layer, in this case 100 μm. The electrode-chip design used here is a simple SU-8 channel system, which brings the electrolyte through 500 μm wide channels to and from a liquid chamber with a diameter of 3000 μm aligned above the sniffer-chip membrane of 2.0 mm in diameter. The metal electrodes are defined in a double comb pattern as seen in Figure 2(b) (i) (green zoom-box). The wires are 100 μm wide and 100 μm apart and the total wetted area of each wire comb is 0.44 mm². Downstream from the double comb electrodes another 100 μm wide electrode is defined, crossing a 3.0 mm wide channel section as seen in Figure 2(b) (ii) (red zoom-box). The thinner electrodes defined in the wide channel section constitute a controlled hydrogen reference electrode (not used in this study). By applying a potential across the two double comb electrodes, or between the double comb electrodes and the upstream electrode, a range of simple two electrode-experiments can be performed, as will be described in further detail in Section IV.

III. CALIBRATION

In order to calibrate the sniffer-chip, it is important to know the exact molecular flow-rate through the capillary of the sniffer-chip. By relating the QMS signals of a measurement to this flow-rate using independent calibration measurements of various gas compounds, it can be converted into a measure of the composition of the molecular flow and thus the molecular flow-rate of each compound.

The molecular flow-rate through the sniffer-chip is calculated using the following expression:[10]

$$\dot{N} = \frac{1}{k_B T} \frac{1}{l} \left[\left(\frac{\pi}{8} \frac{\bar{p} a^4}{\mu} + \frac{8}{3} \sqrt{\frac{\pi}{2}} \frac{a^3}{\nu} \frac{1 + 2\frac{a\nu\bar{p}}{\mu}}{1 + 2.48\frac{a\nu\bar{p}}{\mu}} \right) \right.$$
$$\left. \times (p_1 - p_2) + \frac{8}{3} \sqrt{\frac{\pi}{2}} \frac{a^3}{\nu} (p_2 - p_3) \right], \quad (1)$$

where k_B is Boltzmann's constant, T is the temperature and μ is the dynamic viscosity of the gas in question, which in itself is highly dependent on temperature derived from assuming a circular cross section capillary with the length l and radius a through which the flow undergoes a transition from intermediate Knudsen flow to a molecular flow. The pressure at the inlet and outlet of the capillary is p_1 and p_3, respectively, and p_2

represents the transition pressure at which the mean free path of the gaseous molecules becomes comparable to the dimensions of the capillary,

$$p_2 = \frac{k_B T}{\sqrt{2}\pi s^2 \lambda}, \qquad (2)$$

where λ is the mean free path of the molecules and s is the molecular diameter. $\bar{p} = \frac{p_1 + p_2}{2}$ and $v = \sqrt{m/k_B T}$ where m is the molecular mass.[10]

The molecular flow-rate can also be measured experimentally[10] by sealing of inlet (1) of the sniffer-chip as well as the membrane (5) (see Figure 2(a)) and coupling outlet (2) to a Baratron and the capillary outlet (6) to a turbomolecular pump. Thus, the internal volume of the sniffer-chip is pumped down through the capillary only. By measuring the pressure, p, as a function of time using the Baratron, it is thereby possible to calculate the molecular flow-rate, using the ideal gas law, as follows:

$$\dot{N}(t) = \frac{V}{k_B T} \frac{dp(t)}{dt}. \qquad (3)$$

For the current design of the sniffer-chip, both calculated and measured flow-rates yield $\sim 1.5 \times 10^{15}$ molecules s^{-1} or ~ 60 nl s^{-1} at 1 atm pressure in the sniffer-chip.

This flow-rate depends rather strongly on which gas is passed through the chip and under which conditions: the gas composition and flow-rate through the carrier gas reservoir (1-2) determine the local pressure in the gas chamber (4). The flow through the capillary is thus dependent on the local pressure in the chip, viscous and molecular properties of the gas, and the temperature.

Thus, an internal standard, e.g., 1% Ar in the He carrier gas, or the He carrier gas itself is used to calibrate the flow-rates of the other components in the stream. By normalizing to the QMS signal of the internal standard, the above changes are corrected for. In order to correct for changes in the QMS, e.g., drift in SEM currents or variations in ambient conditions, both during experiments and from time to time, the QMS signal of the internal standard is measured before and after experiments.

Calibration constants for every gas measured in experiments are found by conducting a measurement on a well-defined gas mixture, where the gases in question are mixed into the carrier gas in small but well-defined amounts. If the gas mixture is dominated by a carrier gas, the calibration constants can be calculated as follows:[24]

$$C_n = \dot{N} \frac{f_n}{I_n}, \qquad (4)$$

where f_n is the fraction of the nth component of the gas and I_n is the QMS current measured for the nth component. Again the internal standard is used as a measure of the actual molecular flow-rate of this calibration gas, which now has other molecular properties than the pure carrier gas. The calibration constant thus comes out as a ratio between the molecular flow-rate and the QMS signal measured and captures differences in ionization probabilities, pumping rates, etc.[24] Thus, QMS currents measured with the sniffer-chip can be converted to molecules s^{-1}.

IV. EXPERIMENTS

To demonstrate the operation of the sniffer-chip, two different experiments are performed: a faradaic measurement of electrochemical water-splitting and a transient measurement of electrochemical CO-stripping, both on a polycrystalline platinum electrode and the latter have previously been studied by DEMS.[25,26]

A. Faradaic measurement

As described in Section II C, the electrode-chip is interfaced with the sniffer-chip forming an enclosed two-chip assembly. The electrode-chip has two polycrystalline thin films of Pt with an area of 0.44 mm^2 each, operating as WE and a CE, respectively. Through the microfluidic channels of the electrode-chip, a 0.1M HClO$_4$ aqueous electrolyte is introduced and held steady during experiments. Thus, the two Pt electrodes are located above the sniffer-chip membrane with a 100 μm thin film of electrolyte in between. The electrolyte is automatically completely saturated with He within seconds via mass exchange with the carrier gas flowing under the hydrophobic membrane of the sniffer-chip. Before running the experiment, a range of cyclic voltammograms (CV) are run in the potential range of interest until the electrodes are clean and the CVs are stable.

The experiment consists of a range of chronoamperometric measurements where a constant potential is applied between the WE and CE for two minutes with two minutes of pause in between. The potential is increased from 1.6 V to 1.8 V with increments of 20 mV as seen in Figure 6 (the
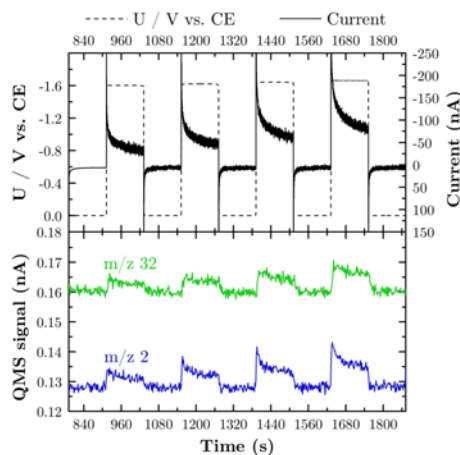
FIG. 6. Two-electrode water-splitting experiment demonstrating the operation of the sniffer-chip. The experiment is performed in 0.1M HClO$_4$ using two platinum electrodes. A potential is applied between the two while both the faradaic current and the mass spectrometer signal of $m/z = 2$ and $m/z = 32$ representing hydrogen and oxygen, respectively, are measured with the sniffer-chip. The potential is stepped up in steps of 20 mV and the H$_2$ and O$_2$ evolution is easily tracked by the QMS already at a faradaic current of ~ 30 nA.

figure only shows the first four square potential waves). The faradaic current and the QMS signal of the sniffer-chip are logged simultaneously and QMS is set to log the $m/z = 2$ and $m/z = 32$ as representations of hydrogen and oxygen evolution, respectively. As seen in Figure 6, showing raw data from the first four chronoamperometric measurements in the experiment, the QMS signals and the faradaic current measurement are correlated. There is a slight time delay in the QMS signal, matching the expected diffusion time of hydrogen and oxygen across the 100 μm thin electrolyte film. With 1D diffusion time given by $\tau_{\mathrm{diff,hydrogen}} = \frac{l^2}{2D}$, where l is the distance between the electrode and the sniffer-chip membrane and D is the diffusion constant, the expected time delay is ~0.98 s for hydrogen, although it is measured to be ~2.46 ± 0.38 s in this experiment. This can be reduced by reducing the distance between the WE and the sniffer-chip membrane, i.e., the height of the electrolyte chamber.

The lowest absolute faradaic current measured, where hydrogen and oxygen formation is still clearly measured with the sniffer-chip, is 32 ± 5.7 nA, which is a measure of the sensitivity of the system. The full capability of this particular sniffer-chip would however be utilized by having a WE covering the entire membrane area of the sniffer-chip, to utilize the large liquid/gas interface. This can be improved even further by increasing the sniffer-chip membrane area.

To quantify the experiment in Figure 6, the integrated faradaic current is compared to the integrated QMS signal for each chronoamperometric measurement corrected with calibration constants obtained in an independent calibration measurement as described in Section III. Figure 7 shows the hydrogen charge measured with the potentiostat and the QMS, respectively, and these prove to be coincident in the beginning. As the experiment progresses, the QMS signal deviates to lower values, most likely due to back-reaction at the electrodes, i.e., spontaneous hydrogen oxidation over the Pt. The amount of H_2 accounted for stabilizes at ~75% at the end of the experiment. This is due to the electrolyte saturating with H_2 after a certain duration of the experiment. Thus, in steady state and with this electrode geometry, ~25% back-reaction is taking place.
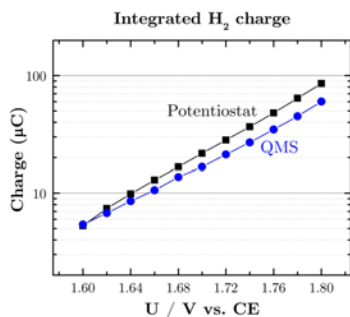

FIG. 7. The integrated hydrogen charge measured with the potentiostat and the mass spectrometer, respectively, based on the data shown in Figure 6. The discrepancy at high current is ascribed to back-reaction at the electrodes.

In summary, this experiment shows how the sniffer-chip is able to make quantitative measurements of electrochemical products formed at an electrode *in situ* at absolute faradaic currents as low as ~30 nA. The experiment was done several times and on different chips to illustrate reproducibility.

B. Transient measurement

Using the same system as before a CO-stripping experiment is performed, with the two polycrystalline thin film double comb electrodes of Pt both working as WEs with a total area of 0.88 mm². A polycrystalline Pt thin film further downstream is then used as CE. Again 0.1M HClO$_4$ is used as electrolyte. Before the experiment, the electrodes are again cleaned electrochemically until a stable CV in the potential range of interest is obtained. While holding the potential between WE and CE at −0.2 V, CO is introduced by mixing into the carrier-gas stream for 10 min after which the gas chamber of the sniffer-chip is flushed with pure He for 60 min until no CO is detected in the QMS and the electrolyte is expected to be fully saturated with He once again. The potential is then scanned to 1.2 V at a ramp-rate of 50 mV s^{-1} to oxidize the surface adsorbed CO to CO$_2$.

During the experiment, the faradaic current and the QMS signal of $m/z = 44$ representing CO$_2$ are logged simultaneously. In Figure 8, both the faradaic current and the $m/z = 44$ QMS signal are plotted as a function of potential and a correlation between the two signals is seen. The measurement thus clearly shows how the sniffer-chip is able to measure CO$_2$ coming off the electrode *in situ* during the anodic potential sweep. However, there is again a time delay of the QMS signal as well as a broadening of the CO$_2$ peak, which can both be explained by the diffusion time of CO$_2$ from the electrode through the 100 μm to the sniffer-chip membrane. The peak-to-peak time delay is measured to be 6.76 s, of which at least 2.6 s is expected from 1D diffusion. The fact that the time delay is longer than expected is most likely due to radial diffusion of CO$_2$ away from the electrode and parallel to the sniffer-chip membrane. It is also noted that the QMS signal is higher after the peak has passed indicating that not all CO$_2$ molecules have left the electrolyte at this point. As previously mentioned, this feature can be improved by decreasing the distance between the electrode and the membrane.

To quantify this CO-stripping experiment, the system is again calibrated as described in Section III. The CO$_2$ peak from the QMS signal is integrated, converted into a total number of CO$_2$ molecules and further to the total charge corresponding to that amount. Similarly, the faradaic current peak is integrated and finally a calculation of the expected CO-stripping charge is made from the geometrical surface area of the WE, assuming a surface coverage of CO of 360 μC cm^{-2}.[27] These three measures of the CO-stripping charge are shown in Table I. The discrepancy between the faradaic current integration and the geometrical surface area calculation can be explained by the roughness of the Pt electrodes, which in this case yields 1.57, slightly higher than the 1.2 often reported in the literature.[28,29] The hydrogen under-potential deposition area is measured to be 2.45 μC in CO-stripping experiment, which supports the
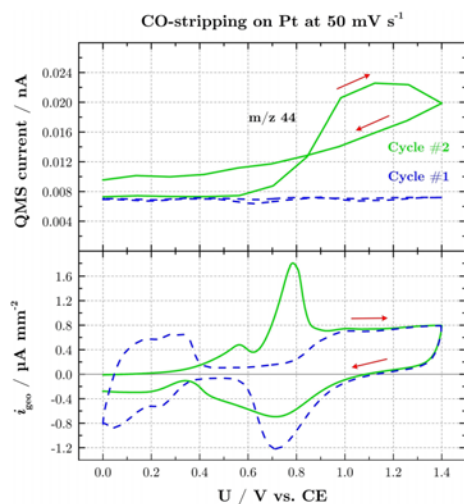
FIG. 8. CO-stripping experiment benchmarking the sensitivity of the sniffer-chip. Platinum electrodes are poisoned with CO and electrochemically stripped clean while the faradaic current and the mass spectrometer signal of $m/z = 44$ representing CO_2 are measured, respectively. Cycle #1 shows a stable Pt CV with all the expected features from polycrystalline Pt, indicated by, e.g., the hydrogen underpotential deposition (UPD) region. Cycle #2 shows the first cycle after the dosing of CO to the electrolyte. It is clear from the data that the sniffer-chip is able to measure the CO_2 coming of the electrode with a great sensitivity and good time-response.

measured area of the CO-stripping peak. The integrated QMS signal yields a slightly lower CO-stripping charge, which is most likely due to the radial diffusion of CO_2 away from the electrode as previously mentioned. The variation in the QMS signal arises from variations in the calibration experiments, which in this case were performed at a different time than the CO-stripping experiment itself.

In summary, the sniffer-chip is thus able to make a quantitative *in situ* measurement of a monolayer of surface adsorbed CO being stripped off an electrode with an area of <1 mm². Considering that the signal-to-noise ratio of this experiment is ~50 and that only part of the membrane area of the sniffer-chip is utilized, this particular sniffer-chip design is probably capable of making a quantitative *in situ* measurement of <1 %

TABLE I. Total CO-stripping charge calculated using the geometrical surface area of the Pt electrode and by integrating faradaic current and the mass spectrometer signal of the CO-stripping peak in Figure 8, respectively. With the difference between the first two ascribed to the roughness of the Pt electrode, all three measures of the CO-stripping charge yield very similar values.

Method	CO-stripping charge (μC)
Geometrical surface area	3.17
Faradaic current	4.97
QMS	4.43 ± 1.22

of a monolayer electrochemically being stripped off an electrode at a potential scan-rate of 50 mV s^{-1}.

V. CONCLUSION

The sniffer-chip represents a fast and highly sensitive method for detecting volatile species in liquids. Using an inert carrier gas flowing underneath a perforated and hydrophobic membrane and through a narrow capillary, the sniffer-chip can couple directly to a QMS, which detects the volatile species collected by the carrier gas, without the use of differential pumping. This results in an intrinsic sensitivity improvement of at least a factor of 100 compared to DEMS/OLEMS systems, while maintaining a fast time-response. Moreover, the sniffer-chip can be used in an open configuration, where the sniffer-chip is dipped into any aqueous solution and detects volatile species dissolved in the liquid, or it can be used in a closed configuration, where the sniffer-chip is interfaced with a microfluidic channel system transporting liquid across the sniffer-chip membrane under well-controlled conditions: with the closed system, represented in this paper by an enclosed two-chip assembly using an electrode-chip, the user has full control of the electrochemical environment, which makes it possible to analyze the electrochemically formed products quantitatively. Thus, the sniffer-chip is able to quantify hydrogen and oxygen evolution on a polycrystalline platinum thin film *in situ* at absolute faradaic currents down to ~30 nA and make a quantitative *in situ* measurement of <1% of a monolayer being electrochemically stripped off an electrode at a potential scan-rate of 50 mV s^{-1}. The latter sets a true benchmark of the sensitivity of the sniffer-chip system and both examples show "best in class" performance. The sniffer-chip thus represents a new concept for measuring volatile species in liquids.

The two experiments presented in this paper are examples of applications of the sniffer-chip and the chip itself is not the limiting factor in these experiments, neither when it comes to the sensitivity nor the time-response. As previously mentioned, the time-response is still limited by the diffusion of volatile species through the liquid to the membrane of the sniffer-chip. Even if the residence-time of the carrier gas inside the sniffer-chip becomes limiting, this can be improved even further. Regarding sensitivity, every single molecule is collected by the sniffer-chip as long as the electrode is in close enough proximity of the membrane. Thus, by simply utilizing more of the membrane area, or by making this even larger, the sensitivity is linearly scalable. Also, a more sensitive mass spectrometer can be used once this becomes the limiting factor. And this is where the major improvement lies with the sniffer-chip compared to DEMS/OLEMS systems: by having a liquid/gas interface suspended by a hydrophobic membrane and an ambient backing pressure of a carrier gas and by having the molecular flux to the mass spectrometer limited by a capillary, you are not only obtaining a high sensitivity without compromising the time-response of the system, it is also possible to scale the membrane area almost arbitrarily and only increase the intake of volatile analyte.

As touched upon in this paper, the sniffer-chip is especially relevant for modern research in the field of electro-

catalysis, where much work is, e.g., put into finding selective and efficient catalysts for CO_2-reduction.[30–32] By electrolyzing water saturated with CO_2 many different chemical compounds can be made,[1] so in order to understand the yet unknown reaction mechanisms of this reaction, it is important to be able to study the reaction *in situ* and to capture various reaction intermediates. Work is already done in this regard,[33] but in order to study, e.g., low coverages of nano-clusters, yielding many different electrochemical products,[34] the sensitivity and time-response of the analysis system becomes critical and must be improved. The present sniffer-chip represents a way to meet these demands and can thereby help improve *in situ* product analysis in the time to come.

1. K. P. Kuhl, E. R. Cave, D. N. Abram, and T. F. Jaramillo, "New insights into the electrochemical reduction of carbon dioxide on metallic copper surfaces," Energy Environ. Sci. **5**(5), 7050 (2012).
2. T. Kotiaho, F. R. Lauritsen, T. K. Choudhury, R. G. Cooks, and G. T. Tsao, "Membrane introduction mass spectrometry," Anal. Chem. **63**(18), 875A–883A (1991).
3. R. C. Johnson, R. G. Cooks, T. M. Allen, M. E. Cisper, and P. H. Hemberger, "Membrane introduction mass spectrometry: Trends and applications," Mass Spectrom. Rev. **19**(1), 1–37 (2000).
4. S. Bruckenstein and R. R. Gadde, "Use of a porous electrode for in situ mass spectrometric determination of volatile electrode reaction products," J. Am. Chem. Soc. **93**(3), 793 (1971).
5. O. Wolter and J. Heitbaum, "Differential electrochemical mass spectroscopy (DEMS)–a new method for the study of electrode processes," Ber. Bunsen-ges. Phys. Chem. **88**, 2–6 (1984).
6. H. Baltruschat, "Differential electrochemical mass spectrometry," J. Am. Soc. Mass Spectrom. **15**(12), 1693–1706 (2004).
7. H. Wang, E. Rus, and H. D. Abruña, "New double-band-electrode channel flow differential electrochemical mass spectrometry cell: Application for detecting product formation during methanol electrooxidation," Anal. Chem. **82**(11), 4319–4324 (2010).
8. A. M. Hynes, H. Ashraf, J. K. Bhardwaj, J. Hopkins, I. Johnston, and J. N. Shepherd, "Recent advances in silicon etching for MEMS using the ASE™ process," Sens. Actuators, A **74**(1-3), 13–17 (1999).
9. D. I. Pomerantz, "Anodic bonding," U.S. patent 3397278 A (18 May 1965).
10. T. R. Henriksen, J. L. Olsen, P. C. K. Vesborg, I. Chorkendorff, and O. Hansen, "Highly sensitive silicon microreactor for catalyst testing," Rev. Sci. Instrum. **80**(12), 124101 (2009).
11. D. Tegtmeyer, A. Heindrichs, and J. Heitbaum, "Electrochemical on line mass spectrometry on a rotating electrode inlet system," Ber. Bunsenges. Phys. Chem. **93**, 201–206 (1989).
12. S. Wasmus, E. Cattaneo, and W. Vielstich, "Reduction of carbon dioxide to methane and ethene–an on-line MS study with rotating electrodes," Electrochim. Acta **35**(4), 771–775 (1990).
13. M. Fujihira and T. Noguchi, "A novel differential electrochemical mass spectrometer (DEMS) with a stationary gas-permeable electrode in a rotational flow produced by a rotating rod," J. Electroanal. Chem. **347**, 457–463 (1993).
14. T. Hartung and H. Baltruschat, "Differential electrochemical mass spectrometry using smooth electrodes: Adsorption and H/D-exchange reactions of benzene on Pt," Langmuir **6**(11), 953–957 (1990).
15. H. Baltruschat and U. Schmiemann, "The adsorption of unsaturated organic species at single crystal electrodes studied by differential electrochemical mass spectrometry," Ber. Bunsenges. Phys. Chem. **97**(3), 452–460 (1993).
16. Y. Gao, H. Tsuji, H. Hattori, and H. Kita, "New on-line mass spectrometer system designed for platinum-single crystal electrode and electroreduction of acetylene," J. Electroanal. Chem. **372**, 195–200 (1994).
17. T. H. M. Housmans, A. H. Wonders, and M. T. M. Koper, "Structure sensitivity of methanol electrooxidation pathways on platinum: An on-line electrochemical mass spectrometry study," J. Phys. Chem. B **110**, 10021–10031 (2006).
18. A. H. Wonders, T. H. M. Housmans, V. Rosca, and M. T. M. Koper, "On-line mass spectrometry system for measurements at single-crystal electrodes in hanging meniscus configuration," J. Appl. Electrochem. **36**(11), 1215–1221 (2006).
19. Z. Jusys, "A new approach for simultaneous DEMS and EQCM: Electro-oxidation of adsorbed CO on Pt and Pt-Ru," J. Electrochem. Soc. **146**(3), 1093 (1999).
20. H. Wang, T. Löffler, and H. Baltruschat, "Formation of intermediates during methanol oxidation: A quantitative DEMS study," J. Appl. Electrochem. **31**, 759–765 (2001).
21. S. P. E. Smith, E. Casado-Rivera, and H. D. Abruña, "Application of differential electrochemical mass spectrometry to the electrocatalytic oxidation of formic acid at a modified Bi/Pt electrode surface," J. Solid State Electrochem. **7**, 582–587 (2003).
22. Abd-El-Aziz A. Abd-El-Latif, J. Xu, N. Bogolowski, P. Königshoven, and H. Baltruschat, "New cell for DEMS applicable to different electrode sizes," Electrocatalysis **3**, 39–47 (2012).
23. J.-P. Grote, A. R. Zeradjanin, S. Cherevko, and K. J. J. Mayrhofer, "Coupling of a scanning flow cell with online electrochemical mass spectrometry for screening of reaction selectivity," Rev. Sci. Instrum. **85**, 104101 (2014).
24. P. C. K. Vesborg, S.-i. In, J. L. Olsen, T. R. Henriksen, B. L. Abrams, Y. Hou, A. Kleiman-shwarsctein, O. Hansen, and I. Chorkendorff, "Quantitative measurements of photocatalytic CO-oxidation as a function of light intensity and wavelength over TiO_2 nanotube thin films in microreactors," J. Phys. Chem. C **1**, 11162–11168 (2010).
25. Z. Jusys, J. Kaiser, and R. J. Behm, "Electrooxidation of CO and H_2/CO mixtures on a carbon-supported Pt catalyst–a kinetic and mechanistic study by differential electrochemical mass spectrometry," Phys. Chem. Chem. Phys. **3**, 4650–4660 (2001).
26. H. Wang, Z. Jusys, R. J. Behm, and H. D. Abruna, "New insights into the mechanism and kinetics of adsorbed CO electrooxidation on platinum: Online mass spectrometry and kinetic Monte Carlo simulation studies," J. Phys. Chem. C **116**, 11040–11053 (2012).
27. M. J. Weaver, S.-C. Chang, L.-W. H. Leung, X. Jiang, M. Rubel, M. Szklarczyk, D. Zurawski, and A. Wieckowski, "Evaluation of absolute saturation coverages of carbon monoxide on ordered low-index platinum and rhodium electrodes," J. Electroanal. Chem. **327**, 247–260 (1992).
28. T. Biegler, D. A. J. Rand, and R. Woods, "Limiting oxygen coverage on platinized platinum; Relevance to determination of real platinum area by hydrogen adsorption," J. Electroanal. Chem. Interfacial Electrochem. **29**, 269–277 (1971).
29. R. W. Lindström, Y. E. Seidel, Z. Jusys, M. Gustavsson, B. Wickman, B. Kasemo, and R. J. Behm, "Electrocatalysis and transport effects on nanostructured Pt/GC electrodes," J. Electroanal. Chem. **644**(2), 90–102 (2010).
30. Y. Hori, K. Kikuchi, and S. Suzuki, "Production of CO and CH_4 in electrochemical reduction of CO_2 at metal electrodes in aqueous hydrogencarbonate solution," Chem. Lett. **1985**, 1695–1698.
31. K. P. Kuhl, T. Hatsukade, E. R. Cave, D. N. Abram, J. Kibsgaard, and T. F. Jaramillo, "Electrocatalytic conversion of carbon dioxide to methane and methanol on transition metal surfaces," J. Am. Chem. Soc. **136**, 14107 (2014).
32. C. W. Li, J. Ciston, and M. W. Kanan, "Electroreduction of carbon monoxide to liquid fuel on oxide-derived nanocrystalline copper," Nature **508**, 504 (2014).
33. K. J. P. Schouten, Y. Kwon, C. J. M. van der Ham, Z. Qin, and M. T. M. Koper, "A new mechanism for the selectivity to C_1 and C_2 species in the electrochemical reduction of carbon dioxide on copper electrodes," Chem. Sci. **2**(10), 1902 (2011).
34. K. Chan, C. Tsai, H. A. Hansen, and J. K. Nørskov, "Molybdenum sulfides and selenides as possible electrocatalysts for CO_2 reduction," ChemCatChem **6**, 1899 (2014).

Paper II

Real-time tracking of electrochemical desorption phenomena with sub-monolayer sensitivity [P2]
Daniel. B. Trimarco*, Soren B. Scott*, Anil H. Thilsted, Jesper Y. Pan, Thomas Pedersen, Ole Hansen, Ib Chorkendorff, and Peter C. K. Vesborg
In preparation
∗These authors contributed equally to this work.

Comment from author

This paper will be based on the content presented in chapters 2 and 3 if this thesis. The final publication will constitute Figures 2.1, 2.2, 2.4, 2.6, 2.7 and 2.8, as well as Figures 3.1, 3.2, 3.4 and Table 3.1 presented herein. The figures will be slightly reformatted, in order to fit a full paper, but the same content will be portrayed.

Real-time tracking of electrochemical desorption phenomena with sub-monolayer sensitivity

Daniel B. Trimarco[*1], Soren B. Scott[*1,2], Anil H. Thilsted[3], Jesper Y. Pan[4], Thomas Pedersen[4], Ole Hansen[4], Ib Chorkendorff[1], and Peter C. K. Vesborg [†1]

[1]Department of Physics, Technical University of Denmark, Fysikvej, Building 312, DK-2800 Kgs. Lyngby, Denmark
[2]Department of Chemistry, University of Copenhagen, Universitetsparken 5, DK-2100 København Ø, Denmark
[3]Spectro Inlets ApS, Fysikvej, Building 312, DK-2800 Kgs. Lyngby, Denmark
[4]Department of Micro- and Nanotechnology, Technical University of Denmark, Ørsteds Plads, Building 344, DK-2800 Kgs. Lyngby, Denmark

August 2017

Abstract

This paper presents a microchip based electrochemistry mass spectrometry (EC-MS) instrument for analyzing minute desorption events in real-time during electrochemistry measurements. A pressurized membrane chip is used to establish a two–step coupling between wet electrochemisty and the vacuum of a mass spectrometer (MS), allowing measurements of volatile reaction species with unprecedented sensitivity. This is done by matching the mass transport through the microchip to the anticipated analyte production rate under electrochemistry experiments, which helps suppress water evaporation and increase the analyte ionization probability in the mass spectrometer. Coupled with a versatile stagnant thin–layer electrochemistry cell, it is thus possible to measure desorption events down to ppm levels of a monolayer on a large range of different sample electrodes, while simultaneously maintaining control of the dissolved gas atmosphere surrounding the electrode. The capabilities of the instrument are demonstrated by analyzing the hydrogen evolution reaction (HER), oxygen evolution reaction (OER), CO oxidation reaction as well as CO stripping on a polycrystalline platinum electrode. By establishing a mass transport model describing the full transport of analyte species from the surface of an electrode and into the mass spectrometer, a direct coupling between surface phenomena and anticpicated mass spectrometer signals are demonstrated, which proves to match the experimental results to a high degree. Thereby a framework is established, which makes it possible to correlate minute desorption phenomena directly with Faradaic process analyzed in electrochemistry. This framework is expected to have large implications for future electrocatalysis studies by giving insight into fundamental electrochemical reaction mechanisms involving desorption of reaction products and intermediates. The established mass transport model is furthermore used to compare the present study with the conventional electrochemical mass spectrometry (DEMS) methodology in order to clarify advantages and disadvantages of the respective techniques.

---

[*]These authors contributed equally to this work.
[†]Corresponding author, email: peter.vesborg@fysik.dtu.dk.

Paper III

Dynamic effects of surface oxygen in CO electroreduction [P3]
Daniel. B. Trimarco*, Soren B. Scott*, Anders Bodin*, Alexander Bagger, Nicola Mazzanti, Jakob E. Sørensen, Thomas Pedersen, Ole Hansen, Ifan E. L. Stephens, Peter C. K. Vesborg, Jan Rossmeisl, and Ib Chorkendorff
In preparation
∗These authors contributed equally to this work.

Dynamic effects of surface oxygen in CO electroreduction

Soren B. Scott [*,1,2], **Daniel B. Trimarco** [*,1], **Anders Bodin** [*,1], Alexander Bagger[2],
Nicola Mazzanti[1], Jakob E. Sørensen[1], Thomas Pedersen[3], Ole Hansen[3], Ifan E. L. Stephens[1],
Peter C. K. Vesborg[1,3], Jan Rossmeisl[2], and Ib Chorkendorff [†,1,3]

[1]Department of Physics, Technical University of Denmark, Fysikvej, Building 312, DK-2800 Kgs. Lyngby,
Denmark
[2]Department of Chemistry, University of Copenhagen, Universitetsparken 5, DK-2100 København Ø, Denmark
[3]Department of Micro- and Nanotechnology, Technical University of Denmark, Ørsteds Plads, Building 344,
DK-2800 Kgs. Lyngby, Denmark

July 17, 2017

Sustainable fuel and chemical production by electroreduction of carbon monoxide with use of renewable electricity will likely contribute to reducing the net emissions of anthropogenic greenhouse gasses[1]. While significant progress has been made in catalyzing the two-electron reduction of carbon dioxide to carbon monoxide (CO)[2;3] or formic acid[3;4], at present the further electrochemical reduction of carbon monoxide to hydrocarbons suffers from poor energetic efficiency and selectivity on known catalysts[5;6].

Recently, it has been shown that copper surfaces effectively catalyze CO reduction to multi-carbon products when prepared from an oxidized precursor[7;8;9]. However, the reason for the increased activity is still debated[10;11;12;13], and elucidation of the reaction mechanism is often hindered by changes in the electrode surface under reaction conditions[14;12;13].

In this study we use mass-selected copper nanoparticles as a model catalyst for elucidating the effect of surface oxygen on the CO electroreduction reaction, demonstrating a highly active transient electrocatalytic pathway for methane production. Using a newly developed electrochemical mass spectrometry (EC-MS) setup with unprecedented sensitivity, we are able to observe the electrocatalytic activity of an oxidized surface before it is reduced during electrolysis. We find that, in contrast to reduced oxide-derived copper surfaces, adsorbed oxygen on copper activates an electrocatalytic pathway towards the single-carbon products without affecting two-carbon product formation.

Based on density functional theory (DFT) calculations, we propose that the dynamic methane production can be attributed to surface oxygen stabilizing the ∗CHO reaction intermediate on under-coordinated sites with respect to adsorbed CO.

In addition to providing mechanistic insight, this result suggests a new design paradigm for improving activity and tuning selectivity of electrocatalysts by stabilizing or regenerating metastable active sites.

Our experiments were conducted in the EC-MS setup sketched in Figure 1a, where the sample is incorporated in a polychlorotrifluoroethylene (PCTFE) EC-MS cell and separated from the mass spectrometer by means of a microfabricated membrane chip (Figure 1a, left inset), allowing a controlled transfer of reaction products from the electrolyte to the vacuum. The distance between the sample and the membrane is defined by a 100 μm Teflon spacer forming a thin layer of electrolyte (0.5 M

---

*These authors contributed equally to this work.
†Corresponding author. Email: ibchork@fysik.dtu.dk.

potassium carbonate, pH=12). During operation, the electrolyte is kept stagnant and is continuously saturated by reactant gas from the microchip membrane. The working volume can be flushed or purged with fresh electrolyte or gas respectively (see SI for more details on the EC-MS system).

The samples were prepared by depositing mass-selected copper nanoparticles with a diameter of 4.8 ± 0.2 nm onto a 5 mm glassy carbon disc with 5% projected surface coverage, corresponding to a total mass loading of 24 ng (Figure 1a, right inset). Operating at these low loadings minimizes particle-particle interaction and mass transport phenomena.

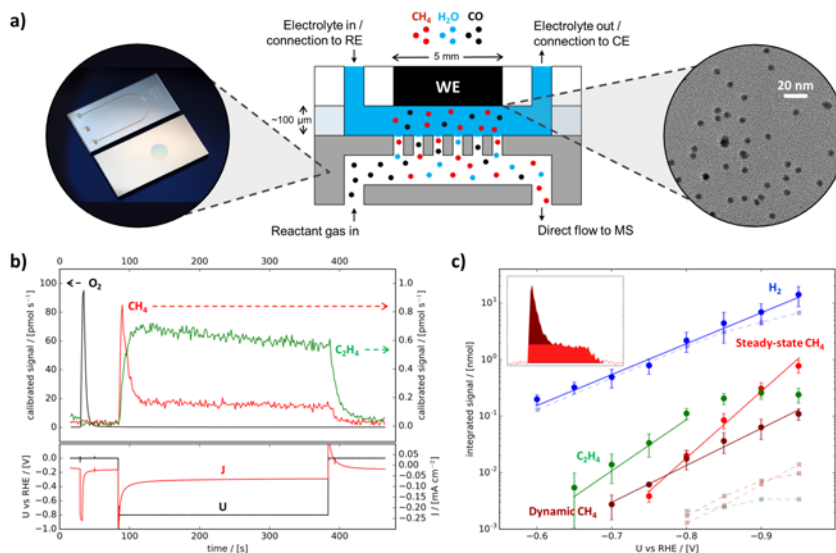Our experiments were based on constant-potential electrolysis (chronoamperometry) as shown in

Figure 1: Experimental setup and demonstration of the transient methane production phenomenon. a, Schematic of the experimental setup. Left inset: Membrane chip used to interface the electrochemical environment with the vacuum of the mass spectrometer (not drawn to scale). Right inset: TEM image of Cu nanoparticles as deposited onto a glassy carbon substrate as the working electrode (WE). The WE and the membrane chip are separated by 100 μm stagnant thin film of electrolyte (the working volume). **b**, EC-MS plot of a typical constant-potential electrolysis experiment showing the calibrated MS signals for oxygen (O_2, black) methane (CH_4, red), and ethylene (C_2H_4, green) during a five minute constant-potential step at a working potential of -0.80 V vs RHE preceded by a five second flush of aerated electrolyte (exchanging working volume electrolyte more than 10 times) while at a resting potential of 0 V vs RHE. The potential (black) and electrical current density (red) are shown below on the same time axis. **c**, Integrated MS signals during one minute constant-potential steps plotted as a function of working potential as a Tafel plot. The aerated electrolyte was flushed for five seconds prior to each step, and the resting potential between steps was 0 V vs RHE. Datapoints and error bars represent the mean and standard deviation, respectively, of measurements on four separate samples. The methane signal is divided into dynamic (dark red) and steady-state (light red) contributions as indicated in the inset. H_2, O_2, CH_4, and C_2H_4 were measured at m/z = 2, 32, 15, and 26, respectively. For details on quantification, see SI.

Figure 1b, with the top panel of showing the calibrated MS signals for oxygen (O_2), methane (CH_4), and ethylene (C_2H_4), respectively (quantified as described in SI), and the bottom panel showing the electrical potential and current. We refer to this type of plot as an EC-MS plot.

To investigate the influence of oxygen on CO electroreduction activity, we expose the sample to dioxygen (O_2) by flushing the working volume with aerated electrolyte for five seconds (exchanging the electrolyte more than 10 times) while holding the sample at a *resting potential* 0 V vs RHE ($t = 40$ s). The cathodic current during the flush is attributed to oxygen reduction. A *working potential* of -0.8 V vs RHE is then applied at $t = 85$ s for five minutes.

At the onset of the working potential step we observe a surprising phenomenon: a high initial production of CH_4 followed by a decline to steady state. Interestingly, this is only observed for CH_4, while the H_2 and C_2H_4 production rates remain steady during the five minutes of electrolysis, indicating that the phenomenon only effects the single-carbon (C1) electrocatalytic pathway.

In order to characterize this transient phenomenon, we separate the integrated CH_4 signal into two parts as indicated in the inset to Figure 1c: (1) the dynamic initial burst of CH_4 activity, and (2) CH_4 produced at the subsequent steady-state level. The integrated MS signals of dynamic CH_4, steady-state CH_4, C_2H_4, and H_2, respectively, from one-minute constant-potential steps are shown in Figure 1c as a function of working potential. Prior to each working potential step, the electrode was exposed to a five second flush of aerated electrolyte at a constant resting potential of 0 V vs RHE, as in the experiment shown in Figure 1b. Error bars represent mean and standard deviation between measurements on four separate samples. Control experiments on blank substrates show minute levels of hydrocarbon production (see SI for more detail), which we attribute to trace impurities [15], but similar levels of hydrogen production, which also indicates that the majority of HER activity is due to the glassy carbon substrate.

When quantified in this way, it is clear that steady-state CH_4 and dynamic CH_4 have distinct potential dependencies. The Tafel slope for steady-state CH_4 is 91 mV/decade, while for dynamic CH_4 it is 151 mV/decade. Ethylene has a Tafel slope of 122 mV/decade from -0.65 V to -0.80 V vs RHE and then tapers off. These Tafel slopes, and the deviation towards lower C_2H_4 activity at higher overpotentials, are in good agreement with previous reports on CO_2 electroreduction on polycrystalline copper [16;17].

To verify that we cannot activate the dynamic CH_4 production without O_2 in the electrolyte, Ar (Figure 2a) or O_2 (Figure 2b) was dosed via the reactant gas through the membrane of the chip while holding the sample at 0 V vs RHE prior to a two minute constant-potential step at -0.90 V vs RHE. Dynamic methane production is activated when O_2 is dosed but not in the Ar control experiment. Production of steady-state CH_4, C_2H_4, and H_2 all remain unaffected.

Previous EC-MS studies of CO electroreduction on Cu utilizing potential scans (cyclic voltammetry) have not observed similar dynamic phenomena, even where the sample has seen an oxidizing environment prior to experiments [8;18]. Likewise, potential scans on our EC-MS system do not show any sign of dynamic CH_4, as seen in Figure 2c, which shows an EC-MS plot of a potential scan at 5 mV/s. This is likely due to the sample getting reduced on the cathodic scan before any hydrocarbons are produced.

To probe the conditions necessary to activate the catalyst for dynamic CH_4 production, we varied the resting potential at which O_2 was introduced, as shown in Figure 2d. Here, the integrated MS signals during one-minute constant-potential steps at -0.85 V vs RHE are plotted against the preceding resting potential, during which O_2 was introduced by a five-second flush of aerated electrolyte. This experiment demonstrates that dynamic CH_4 is only activated when the potential during O_2 exposure is anodic of -0.20 V vs RHE. The dynamic CH_4 production then increases as function of resting potential until it reaches a plateau around +0.20 V vs RHE, suggesting that the relevant surface sites have become saturated. A similar saturation can likewise be obtained by varying the duration of O_2 exposure without changing the resting potential (see SI for more details).

Interestingly, when O_2 was introduced at potentials anodic of 0 V vs RHE, the steady-state activity was also increased, indicating that higher degrees of oxidation influence only the steady-state activity of CH_4 and C_2H_4. Without O_2 in the electrolyte a similar increase in steady-state CO electroreduction activity can be obtained at potentials anodic of +0.5 V vs RHE, but without activating the dynamic

CH_4 production (see SI for more details). This steady-state increase in CO electroreduction activity is consistent with observations on oxide-derived Cu electrodes.[7;9;19]

The observation that dynamic CH_4 production is activated by O_2 exposure up to a saturation point, but not activated by electrochemical oxidation, suggests that the increased activity is due to metastable oxidation of specific active sites on the Cu surface. The surface sites relevant for this study are illustrated by Figure 3a which shows a Wulff construction of a Cu NP approximately 5 nm in diameter. Surface atoms are color-coded according to their coordination number (CN).

Prior DFT studies have investigated the rate- and potential- limiting elementary steps in CO_2 and CO electroreduction on various reduced copper surface sites.[20] On terraced sites (CN = 8 or 9), the binding energy of ∗CO is very small ($|E(∗CO)| < 0.1$ eV), and CO adsorption is rate-limiting. Thus we do not expect the flat surfaces to contribute significantly to catalyzing the reaction. On undercoordinated sites, the first proton-electron transfer to ∗CO, forming ∗CHO, is potential-limiting for CO reduction to methane. The limiting overpotential is larger for kinks (CN = 6) than for steps (CN = 7), as the higher reactivity of kink sites lowers the free energy of ∗CO (double-bonded to the surface) by a greater amount than that of ∗CHO (single-bonded). Our calculations, shown as free
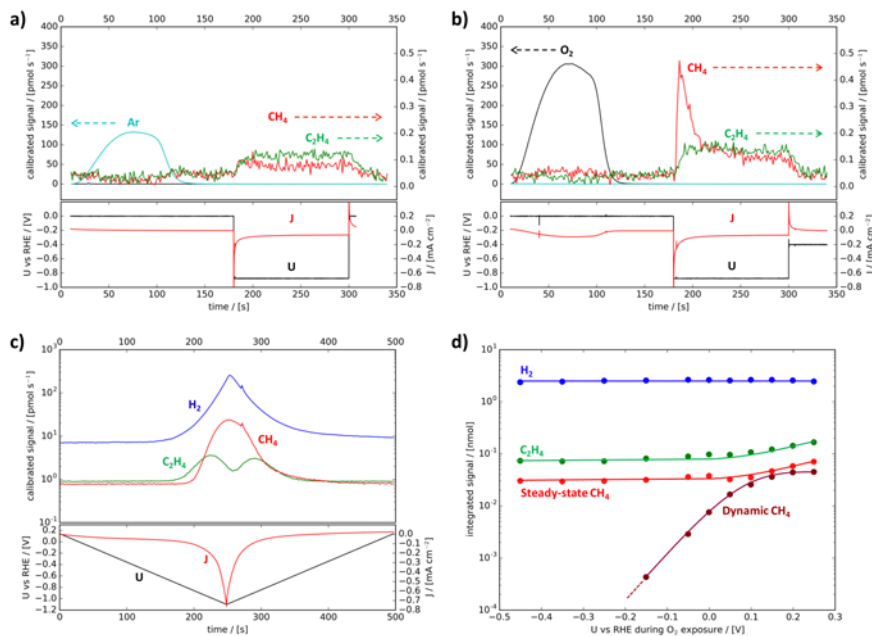

Figure 2: Influence of oxygen on dynamic methane production. a-b, The effect of oxygen demonstrated by two constant-potential electrolysis experiments at a working potential of -0.90 V vs RHE. Gaseous Ar (a) or O_2 (b) was dosed through the microchip membrane while holding the resting potential at 0 V vs RHE. The experiments are plotted as EC-MS plots with the top panel showing the mass spectrometer signals for argon (Ar, cyan), oxygen (O_2, black), methane (CH_4, red) and ethylene (C_2H_4, green) and the bottom panel showing the electrical potential (black) and geometric current density (red). **c**, Potential scan as an EC-MS plot. **d**, The integrated mass spectrometry signal of steady-state methane (CH_4, red), dynamic methane (CH_4, dark red) and steady state ethylene (C_2H_4, green) during a one minute constant-potential steps at -0.85 V vs RHE as function of the resting potential during oxygen exposure immediately preceding the constant-potential step.

energy diagrams for the first steps of CO reduction at step and kink sites in the blue traces ('without oxygen') of Figures 3c and 3d, respectively, reproduce this result. An electrical potential of -0.8 V vs RHE, corresponding to the experimental condition in Figure 1, has been implemented for these calculations as an adjustment to the reference state of hydrogen, i.e. by the computational hydrogen electrode (CHE).

Our calculations predict that ∗CO at step and kink sites is destabilized by adjacent surface-adsorbed atomic oxygen (surface oxygen, ∗O). While ∗CHO on step sites is destabilized by a similar amount, leaving the limiting potential unchanged, ∗CHO on kink sites is stabilized with respect to ∗CO by surface oxygen. This effect was observed as a general trend independent of the exact adsorption site used for ∗O. These results are shown as free energy diagrams in the red traces ('with oxygen') of Figures 3c and 3d, respectively, where the exact choice of ∗O site, indicated in the insets, is based on stability with respect to ∗OH. In summary, we expect that the effect of surface oxygen is to increase the rate of CO electroreduction to CH_4 at sites which normally bind CO too strongly.

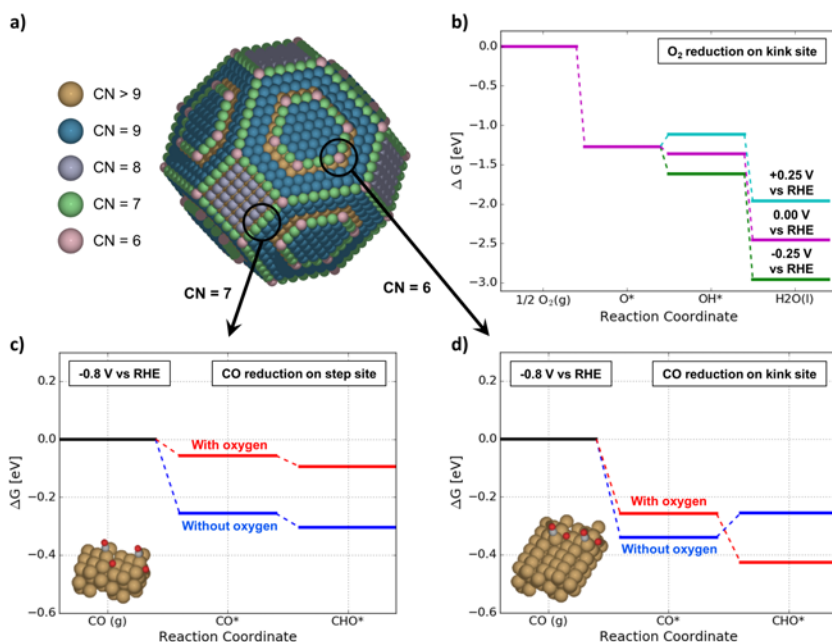We attribute the transient nature of the pathway to the fact that the surface oxygen is only

Figure 3: Atomic scale modeling of the influence of oxygen on the catalytic pathway towards methane. a, Wulff construction of a Cu particle approximately 5 nm in diameter, illustrating the coordination numbers of the surface atoms. b, Free energy diagram for the oxygen reduction reaction on the kink site at three different potentials. At +0.25 V vs. RHE the oxygen is stable, whereas more negative potentials cause a further reduction to *OH. Kinetic barriers between reaction intermediates are not included, and thus the adsorbed oxygen could be metastable at e.g. 0 V vs. RHE, even though the reaction to *OH is slightly downhill in energy. c-d, Free energy diagrams calculated with density functional theory for the potential dependent steps for CO electroreduction to CH_4 for b the step and c the kink site, without (blue) and with (red) an adsorbed oxygen atom at the most stable nearby site. In each case, the unit cell used for the calculation with the adsorbed oxygen is shown as an inset. Both diagrams are shown with an applied potential of -0.8 V vs RHE, similar to the experiment shown in Figure 1b.

short-lived at CO-electroreduction potentials before being reduced to water. At resting potentials, however, the oxygen can be stable as shown in figure 3b, which displays a free energy diagram of the oxygen reduction reaction on the kink site at three different resting potentials. At +0.25 V vs. RHE the oxygen is stable, whereas more negative potentials cause a further reduction to *OH. It should, however, be noted that kinetic barriers between reaction intermediates are not included in the calculations. If there is such a kinetic barrier for ∗O reduction to ∗HO at e.g. 0 V vs. RHE, then ∗O could be a metastable state at the O_2 dosing potential, and be present transiently even at CO reduction potentials. The duration of dynamic methane activity would then correspond to the lifetime of this metastable active site. Fitting of the experimentally measured CH_4 signal with a model of CH_4 diffusion and evaporation in the EC-MS system (SI) indicates that the lifetime of the active site is on the order of 1 second at -0.85 V vs RHE. During this lifetime, an active site turns over between 2 and 20 CH_4 molecules, where the uncertainty lies primarily in estimating the number of active sites (SI).

The decoupled dynamic behavior of CH_4 and C_2H_4 production is consistent with the understanding that C1 and C2 pathways in CO reduction have distinct rate-limiting steps[5;21]. However, our results stand in contrast to earlier observations of oxidized Cu activating a C2 pathway, leading to increased C_2H_4 formation[9;12]. The difference is that our time-resolved product detection and constant-potential experiment methods enable us to isolate the effect of surface oxygen, which is reduced quickly and affects only the C1 CO electroreduction pathway. Also note that our results are obtained on nanoparticles which have a high concentration of undercoordinated kink sites as compared to polycrystalline surfaces.

While EC-MS has successfully been used to determine reaction selectivity in lithium batteries[22], investigating the catalytic mechanism for oxygen evolution reaction[23], and study single crystals for CO_2 electroreduction[24], this is, to the best of our knowledge, the first time EC-MS has been used to study an intrinsically transient phenomenon. The newly developed EC-MS system used in our study can potentially open new research fields, such as studying the OER activity of metallic transition metals or the intrinsic activity of catalysts that become poisoned by intermediates. On the industrial level, mastering such transient phenomena could make it possible to steer electrocatalytic processes to produce products beyond the reach of steady electrolysis.

Methods summary

Electrochemical mass spectrometry: Our EC-MS setup uses a micro-fabricated membrane chip (right inset of Figure 1a) to make a liquid-vacuum junction between electrolyte and mass spectrometer, allowing volatile electrochemical products to be detected while simultaneously dosing reactant gas through the membrane[25]. A glassy carbon disc (Ø 5 mm) was mounted as working electrode (WE) in an electrochemical cell which enables electrolyte flow and connections to external counter and reference electrodes, thus establishing a 3-electrode setup. The electrochemical cell was mounted on top of the membrane chip with a 100 μm Teflon spacer defining the distance between WE and membrane chip. All experiments were carried out in a 0.5 M potassium carbonate buffer with pH=12. See SI for further details.

Sample synthesis and characterization: Mass-selected copper nanoparticles with a diameter of $d = 4.8 \pm 0.2$nm were used as a model catalyst. The nanoparticles were synthesized in an ultra-high vacuum nanoparticle source (Nanobeam 2011, Birmingham Instruments Inc.) by magnetron sputtering of a copper target and gas-phase nanoparticle aggregation in 0.4 mbar of He and Ar, followed by super-sonic expansion through an aperture into a differentially pumped UHV region where the particles do not grow further. Subsequently, particles with $m = 350,000$ amu were selected in a lateral time-of-flight mass filter with mass resolution of m/Δm=20[26]. The particles were deposited onto sputter-cleaned glassy carbon discs with 5 % projected surface coverage, corresponding to a total mass loading of 24 ng of Cu on each sample. Cleanliness of the samples was ensured by X-ray photoelectron spectroscopy (SPECS XR 50 X-ray gun coupled to Omicron NanoSAM 7 channel energy analyzer) and ion scattering spectroscopy (Omicron ISE100 ion gun) before and after deposition of nanoparticles; the spectroscopies were performed in a UHV system coupled to the nanoparticle source (Scienta Omicron), thus avoiding air exposure before the sample was taken out for EC-MS measurements. The nanoparticle size-distribution was found from TEM images acquired in a FEI Tecnai T20 G2 transmission electron microscope, analyzed in the software ImageJ. A small fraction of particles are larger than $d = 4.8 \pm 0.2$ nm, due to particles landing on top of each other, or particles with double mass which cannot be discriminated from the desired mass in the mass filter[27]. Spectroscopy and microscopy is presented in supplementary information.

Substrate cleaning procedure: All glassy carbon substrates were cleaning using the following procedure: 1) Rinsing in ultrapure water 2) Cleaning in 65% suprapure nitric acid for one hour, then rinsing in ultrapure water 3) Polishing with $1/4 \mu$m diamond paste 4) Sonicating two times for 10 minutes, first in ethanol and then in ultrapure water 5) Repeating the acid treatment (step 2) and 6) Sonicating two times in ultrapure water for 10 minutes. After cleaning, 3d and 5d metal impurities were below the detection limit of XPS, but the ISS measurements still showed traced amounts, as it is an extremely sensitive technique (see supplementary information).

Glassware and EC cell cleaning procedure: Before each experiment, all components of the setup that were exposed to electrolyte during experiments were cleaned by leaving them overnight in 3:1 solution of 98% sulfuric acid and 30% hydrogen peroxide (Piranha solution). This effectively removed organic impurities and non-precious metals. All components were then thoroughly rinsed five times with water to remove the solvent and any residual contamination.

Electrolyte preparation: All experiments were performed in a 0.5 M potassium carbonate buffer titrated to pH 12 with KOH. The electrolyte was prepared by saturating 200 ml of 1.0 M KOH with CO_2, to a pH of 7.8. This was then tritrated to pH 12 using 213.5 ml 1.0 M KOH.

Density functional theory: The two DFT models were created in ASE[28]. A 211 stepped slab with a (3,3,3) unit cell and a kink model by removing atoms from a larger 211 slab with unit cell size (3,6,3). In both structures the two lower atomic layers where kept fixed. For the electronic structure calculations the projector-augmented wave method was used together with the revised Perdew-Burke-Ernzerhof (RPBE)[29] functional in the GPAW software[30;31]. For all calculations a 0.17 grid spacing were applied, the forces were relaxed down below 0.05 eV/Å and a (4 x 4 x 1) and (4 x 2 x 1) k-point sampling were used for the step and kink structure, respectively. The hydrogen electrode was employed[32] to calculate the free energy diagrams. For zero point, entropy and heat capacity we apply values from reference[33] and as intermediate water corrections we use 0.25 eV for R-OH intermediates and 0.1 eV for R=O intermediate similar to the results of A. Petersson[34].

Author Contributions: S. B. Scott, D. B. Trimarco, A. Bodin, N. Mazzanti, and J. E. Sørensen performed the experiments with supervision from O. Hansen, I. L. Stephens, P. C. K. Vesborg, and I. Chorkendorff; A. Bagger did the DFT modelling with supervision from J. Rossmeisl; S. B. Scott performed analysis and modelling of experimental data; D. B. Trimarco, P. C. K. Vesborg, S. B. Scott, and T. Pedersen developed the EC-MS technique with supervision from O. Hansen and I. Chorkendorff; S. B. Scott, D. B. Trimarco, and A. Bodin wrote the paper with contributions from A. Bagger and discussion with all authors.

References

[1] Steven Chu, Yi Cui, and Nian Liu. The path towards sustainable energy. *Nature Materials*, 16(1):16–22, 2016.

[2] Christina W. Li and Matthew W. Kanan. CO2 reduction at low overpotential on Cu electrodes resulting from the reduction of thick Cu2O films. *Journal of the American Chemical Society*, 134(17):7231–7234, 2012.

[3] Min Liu, Yuanjie Pang, Bo Zhang, Phil De Luna, Oleksandr Voznyy, Jixian Xu, Xueli Zheng, Cao Thang Dinh, Fengjia Fan, Changhong Cao, F. Pelayo García de Arquer, Tina Saberi Safaei, Adam Mepham, Anna Klinkova, Eugenia Kumacheva, Tobin Filleter, David Sinton, Shana O. Kelley, and Edward H. Sargent. Enhanced electrocatalytic CO2 reduction via field-induced reagent concentration. *Nature*, 537(7620):382–386, 2016.

[4] S Gao, Y Lin, X Jiao, Y Sun, Q Luo, W Zhang, D Li, J Yang, and Y Xie. Partially oxidized atomic cobalt layers for carbon dioxide electroreduction to liquid fuel. *Nature*, 529(7584):68–71, 2016.

[5] Ruud Kortlever, Jing Shen, Klaas Jan P Schouten, Federico Calle-Vallejo, and Marc T M Koper. Catalysts and Reaction Pathways for the Electrochemical Reduction of Carbon Dioxide. *The Journal of Physical Chemistry Letters*, 6(20):4073–4082, 2015.

[6] Zarko P. Jovanov, Heine A. Hansen, Ana Sofia Varela, Paolo Malacrida, Andrew A. Peterson, Jens K. Nørskov, Ifan E L Stephens, and Ib Chorkendorff. Opportunities and challenges in the electrocatalysis of CO2 and CO reduction using bifunctional surfaces: A theoretical and experimental study of Au-Cd alloys. *Journal of Catalysis*, 343(April):215–231, 2016.

[7] Christina W Li, Jim Ciston, and Matthew W Kanan. Electroreduction of carbon monoxide to liquid fuel on oxide-derived nanocrystalline copper. *Nature*, 508(7497):504–507, 2014.

[8] F. Sloan Roberts, Kendra P. Kuhl, and Anders Nilsson. High selectivity for ethylene from carbon dioxide reduction over copper nanocube electrocatalysts. *Angewandte Chemie - International Edition*, 54(17):5179–5182, 2015.

[9] Chung Shou Chen, Albertus D. Handoko, Jane Hui Wan, Liang Ma, Dan Ren, and Boon Siang Yeo. Stable and selective electrochemical reduction of carbon dioxide to ethylene on copper mesocrystals. *Catal. Sci. Technol.*, 5(1):161–168, 2015.

[10] Arnau Verdaguer-Casadevall, Christina W. Li, Tobias P. Johansson, Soren B. Scott, Joseph T. Mckeown, Mukul Kumar, Ifan E L Stephens, Matthew W. Kanan, Ib Chorkendor, and Ib Chorkendorff. Probing the active surface sites for CO reduction on oxide-derived copper electrocatalysts. *Journal of the American Chemical Society*, 137(31):9808–9811, 2015.

[11] Ana Sofia Varela, Matthias Kroschel, Tobias Reier, and Peter Strasser. Controlling the selectivity of CO2 electroreduction on copper: The effect of the electrolyte concentration and the importance of the local pH. *Catalysis Today*, 260:8–13, 2016.

[12] Hemma Mistry, Ana Sofia Varela, Cecile S. Bonifacio, Ioannis Zegkinoglou, Ilya Sinev, Yong-wook Choi, Kim Kisslinger, Eric A. Stach, Judith C. Yang, Peter Strasser, and Beatriz Roldan Cuenya. Highly selective plasma-activated copper catalysts for carbon dioxide reduction to ethylene. *Nature Communications*, 7:1–8, 2016.

[13] Andre André Eilert, Filippo Cavalca, F Sloan Roberts, Ju Jürg Osterwalder, Chang Liu, Ethan J Crumlin, Hirohito Ogasawara, Daniel Friebel, Lars G M Pettersson, Marco Favaro, Ethan J Crumlin, Hirohito Ogasawara, Daniel Friebel, Lars G M Pettersson, and Anders Nilsson. Subsurface Oxygen in Oxide-Derived Copper Electrocatalysts for Carbon Dioxide Reduction. *Journal of Physical Chemistry Letters*, (8):285–290, 2017.

[14] Dahee Kim, Seunghwa Lee, Joey D. Ocon, Beomgyun Jeong, Jaeyoung Kwang Lee, Kwang Lee, and Jaeyoung Kwang Lee. Insights into autonomously formed oxygen-evacuated Cu2O electrode for the selective production of C2H4 from CO2. *Phys. Chem. Chem. Phys.*, 17(2):1–9, 2015.

[15] Yanwei Lum, Youngkook Kwon, Peter Lobaccaro, Le Chen, Ezra Lee Clark, Alexis T. Bell, and Joel W. Ager. Trace Levels of Copper in Carbon Materials Show Significant Electrochemical CO2 Reduction Activity. *ACS Catalysis*, 6(1):202–209, 2016.

[16] Yoshio Hori, Akira Murata, and Ryutaro Takahashi. Formation of hydrocarbons in the electrochemical reduction of carbon dioxide at a copper electrode in aqueous solution. *Journal of the Chemical Society, Faraday Transactions 1: Physical Chemistry in Condensed Phases*, 85(8):2309, 1989.

[17] Kendra P. Kuhl, Etosha R. Cave, David N. Abram, and Thomas F. Jaramillo. New insights into the electrochemical reduction of carbon dioxide on metallic copper surfaces. *Energy & Environmental Science*, 5(2012):7050–7059, 2012.

[18] Klaas Jan P Schouten, Zisheng Qin, Elena Pérez Gallent, and Marc T M Koper. Two pathways for the formation of ethylene in CO reduction on single-crystal copper electrodes. *Journal of the American Chemical Society*, 134(24):9864–9867, 2012.

[19] F. Sloan Roberts, Kendra P. Kuhl, and Anders Nilsson. Electroreduction of Carbon Monoxide Over a Copper Nanocube Catalyst: Surface Structure and pH Dependence on Selectivity. *ChemCatChem*, pages 1119–1124, 2016.

[20] Chuan Shi, Heine a Hansen, Adam C Lausche, and Jens K Nørskov. Trends in electrochemical CO2 reduction activity for open and close-packed metal surfaces. *Physical Chemistry Chemical Physics*, 16(10):4720–4727, 2014.

[21] Joseph H Montoya, Chuan Shi, Karen Chan, and Jens K Nørskov. Theoretical insights into a co dimerization mechanism in CO_2 electroreduction. *The Journal of Physical Chemistry Letters*, pages 2032–2037, 2015.

[22] Bryan D. McCloskey, Rouven Scheffler, Angela Speidel, Girish Girishkumar, and Alan C. Luntz. On the mechanism of nonaqueous li–o2 electrochemistry on c and its kinetic overpotentials: Some implications for li–air batteries. *The Journal of Physical Chemistry C*, 116(45):23897–23905, 2012.

[23] Alexis Grimaud, Oscar Diaz-morales, Binghong Han, Wesley T Hong, Yueh-lin Lee, Livia Giordano, Kelsey A Stoerzinger, Marc T M Koper, and Yang Shao-Horn. Activating lattice oxygen redox reactions in metal oxides to catalyse oxygen evolution. *Nat. Chem.*, 9(5):457–465, 2017.

[24] Klaas Jan P Schouten, Elena Perez Gallent, and Marc T M Koper. The influence of pH on the reduction of CO and CO2 to hydrocarbons on copper electrodes. *Journal of Electroanalytical Chemistry*, 716:53–57, 2013.

[25] Daniel B. Trimarco, Thomas Pedersen, Ole Hansen, Ib Chorkendorff, and Peter C K Vesborg. Fast and sensitive method for detecting volatile species in liquids. *Review of Scientific Instruments*, 86(7), 2015.

[26] B von Issendorff and R E Palmer. A new high transmission infinite range mass selector for cluster and nanoparticle beams. *Rev. Sci. Instrum.*, 70(4497-4501), 1999.

[27] Hernandez-Fernandez P Deiana D Strebel C E McCarthy D N Bodin A Malacrida Paolo Stephens Ifan Chorkendorff I Masini F. Exploring the phase space of time of flight mass selected PtxY nanoparticles. *Phys. Chem. Chem. Phys*, 16(48)(26506-26513), 2014.

[28] Sune R. Bahn and Karsten W. Jacobsen. An object-oriented scripting interface to a legacy electronic structure code. *Computing in Science and Engineering*, 4(3):56–66, 2002.

[29] B. Hammer, L. Hansen, and J. Nørskov. Improved adsorption energetics within density-functional theory using revised Perdew-Burke-Ernzerhof functionals. *Physical Review B*, 59(11):7413–7421, 1999.

[30] J. J. Mortensen, L. B. Hansen, and K. W. Jacobsen. Real-space grid implementation of the projector augmented wave method. *Physical Review B - Condensed Matter and Materials Physics*, 71(3):1–11, 2005.

[31] J Enkovaara, C Rostgaard, J J Mortensen, J Chen, M Dułak, L Ferrighi, J Gavnholt, C Glinsvad, V Haikola, H a Hansen, H H Kristoffersen, M Kuisma, a H Larsen, L Lehtovaara, M Ljungberg, O Lopez-Acevedo, P G Moses, J Ojanen, T Olsen, V Petzold, N a Romero, J Stausholm-Møller, M Strange, G a Tritsaris, M Vanin, M Walter, B Hammer, H Häkkinen, G K H Madsen, R M Nieminen, J K Nørskov, M Puska, T T Rantala, J Schiøtz, K S Thygesen, and K W Jacobsen. Electronic structure calculations with GPAW: a real-space implementation of the projector augmented-wave method. *Journal of physics. Condensed matter : an Institute of Physics journal*, 22(25):253202, 2010.

[32] J K Nørskov, J Rossmeisl, A Logadottir, L Lindqvist, J R Kitchin, T Bligaard, and H Jónsson. Origin of the overpotential for oxygen reduction at a fuel-cell cathode. *Journal of Physical Chemistry B*, 108(46):17886–17892, 2004.

[33] Karen Chan, Charlie Tsai, Heine A. Hansen, and Jens K. Nørskov. Molybdenum sulfides and selenides as possible electrocatalysts for CO 2 reduction. *ChemCatChem*, 6(7):1899–1905, 2014.

[34] Andrew A. Peterson, Frank Abild-Pedersen, Felix Studt, Jan Rossmeisl, and Jens K. Nørskov. How copper catalyzes the electroreduction of carbon dioxide into hydrocarbon fuels. *Energy & Environmental Science*, 3(9):1311, 2010.

Paper IV

Anodic H$_2$ desorption from polycrystaline copper [P4]
Soren B. Scott, <u>Daniel. B. Trimarco</u>, Nikolaj R. Knøsgaard, Albert K. Engstfeld, Jan Rossmeisl, Peter C. K. Vesborg and Ib Chorkendorff
In preparation

Comment from author

This paper will be based on the content presented in chapter 6 if this thesis. The final publication will constitute Figures 6.1 and 6.2 presented herein.

Anodic H$_2$ desorption from polycrystaline copper

Soren B. Scott[1,2], Daniel B. Trimarco[1], Nikolaj R. Knøsgaard[1], Albert K. Engstfeld[1], Jan Rossmeisl[2], Peter C. K. Vesborg[1], and Ib Chorkendorff [*1]

[1]Department of Physics, Technical University of Denmark, Fysikvej, Building 312, DK-2800 Kgs. Lyngby, Denmark
[2]Department of Chemistry, University of Copenhagen, Universitetsparken 5, DK-2100 København Ø, Denmark

August 2017

Abstract

This paper presents the novel observation of a molecular hydrogen desorption phenomenon occurring on polycrystalline copper at electrical potentials anodic of the reversible hydrogen potential (RHE). When scanning a copper electrode to potentials anodic RHE, approximately 50 pmol of molecular hydrogen desorbes from the surface, corresponding to $\sim 10\,\%$ of monolayer. This anodic hydrogen desorption happens only after initially exposing the electrode to cathodic potentials, close to the onset of the hydrogen evolution reaction (HER), which causes the surface decorate with adsorbed hydrogen species. This observation was made possible by utilizing a newly developed microchip based electrochemistry mass spectrometry (EC-MS) instrument, designed to capture minute desorptions of volatile electrochemical reaction species in real-time. The anodic hydrogen desorption happens cathodic of any copper oxidation or reduction phenomona and the total amount of desorbed hydrogen remain unchanged at ~ 50 pmol regardless of scan rates or priming conditions. The phenomenon is proven to be electrochemically triggered, by locking the pre-adsorbed hydrogen in place at intermediate potentials for several minutes, after which ~ 50 pmol is again released. By gradually varying cathodic and anodic potentials limits and thereby isolating the anodic desorption phenomenon from ordinary HER, the hydrogen ad- and desorbtion potentials are experimentally probed to be $-0.125\,\mathrm{V}$ vs RHE and $0.05\,\mathrm{V}$ vs RHE, respectively. These ad- and desorption potentials are furthermore proven invariant with respect to pH change on an RHE scale. Ad- and desorbtion energies are calculated using density functional theory (DFT), which, consistently with the experimental observations, suggest that surface adsorbed *H species are replaced by *OH at potentials anodic of $+0.05\,\mathrm{V}$ vs RHE, where *OH adsorbtion becomes energetically more favorable. This study is believed to be the first experimental demonstration of ad- and desorbtion energies for hydrogen on copper under electrochemical conditions.

---

*Corresponding author, email: ibchork@fysik.dtu.dk.

1

Appended patents

Patent I

A device for extracting volatile species from a liquid
Daniel. B. Trimarco, Peter C. K. Vesborg, Thomas Pedersen, Ole Hansen, and
Ib Chorkendorff
Patent pending, publication no. WO 2016075208 A1
(priority date: Nov 14 2014, publication date: May 19 2016)

1

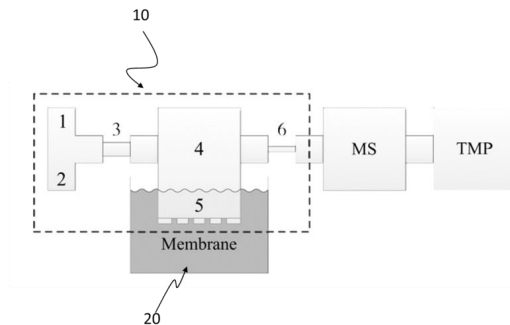A DEVICE FOR EXTRACTING VOLATILE SPECIES FROM A LIQUID

ABSTRACT

5 The invention relates to a device (10) for extracting volatile species from a liquid
(20) connected to an inlet of an analysis instrument, such as a mass spectrometer
(MS). The device has a chamber (4), a membrane (5) forming a barrier for the
liquid at zero differential pressure between the inside and the outside of the
chamber, and allowing passage of the volatile species at zero differential pressure
10 between the inside and the outside of the chamber. The device has an inlet
capillary channel (3) to feed in a carrier gas and prevent back-diffusion from the
chamber, and an outlet capillary channel (6) which provides a significant pressure
reduction, e.g. from atmospheric pressure in the chamber (4) to near-vacuum
suitable for an MS. The invention combines the best of two worlds, i.e. the fast
15 time-response of a DEMS system and the high sensitivity of a MIMS system, since
a differential pumping stage is not needed.
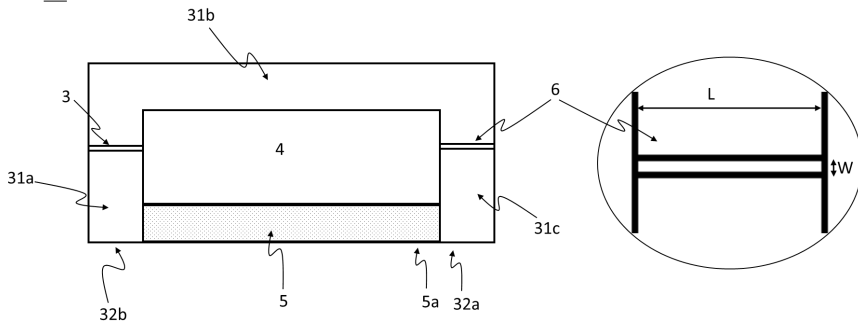
2

CLAIMS

1. A device (10) for extracting volatile species from an associated liquid (20) and being suitable for connection to an inlet of an associated analysis
5   instrument, such as a mass spectrometer (MS), the device comprising:
    a. a chamber (4),
    b. a membrane (5), which:
        i. connects the inside of the chamber with the outside of the chamber,
10   ii. forms a barrier for the liquid at zero, or near-zero, differential pressure between the inside and the outside of the chamber,
        iii. allows passage of the volatile species at zero, or near-zero, differential pressure between the inside and the outside of the chamber,
15   c. an inlet capillary channel (3) which connects the inside of the chamber with the outside of the chamber, the inlet capillary channel being arranged for intake of a carrier gas, and
        d. an outlet capillary channel (6) which connects the inside of the chamber with the outside of the chamber, the outlet capillary
20   channel being arranged for connection with said inlet of the associated analysis instrument,
    wherein, upon immersion of the device into the liquid, the device allows the liquid (20) to come into contact with the membrane (5).

25 2. A device according to any one of the preceding claims, wherein a substantially plane side (32a, 32b) of the device comprises the membrane, and wherein an outer surface of the membrane is substantially flush with, or protruding from, said side of the device.

30 3. A device according to any one of the preceding claims, wherein the volume of the chamber (4, 4a, 4b) is 1 ml or less, preferably 1 µl or less, more preferably 100 nl or less.

    4. A device according to any one of the preceding claims, wherein the outlet
35   capillary channel is spatially dimensioned so that the gas kinetics of the

3

species and the carrier gas, after leaving the outlet capillary channel, can be described as a ballistic flow (Knudsen number significantly above 1), or as a near ballistic flow.

5.   5. A device according to any one of the preceding claims, wherein the inlet capillary channel is spatially dimensioned so that limited, preferably no, back-diffusion occurs from the chamber (4, 4a, 4b).

   6. A device according to any one of the preceding claims, wherein the
10.   membrane is perforated.

   7. A device according to any one of the preceding claims, wherein the device comprises at least
      a. a first structural element (41a, 41c), and
15.   b. a second structural element (41b) and
      wherein the membrane (5) is formed in the first structural element and on a first side (32a, 32b) of the first structural element, and wherein the second structural element (41b) is joined to the first structural element on the opposite side of the first structural element with respect to the first
20.   side.

   8. A device according to claim 7, wherein one, or more, cavities are formed in the first structural element, wherein one, or more, cavities (3, 4, 4a, 4b, 6) correspond to one or more of
25.   a. the chamber (4, 4a, 4b),
      b. the inlet capillary (3),
      c. the outlet capillary (6),
      and wherein the second structural element (41b) forms a barrier in least one of the one, or more, cavities.
30.
   9. A device according to claims 7 or 8 wherein one, or more, of
      a. the chamber (4),
      b. the inlet capillary (3),
      c. the outlet capillary (6),
35.   are placed between

4

- the first side of the first structural element (32a, 32b), and
- the second structural element (41b).

10. A system (100) for analysis comprising

5
- a device (10) according to any of the previous claims, and
- an analysis instrument, such as a mass spectrometer (MS),

where the outlet capillary channel (6) of the device is connected with an inlet of the analysis instrument.

10   11. A system (100) for analysis comprising

- a device (10) according to any of claims 1-9, and
- a source of a carrier gas, which is connected to the chamber via the inlet capillary channel (3).

15   12. A system (100) according to claims 10 or 11, wherein a characteristic time, corresponding to a time difference between

a. a change in the associated liquid sample (20),

and

b. a point in time wherein a corresponding signal change as measured

20   by the analysis instrument reaches 1/e with respect to a saturation level of said signal,

is 1 min. or less, preferably 10 s or less, more preferably 1 s or less.

13. A method for extracting a volatile species from a liquid sample (20), the

25   method comprising:

a. providing a device (10) according to any one of claims 1-9, or a system (100) according to any of claims 10-12,

b. exposing the membrane (5) to the liquid sample (20), and

c. allowing the volatile species to pass through the membrane.

30

14. A method for extracting a volatile species from a liquid sample according to claim 13, wherein the method comprises

- at least partially immersing the device according to any one of claims 1-9,

5

so as to realize exposing the membrane to the liquid sample, preferably the liquid sample being an aqueous liquid, such as wherein a main component of the liquid sample is water.

5   15. Use of a device according to any of claims 1-9, or a system according to any of claims 10-12, for extracting a volatile species from a liquid sample (20).

Bibliography

[1] Steven Chu and Arun Majumdar. Opportunities and challenges for a sustainable energy future. *Nature*, 488(7411):294–303, 2012.

[2] United Nations. The World at Six Billion. Technical report, 1999.

[3] United Nations. World Population Prospects. Technical report, 2017.

[4] Ronald Lee. The Outlook for Population Growth. *Science*, 333(6042):569–573, 2011.

[5] British Petroleum (BP). Statistical Review of World Energy. (June), 2017.

[6] Hans Rosling. Gapminder, 2011.

[7] United Nations. Human Development for Everyone. Technical report, 2016.

[8] International Energy Agency (IEA). World Energy Outlook. Technical report, 2016.

[9] Lawrence Livermore National Laboratory (LLNL). Energy Flow Chart, 2016.

[10] Paul J. Crutzen. Geology of mankind. *Nature*, 415(January):23, 2002.

[11] P. J. Gleckler, B. D. Santer, C. M. Domingues, D. W. Pierce, T. P. Barnett, J. a. Church, K. E. Taylor, K. M. AchutaRao, T. P. Boyer, M. Ishii, and P. M. Caldwell. Human-induced global ocean warming on multidecadal timescales. *Nat. Clim. Chang.*, 2(7):524–529, 2012.

[12] Intergovernmental Panel on Climate Change (IPCC). Climate Change 2014 Synthesis Report. Technical report, 2014.

[13] United Nations. Paris Agreement, 2016.

[14] Randall Munroe. xkcd − 4.5 degrees, 2014.

[15] David J. Murphy and Charles A S Hall. Year in review − EROI or energy return on (energy) invested. *Ann. N. Y. Acad. Sci.*, 1185:102–118, 2010.

[16] Johan Rockström, Will Steffen, Kevin Noone, Åsa Persson, F. Stuart Chapin, Eric Lambin, Timothy M. Lenton, Marten Scheffer, Carl Folke, Hans Joachim Schellnhuber, Björn Nykvist, Cynthia A. de Wit, Terry Hughes, Sander van der Leeuw, Henning Rodhe, Sverker Sörlin, Peter K. Snyder, Robert Costanza, Uno Svedin, Malin Falkenmark, Louise Karl- berg, Robert W. Corell, Victoria J. Fabry, James Hansen, Brian Walker, Diana Liverman, Katherine Richardson, Paul Crutzen, and Jonathan Fo- ley. Planetary boundaries: Exploring the safe operating space for human- ity. *Nature*, 14(2), 2009.

[17] Steven Chu, Yi Cui, and Nian Liu. The path towards sustainable energy. *Nat. Mater.*, 16(1):16–22, 2017.

[18] Barack Obama. The irreversible momentum of clean energy. *Science*, 355(6321):126–129, 2017.

[19] Siemens. Next47: Decentralized Electrification, 2016.

[20] Ib Chorkendorff and J.W. Niemantsverdriet. *Concepts of Modern Cataly- sis and Kinetics.* 2003.

[21] Paul Sabatier. Hydrogenations et deshydrogenations par catalyse. *Berichte der Dtsch. Chem. Gesellschaft*, 44(3):1984–2001, 1911.

[22] Peter Atkins and Julio de Paola. *Physical Chemisry.* Oxford University Press, ninth edition, 2014.

[23] M. J. Weaver, S .-C. Chang, L. W. H. Leung, X. Jiang, M. Rubel, M. Szk- larczyk, D. Zurawski, and A. Wieckowski. Evaluation of absolute satu- ration coverages of carbon monoxide on ordered low-index platinum and rhodium electrodes. *J. Electroanal. Chem.*, 327(1-2):247–260, jun 1992.

[24] InProcess Instruments. Operating Principle of a Quadrupole Mass Spec- trometer, 2009.

[25] Pfeiffer Vacuum. *Vacuum Technology Know-how Book.* 2013.

[26] George Hoch and Bessel Kok. A mass spectrometer inlet system for sampling gases dissolved in liquid phases. *Arch. Biochem. Biophys.*, 101(1):160–170, apr 1963.

[27] S. Bruckenstein and R.R. Gadde. Use of a Porous Electrode for in Situ Mass Spectrometric Determination of Volatile Electrode Reaction Products. *J. Am. Chem. Soc.*, 93(3):793–794, 1971.

[28] Robert B. Bird, Warren E. Stewart, and Edwin N. Lightfoot. *Transport Phenomena*. John Wiley and Sons, second edition, 2007.

[29] Helmut Baltruschat. Differential electrochemical mass spectrometry. *J. Am. Soc. Mass Spectrom.*, 15(12):1693–1706, dec 2004.

[30] O. Wolter and J. Heitbaum. Differential Electrochemical Mass Spectroscopy (DEMS) - a New Method for the Study of Electrode Processes. *Berichte der Bunsengesellschaft für Phys. Chemie*, 88:2–6, 1984.

[31] Helmut Baltruschat and U. Schmiemann. The Adsorption of Unsaturated Organic Species at Single Crystal Electrodes Studied by Differential Electrochemical Mass Spectrometry. *J. Phys. Chem.*, 97(3):452–460, 1993.

[32] Zenonas Jusys, H. Massong, and Helmut Baltruschat. A New Approach for Simultaneous DEMS and EQCM: Electro-oxidation of Adsorbed CO on Pt and Pt-Ru. *J. Electrochem. Soc.*, 146(3):1093–1097, 1999.

[33] Yunzhi Gao, Hideto Tsuji, Hideshi Hattori, and Hideaki Kita. New on-line mass spectrometer system designed for platinum-single crystal electrode and electroreduction of acetylene. *J. Electroanal. Chem.*, 372(1-2):195–200, jul 1994.

[34] Ad H. Wonders, Tom H. M. Housmans, V. Rosca, and Marc T. M. Koper. On-line mass spectrometry system for measurements at single-crystal electrodes in hanging meniscus configuration. *J. Appl. Electrochem.*, 36(11):1215–1221, sep 2006.

[35] Abd-El-Aziz A. Abd-El-Latif, Jie Xu, Nicky Bogolowski, Peter Königshoven, and Helmut Baltruschat. New Cell for DEMS Applicable to Different Electrode Sizes. *Electrocatalysis*, 3(1):39–47, mar 2012.

[36] D. Tegtmeyer, A. Heindrichs, and J. Heitbaum. Electrochemical on Line Mass Spectrometry on a Rotating Electrode Inlet System. *Ber. Bunsenges. Phys. Chem*, 93:201–206, 1989.

[37] K. Jambunathan and A. C. Hillier. Measuring Electrocatalytic Activity on a Local Scale with Scanning Differential Electrochemical Mass Spectrometry. *J. Electrochem. Soc.*, 150(6):E312, 2003.

[38] Jan-Philipp Grote, Aleksandar R. Zeradjanin, Serhiy Cherevko, and Karl J. J. Mayrhofer. Coupling of a scanning flow cell with online electrochemical mass spectrometry for screening of reaction selectivity. *Rev. Sci. Instrum.*, 85(10):104101, oct 2014.

[39] Zenonas Jusys, J. Kaiser, and R. Jürgen Behm. A novel dual thin-layer flow cell double-disk electrode design for kinetic studies on supported catalysts under controlled mass-transport conditions. *Electrochim. Acta*, 49(8):1297–1305, 2004.

[40] M. Heinen, Y. X. Chen, Zenonas Jusys, and R. Jürgen Behm. In situ ATR-FTIRS coupled with on-line DEMS under controlled mass transport conditions-A novel tool for electrocatalytic reaction studies. *Electrochim. Acta*, 52(18):5634–5643, 2007.

[41] Christoph J. Bondue, Peter Königshoven, and Helmut Baltruschat. A New 2-Compartment Flow Through Cell for the Simultaneous Detection of Electrochemical Reaction Products by a Detection Electrode and Mass Spectroscopy. *Electrochim. Acta*, 214:241–252, oct 2016.

[42] N. Tsiouvaras, S. Meini, I. Buchberger, and H. A. Gasteiger. A Novel On-Line Mass Spectrometer Design for the Study of Multiple Charging Cycles of a Li-O2 Battery. *J. Electrochem. Soc.*, 160(3):A471–A477, jan 2013.

[43] Ehab Mostafa, Abd-El-Aziz A. Abd-El-Latif, Richard Ilsley, Gary Attard, and Helmut Baltruschat. Quantitative DEMS study of ethanol oxidation: effect of surface structure and Sn surface modification. *Phys. Chem. Chem. Phys.*, 14(46):16115–16129, 2012.

[44] Zenonas Jusys, J. Kaiser, and R. Jürgen Behm. Composition and activity of high surface area PtRu catalysts towards adsorbed CO and methanol electrooxidation – A DEMS study. *Electrochim. Acta*, 47(22-23):3693–3706, aug 2002.

[45] Klaas Jan P. Schouten, Elena Pérez Gallent, and Marc T. M. Koper. The influence of pH on the reduction of CO and and CO2 to hydrocarbons on copper electrodes. *J. Electroanal. Chem.*, 716:53–57, 2014.

[46] Bryan D. McCloskey, Rouven Scheffler, Angela Speidel, Girish Girishkumar, and Alan C. Luntz. On the mechanism of nonaqueous Li-O2 electrochemistry on C and its kinetic overpotentials: Some implications for Li-air batteries. *J. Phys. Chem. C*, 116(45):23897–23905, 2012.

[47] Raimo a. Ketola and Frants R. Lauritsen. Membrane Inlet Mass Spectrometry (MIMS) in Historical Perspective. In *Encycl. Mass Spectrom.*, pages 143–148. Elsevier, 2016.

[48] Elmar Heinzle and Matthias Reuss. *Mass Spectrometry in Biotechnological Process Analysis and Control.* Springer US, Boston, MA, 1987.

[49] Tapio Kotiaho, Frants R. Lauritsen, Tarun K. Choudhury, R. Graham Cooks, and George T. Tsao. Membrane Introduction Mass Spectrometry. *Anal. Chem.*, 63(18):875–883, 1991.

[50] R. Graham Cooks and Tapio Kotiaho. Membrane Introduction Mass Spectrometry in Environmental Analysis. In *Pollut. Prev. Ind. Process.*, pages 126–154. oct 1992.

[51] Scott Bauer. Membrane introduction mass spectrometry; an old method that is gaining new interest through recent technological advances. *TrAC Trends Anal. Chem.*, 14(5):202–213, may 1995.

[52] K. F. Hansen and H. Degn. On-line membrane inlet mass spectrometry for feed-back control of precursor concentration in penicillin fermentation. *Biotechnol. Tech.*, 10(7):485–490, jul 1996.

[53] Tapio Kotiaho. On-site Environmental and In Situ Process Analysis by Mass Spectrometry. *J. Mass Spectrom.*, 31(1):1–15, jan 1996.

[54] Frants R. Lauritsen and Tapio Kotiaho. Advances in Membrane Inlet Mass Spectrometry (MIMS). *Rev. Anal. Chem.*, 15(4):237–264, jan 1996.

[55] N. Srinivasan, R. C. Johnson, N. Kasthurikrishnan, P. Wong, and R. Graham Cooks. Membrane introduction mass spectrometry. *Anal. Chim. Acta*, 350(3):257–271, sep 1997.

[56] G. Cowie and D. Lloyd. Membrane inlet ion trap mass spectrometry for the direct measurement of dissolved gases in ecological samples. *J. Microbiol. Methods*, 35(1):1–12, feb 1999.

[57] R. C. Johnson, R. Graham Cooks, T. M. Allen, M. E. Cisper, and P. H. Hemberger. Membrane introduction Mass Spectrometry: Trends and applications. *Mass Spectrom. Rev.*, 19(1):1–37, 2000.

[58] A.A. Abd-El-Latif, C.J. Bondue, S. Ernst, M. Hegemann, J.K. Kaul, M. Khodayari, E. Mostafa, A. Stefanova, and H. Baltruschat. Insights into electrochemical reactions by differential electrochemical mass spectrometry. *Trends Anal. Chem.*, 70:4–13, 2015.

[59] Herbert Oberacher, Florian Pitterl, Robert Erb, and Sabine Plattner. Mass spectrometric methods for monitoring redox processes in electrochemical cells. *Mass Spectrom. Rev.*, 34(1):64–92, jan 2015.

[60] R. Sander. Compilation of Henry's law constants (version 4.0) for water as solvent. *Atmos. Chem. Phys.*, 15(8):4399–4981, apr 2015.

[61] Kenneth Nielsen, Thomas Andersen, Robert Jensen, Jane H. Nielsen, and Ib Chorkendorff. An open-source data storage and visualization back end for experimental data. *J. Lab. Autom.*, 19(2):183–90, 2014.

[62] Pine Research Instrumentation. ChangeDisk RDE PTFE U-Cup assembly, 2017.

[63] Marc T. M. Koper, Stanley C. S. Lai, and Enrique Herrero. Mechanisms of the Oxidation of Carbon Monoxide and Small Organic Molecules at Metal Electrodes. In *Fuel Cell Catal. A Surf. Sci. Approach*, pages 159–207. 2009.

[64] Tobias Reier, Mehtap Oezaslan, and Peter Strasser. Electrocatalytic oxygen evolution reaction (OER) on Ru, Ir, and pt catalysts: A comparative study of nanoparticles and bulk materials. *ACS Catal.*, 2(8):1765–1772, 2012.

[65] Zenonas Jusys, J. Kaiser, and R. Jürgen Behm. Electrooxidation of CO and H2/CO mixtures on a carbon-supported Pt catalyst − a kinetic and mechanistic study by differential electrochemical mass spectrometry. *Phys. Chem. Chem. Phys.*, 3(21):4650–4660, oct 2001.

[66] Hongsen Wang, Zenonas Jusys, R. Jürgen Behm, and Héctor D. Abruña. New Insights into the Mechanism and Kinetics of Adsorbed CO Electrooxidation on Platinum: Online Mass Spectrometry and Kinetic Monte Carlo Simulation Studies. *J. Phys. Chem. C*, 116(20):11040–11053, may 2012.

[67] Maria J. T. C. Van Der Niet, Nuria Garcia-Araez, Javier Hernández, Juan M. Feliu, and Marc T .M. Koper. Water dissociation on well-defined platinum surfaces: The electrochemical perspective. *Catal. Today*, 202(1):105–113, 2013.

[68] National Institute of Standards and Technology. *NIST Chemistry WebBook*. 69 edition, 2017.

[69] Peter C. K. Vesborg, Su-il In, Jakob L. Olsen, Toke R. Henriksen, Billie L. Abrams, Yidong Hou, Alan Kleiman-Shwarsctein, Ole Hansen, and Ib Chorkendorff. Quantitative Measurements of Photocatalytic CO-Oxidation as a Function of Light Intensity and Wavelength over TiO 2 Nanotube Thin Films in μ-Reactors. *J. Phys. Chem. C*, 114(25):11162–11168, jul 2010.

[70] Hiden Analytical Ltd. Relative Sensitivity, 2017.

[71] J. H. Leck. *Total and Partial Pressure Measurement in Vacuum Systems*. Blackie, 1989.

[72] M Soni, S Bauer, J W Amy, P Wong, and R G Cooks. Direct Determination of Organic Compounds in Water At Parts-Per-Quadrillion Levels By Membrane Introduction Mass Spectrometry. *Anal. Chem.*, 67(8):1409–1412, 1995.

[73] Søren Bertelsen Scott. *Investigating the Electrochemical Reduction of Carbon Dioxide using In Situ Mass Spectrometry.* Master's thesis, 2016.

[74] A. Roth. Gas flow at low pressures. In *Vac. Technol.*, volume 62, pages 62–148. 1990.

[75] Toke Riishøj Henriksen. *Silicon Microreactors for Measurements of Catalytic Activity.* PhD thesis, 2010.

[76] Jakob Lind Olsen. *Heterogeneous catalysis in highly sensitive microreactors.* PhD thesis, 2010.

[77] Toke R. Henriksen, Jakob L. Olsen, Peter C. K. Vesborg, Ib Chorkendorff, and Ole Hansen. Highly sensitive silicon microreactor for catalyst testing. *Rev. Sci. Instrum.*, 80(12):4101, dec 2009.

[78] Henrik Bruus. *Theoretical Microfluidics.* Oxford University Press, 2008.

[79] Daniel B. Trimarco. *Development of a liquid phase detector for electrochemical products.* Master's thesis, 2013.

[80] Felix Sharipov. Gaseous mixtures in vacuum systems and microfluidics. *J. Vac. Sci. Technol. A Vacuum, Surfaces, Film.*, 31(5):050806, 2013.

[81] R. Gordon Livesey. Flow of Gases Through Tubes and Orifices. In *Found. Vac. Sci. Technol.*, pages 81–105. 1998.

[82] John F. O'Hanlon. *A User's Guide to Vacuum Technology.* 2003.

[83] Ulrich J. Quaade, Søren Jensen, and Ole Hansen. Fabrication and modeling of narrow capillaries for vacuum system gas inlets. *J. Appl. Phys.*, 97(4):1–5, 2005.

[84] Yoshio Hori, Katsuhei Kikuchi, and Shin Suzuki. Production of CO and CH4 in electrochemical reduction of CO2 at metal electrodes in aqueous hydrogencarbonate solution. *Chem. Lett.*, 14(11):1695–1698, nov 1985.

[85] Kendra P. Kuhl, Etosha R. Cave, David N. Abram, and Thomas F. Jaramillo. New insights into the electrochemical reduction of carbon dioxide on metallic copper surfaces. *Energy Environ. Sci.*, 5(5):7050–7059, 2012.

[86] Yihong Chen, Christina W. Li, and Matthew W. Kanan. Aqueous CO2 reduction at very low overpotential on oxide-derived Au nanoparticles. *J. Am. Chem. Soc.*, 134(49):19969–72, dec 2012.

[87] Yoshio Hori, Akira Murata, and Ryutaro Takahashi. Formation of hydrocarbons in the electrochemical reduction of carbon dioxide at a copper electrode in aqueous solution. *J. Chem. Soc. Faraday Trans. 1 Phys. Chem. Condens. Phases*, 85(8):2309, 1989.

[88] Christina W. Li, Jim Ciston, and Matthew W. Kanan. Electroreduction of carbon monoxide to liquid fuel on oxide-derived nanocrystalline copper. *Nature*, 508(7497):504–507, apr 2014.

[89] Xiaofeng Feng, Kaili Jiang, Shoushan Fan, and Matthew W. Kanan. Grain-Boundary-Dependent CO2 Electroreduction Activity. *J. Am. Chem. Soc.*, page 150406073249009, 2015.

[90] Arnau Verdaguer-Casadevall, Christina W. Li, Tobias P. Johansson, Soren B. Scott, Joseph T. McKeown, Mukul Kumar, Ifan E.L. Stephens, Matthew W. Kanan, and Ib Chorkendorff. Probing the Active Surface Sites for CO Reduction on Oxide-Derived Copper Electrocatalysts. *J. Am. Chem. Soc.*, 137(31):9808–9811, 2015.

[91] Ana Sofia Varela, Matthias Kroschel, Tobias Reier, and Peter Strasser. Controlling the selectivity of CO2 electroreduction on copper: The effect of the electrolyte concentration and the importance of the local pH. *Catal. Today*, 260:8–13, 2016.

[92] Erlend Bertheussen, Arnau Verdaguer-Casadevall, Davide Ravasio, Joseph H. Montoya, Daniel B. Trimarco, Claudie Roy, Sebastian Meier, Jorgen Wendland, Jens K. Norskov, Ifan E. L. Stephens, and Ib Chorkendorff. Acetaldehyde as an Intermediate in the Electroreduction of Carbon Monoxide to Ethanol on Oxide-Derived Copper. *Angew. Chemie Int. Ed.*, 55(4):1450–1454, jan 2016.

[93] Hemma Mistry, Ana Sofia Varela, Cecile S. Bonifacio, Ioannis Zegkinoglou, Ilya Sinev, Yong-Wook Choi, Kim Kisslinger, Eric A. Stach, Judith C. Yang, Peter Strasser, and Beatriz Roldan Cuenya. Highly selective plasma-activated copper catalysts for carbon dioxide reduction to ethylene. *Nat. Commun.*, 7, 2016.

[94] Dahee Kim, Seunghwa Lee, Joey D. Ocon, Beomgyun Jeong, Jae Kwang Lee, and Jaeyoung Lee. Insights into an autonomously formed oxygen-evacuated Cu2O electrode for the selective production of C2H4 from CO2. *Phys. Chem. Chem. Phys.*, 17(2):824–830, 2015.

[95] André Eilert, Filippo Cavalca, F. Sloan Roberts, Jürg Osterwalder, Chang Liu, Marco Favaro, Ethan J. Crumlin, Hirohito Ogasawara, Daniel Friebel, Lars G.M. Pettersson, and Anders Nilsson. Subsurface Oxygen in Oxide-Derived Copper Electrocatalysts for Carbon Dioxide Reduction. *J. Phys. Chem. Lett.*, 8(1):285–290, 2017.

[96] Yanwei Lum, Youngkook Kwon, Peter Lobaccaro, Le Chen, Ezra Lee Clark, Alexis T. Bell, and Joel W. Ager. Trace Levels of Copper in Carbon Materials Show Significant Electrochemical CO2 Reduction Activity. *ACS Catal.*, 6(1):202–209, 2016.

[97] Klaas Jan P. Schouten, Zisheng Qin, Elena Pérez Gallent, and Marc T .M. Koper. Two pathways for the formation of ethylene in CO reduction on single-crystal copper electrodes. *J. Am. Chem. Soc.*, 134(24):9864–9867, 2012.

[98] F. Sloan Roberts, Kendra P. Kuhl, and Anders Nilsson. High selectivity for ethylene from carbon dioxide reduction over copper nanocube electrocatalysts. *Angew. Chemie Int. Ed.*, 54(17):5179–5182, 2015.

[99] Cécile S. Le Duff, Matthew J. Lawrence, and Paramaconi Rodriguez. Role of the adsorbed oxygen species in the selective electrochemical reduction of CO2 to alcohols and carbonyls on copper electrodes. *Angew. Chemie Int. Ed.*, aug 2017.

[100] Chuan Shi, Heine A. Hansen, Adam C. Lausche, and Jens K. Nørskov. Trends in electrochemical CO2 reduction activity for open and close-packed metal surfaces. *Phys. Chem. Chem. Phys.*, 16(10):4720, 2014.

[101] Andrew A. Peterson and Jens K. Nørskov. Activity descriptors for CO2 electroreduction to methane on transition-metal catalysts. *J. Phys. Chem. Lett.*, 3(2):251–258, 2012.

[102] H. A. Hansen, C. Shi, A. C. Lausche, A. A. Peterson, and J. K. Nørskov. Bifunctional alloys for the electroreduction of CO2 and CO. *Phys. Chem. Chem. Phys.*, 18(13):9194–9201, 2016.

[103] Aleksandra Vojvodic and Jens K. Nørskov. New design paradigm for heterogeneous catalysts. *Natl. Sci. Rev.*, 2(2):140–143, 2015.

[104] Aayush R. Singh, Brian A. Rohr, Jay A. Schwalbe, Matteo Cargnello, Karen Chan, Thomas F. Jaramillo, Ib Chorkendorff, and Jens K. Nørskov. Electrochemical Ammonia Synthesis - The Selectivity Challenge. *ACS Catal.*, 7(1):706–709, 2017.

[105] Ruud Kortlever, Jing Shen, Klaas Jan P. Schouten, Federico Calle-Vallejo, and Marc T. M. Koper. Catalysts and Reaction Pathways for the Electrochemical Reduction of Carbon Dioxide. *J. Phys. Chem. Lett.*, 6(20):4073–4082, 2015.

[106] Joseph H. Montoya, Chuan Shi, Karen Chan, and Jens K. Nørskov. Theoretical Insights into a CO Dimerization Mechanism in CO 2 Electroreduction. *J. Phys. Chem. Lett.*, 6(11):2032–2037, 2015.

[107] Yoshio Hori, Ryutaro Takahashi, Yuzuru Yoshinami, and Akira Murata. Electrochemical Reduction of CO at a Copper Electrode. *J. Phys. Chem. B*, 101(36):7075–7081, 1997.

[108] Elie Protopopoff and Philippe Marcus. Potential-pH diagrams for hydroxyl and hydrogen adsorbed on a copper surface. *Electrochim. Acta*, 51(3):408–417, 2005.

[109] C. S. Alexander and J. Pritchard. Chemisorption of hydrogen on evaporated copper films. *J. Chem. Soc. Faraday Trans. 1*, 68:202, 1972.

End of thesis